Development of Optoelectronic Devices and Computational Tools for the Production and Manipulation of Heavy Rydberg Systems

by

Jeffrey Philippson

A thesis submitted to the Department of Physics,

Engineering Physics and Astronomy

in conformity with the requirements for

the degree of Master of Science

Queen's University

Kingston, Ontario, Canada

September, 2007

Abstract

Experimental and theoretical progress has been made toward the production and manipulation of novel atomic and molecular states. The design, construction and characterization of a driver for an acousto–optic modulator is presented, which achieves a maximum diffraction efficiency of 54 % at 200 MHz, using a commercial modulator. A novel design is presented for a highly sensitive optical spectrum analyzer for displaying laser mode structure in real time. Utilizing programmable microcontrollers to read data from a CMOS image sensor illuminated by the diffraction pattern from a Fabry–Pérot interferometer, this device can operate with beam powers as low as 3.3 μW, at a fraction of the cost of equivalent products. Computational results are presented analyzing the behaviour of a model quantum system in the vicinity of an avoided crossing. The results are compared with calculations based on the Landau–Zener formula, with discussion of its limitations. Further computational work is focused on simulating expected conditions in the implementation of a technique for coherent control quantum states atomic and molecular beams. The work presented provides tools to further the aim of producing large, mono–energetic populations of heavy Rydberg systems.

Acknowledgements

I would like to thank the people whose help and support has facilitated the completion of this thesis...

First and foremost, I would like to convey my sincere gratitude for the help, advice, patience and understanding shown by my supervisor Ralph Shiell. His knowledge and enthusiasm are a source of constant inspiration to me.

Matt Ugray and Tefo James Toai were collaborators on the optical spectrum analyzer project presented in chapter 4, they both made significant contributions and were both a pleasure to work with. Figure 4.2 was created by MU. In addition, I would like to thank Ken Sutherland for early work on optimising a Fabry–Pérot interference pattern and Jonathan Murrell for useful discussions concerning CMOS image sensors.

I wish to thank Edward Wilson for his assistance with the use of various machine tools and Ralph Fredrick for useful discussions concerning the design of electronic devices.

James Fraser is my Queen's University co–supervisor; I wish to express my thanks for his support during my time at Queen's.

Finally I want to extend my gratitude to the entire physics department at Trent University for making me feel welcome, for stimulating discussions and for generally being a wonderful group of people.

Dedicated to Mary and Peter,

truly special people who are a source of constant inspiration.

Contents

List of Tables

List of Figures

List of Acronyms

ADC – Analog to digital converter

AOM – Acousto–optic modulator

APT – Adiabatic population transfer

BEC – Bose–Einstein condensate

CCD – Charge–coupled device

CMOS – Complimentary metal–oxide semiconductor

CPT – Coherent population trapping

ECDL – External cavity diode laser

EEPROM – Electronically erasable programmable read–only memory

I^2C – Inter–integrated circuit

MOSFET – Metal–oxide semiconductor field effect transistor

MOT – Magneto–optical trap

OSA – Optical spectrum analyzer

PCB – Printed Circuit board

PLCC – Plastic leadless chip carrier

RF – Radio frequency

SRAM – Static random access memory

STIRAP – Stimulated Raman adiabatic passage

TIPPS – Threshold ion–pair production spectroscopy

VCO – Voltage–controlled oscillator

VSCPT – Velocity–selective coherent population trapping

VSWR – Voltage standing wave ratio

VUV – Vacuum ultra–violet

ZIF – Zero insertion force

Chapter 1

Introduction

The arrival of quantum theory at the beginning of the 20^{th} century seemed to split the natural world in two; the macroscopic world governed by the familiar laws of classical physics laid down by Kepler, Galileo, Newton and others, and the microscopic world where the fundamentally different rules of quantum mechanics apply.

While the correspondence principle has allowed a sense of consistency to be maintained, the boundary between the classical and quantum domains remains mysterious. Towards the end of the 20^{th} century, significant progress was made in producing coherent quantum objects with sizes approaching the macroscopic scale. Bose–Einstein condensates (BECs) are at the vanguard of this quest for ever larger quantum systems;[1] less well known are a class of molecules in weakly bound ion–pair states, known as heavy Rydberg systems.[2] Together with *electronic* Rydberg states in which an electron is weakly bound,[3] these novel systems occupy the fertile territory straddling the quantum and classical worlds, with typical bond lengths on the order of 1 μm.

Distinguished by their large size and simple internal structure, Rydberg states present unique opportunities for experimental investigations aimed at bridging the quantum–classical divide. Electronic Rydberg states are states of high principal quantum number n. Stable Rydberg states with high angular momentum maintain a large separation between an excited valence electron and the ion core; consequently, the potential seen by the electron resembles, to a first approximation, the $^1/_r$ coulomb potential within a hydrogen atom. Heavy Rydberg systems have a similar structure with the valence electron replaced by a negative ion, giving a reduced mass orders of magnitude larger than any electronic Rydberg state and a correspondingly long time–scale for evolution of the wavefunction.

1.1 Research goals

Our intention is to develop efficient techniques for producing large populations of heavy Rydberg systems with low internal energies. To date these systems have been produced in small numbers, using inefficient frequency mixing techniques to obtain vacuum–ultra–violet laser light to excite different molecular species into ion–pair states.[4] Two approaches will be investigated in the Optical Physics Laboratory at Trent University. The first is excitation at short range from a molecular beam (*the beam experiment*), prepared in an initial state using the population transfer mechanism described in chapter 7, before exciting to heavy Rydberg states using a UV laser source. An alternative approach (*the MOT experiment*) is based on long range excitation due to collisions between cold, excited atoms in a magneto–optical trap (MOT). Such collisions can lead to charge transfer, forming bound ion–pairs provided they are prepared in an appropriate initial state.

The ability to produce heavy Rydberg systems with internal energies accessible to lower optical frequency UV lasers will enable their production in far greater numbers than has hitherto been possible. To this end, we will be investigating the relationship between the production of heavy Rydberg systems in a molecular beam and the initial vibrational state of the molecules. To date, only a small number of molecular species have been used to create these exotic molecules, although any atom with a positive electronegativity can, in theory, bind to a positive ion and form a heavy Rydberg system. The intention is to use Li_2 as it has an ion–pair threshold energy accessible using near UV light and an atomic mass that results in a relatively simple internal structure. To the author's knowledge, lithium has not yet been used for the creation of a heavy Rydberg system.

Once formed, the heavy Rydberg systems can be stabilized to avoid dissociation into free ions; this is achieved through control of the angular momentum, which, in–turn, affects the bond–length. Detection of heavy Rydberg systems is generally accomplished through field-dissociation, which allow determination of the binding energy of the system.

Electronic Rydberg states with just a single excited electron have a reduced mass approximately equal to the electron mass, irrespective of the species, while different species of heavy Rydberg system have a wide range of reduced mass. As the rate of time evolution of the wavefunction is inversely proportional to the square–root of the reduced mass, this provides opportunities for the experimental determination of theoretically predicted transition rates and investigation of the breakdown of theoretical concepts such as the Franck–Condon principle and the Born–Oppenheimer approximation.

1.2 Structure of the thesis

Chapter 2 presents a review of relevant literature covering electronic and heavy Rydberg states and useful material related to the construction of electronic and optoelectronic equipment similar to that presented in this thesis.

The following three chapters outline the design, construction and characterization of equipment that will be required in the near future for planned experiments discussed above. These include a driver for an acousto–optic modulator, a system for displaying laser mode structure in real time, and power supplies for research equipment.

The final two chapters present the results of computational work simulating model systems under conditions relevant to the production of electronic and heavy Rydberg states. Chapter 6 presents an analysis of adiabatic versus diabatic passage in curve crossings, based on precise numerical solutions to the equations of motion for the state amplitudes in a model system with reference to calculations using the well–known Landau–Zener formula. These results are directly related to the problem of the formation of ion–pair states from covalently bound diatomic molecules. Chapter 7 examines the process of adiabatic population transfer (APT) and its theoretical foundation in the concept of coherent population trapping. A number of different approaches for experimental implementation of APT are considered with particular focus on the effects of various anticipated experimental deviations from the theoretical ideal.

Chapter 2

Literature Review

The work presented in this thesis provides tools for the coherent control of atomic and molecular Rydberg states and heavy Rydberg systems. The following sections provide an overview of the available literature, covering theoretical and experimental considerations in the study of Rydberg states, and the construction of equipment necessary for their efficient production and manipulation.

2.1 Rydberg atoms

Rydberg atoms are atoms with a high principle quantum number n. One of the defining features of such atoms is the nearly hydrogenic $^1/_r$ potential that results from the large separation between the excited electron and the remaining ion–core. States with more than one highly excited electron, and states with low angular momentum in which the electron may pass close to, or even penetrate, the ion–core, show a significant deviation from this hydrogenic potential. These exceptions will be excluded from the definition of a Rydberg atom in this thesis.

Rydberg atoms have been the focus of intense scientific study for more than a century,[5] with early experiments using absorption spectroscopy to determine their energy level structure,[6] a technique that remains invaluable to the present day.

Prior to the introduction of tunable dye lasers, the production of electronic Rydberg states in large numbers relied on techniques such as electron impact excitation:[7]

$$e^- + A \to A^* + e^-, \tag{2.1}$$

and charge exchange excitation:[8]

$$A^+ + B \to A^* + B^+, \tag{2.2}$$

however these both produce populations with a broad spread of energies. The introduction of the tunable dye laser in the 1970s led to renewed interest in the field due to the exquisite control over the final state of the population afforded by narrow–band optical excitation.[9] Farley *et al.* demonstrated the efficacy of dye lasers in an early experiment investigating the hyperfine structure of the $n \approx 10$ states in rubidium and caesium.[10]

The literature on Rydberg atoms is extensive; a recent and comprehensive treatise covering both theoretical and experimental considerations is provided by Gallagher,[3] who makes regular use of the earlier work by Koch.[11] In addition to these general overviews, there exist numerous works on the specifics of excitation, cooling, trapping and detection of conventional Rydberg states of atoms and molecules.

Two schemes for the coherent excitation of atomic populations to stable Rydberg states were presented by Deiglmayr *et al.*;[12] excitation probabilities approaching unity were achieved in ^{87}Rb using the population transfer mechanism investigated theoretically in chapter 7 of this thesis. An alternative approach utilizing a two–photon resonance in a 3–level system, in which the excitation was far–detuned from the intermediate state, provided a similarly high excitation probability with more stringent pulse timing and laser power requirements.

Cooling of electronic Rydberg states can stabilize populations against autoionization and facilitate trap loading; there are a number of different approaches. A cloud of cold atoms can be obtained through laser cooling and subsequently excited to Rydberg states. An excellent review of theoretical and experimental considerations in laser cooling is given by Metcalf and Straten.[13] Guo *et al.* utilize velocity–selective coherent population trapping (VSCPT) to obtain cold Rydberg states of caesium and sodium.[14] This technique involves preparing an atomic population in a coherent superposition of internal and external momentum states, such that low velocity atoms become decoupled from the light field.

Cooling molecules can present a greater challenge due to the high density of states, which disrupt the closed multilevel systems addressed in laser cooling. A technique utilizing a time–varying electric field to decelerate neutral dipolar molecules was developed by Bethlem *et al.*,[15] and was extended by Softley *et al.* for use with Rydberg states of molecular hydrogen.[16]

Atomic and molecular beam methods find wide application in the study of Rydberg states; Wright *et al.* used an atomic beam source to perform optical spectroscopy on Rydberg states of argon,[17] taking advantage of the narrow transverse velocity distribution that results from beam collimation, and Doppler tuning the laser frequency by varying the intersection angle of the laser and the atomic beam.

An in–depth investigation of the formation and containment of ^{85}Rb Rydberg atoms in a magnetic trap was provided by Choi *et al.*,[18] with observed trapping times exceeding 200 ms. Here, the rubidium atoms were laser cooled then optically excited to Rydberg states, from which a small fraction were collisionally excited to long–lived, high angular momentum states, which were collected in a magnetic trap. In addition, theoretical calculations are presented illustrating the operating principles of the trap, including a demonstration that the majority the target atoms are low field seeking, justifying the use of magnetic trapping.

Long–lived atomic Rydberg states are typically detected using field ionization techniques as described by Tuan *et al.*[19] Here, a beam of neutral rubidium was excited using a frequency doubled, pulsed dye laser, and the np states from $n = 28$ up to $n = 78$ were detected using pulsed field ionization. Low oscillator strengths for transitions to lower levels preclude efficient fluorescence detection.

2.2 Heavy Rydberg systems

With their similarity to electronic Rydberg states, along with a large size and a reduced mass that varies between species, heavy Rydberg systems add a new dimension to the study of Rydberg states with improved temporal and spatial resolution, due to their large size and slow time–evolution. We intend to produce heavy Rydberg systems in lithium; the energy level scheme of which is shown in figure 2.1.

In spite of their intriguing nature, the literature on these novel molecular systems is relatively limited. A good review is provided by Reinhold *et al.*,[2] which includes the development of a mass–scaling law to allow direct comparison of results from conventional and heavy Rydberg systems.

The first observation of bound ion–pair states was by Kalamarides *et al.* in 1976;[20] collisions between Rydberg states of potassium and CF_3I lead to the formation of K^+ and I^- ions, with a small fraction of the ion–pairs forming bound states. This significant observation was noted at the time, only as a mechanism reducing the amplitude of the anion detection signal.

A review of ion–pair spectroscopy is given by Suits *et al.*.[21] Using a VUV laser source to effect dissociation prior to detection of the resulting free ions in a process analogous to photoelectron spectroscopy. When the absorbed energy is sufficient to excite to the continuum, dissociation occurs and the fragments can be detected and their kinetic energy measured using ion imaging. If the absorbed energy is just below the dissociation threshold, pulsed field dissociation may be used in a process termed threshold ion–pair production spectroscopy (TIPPS).[22][23]

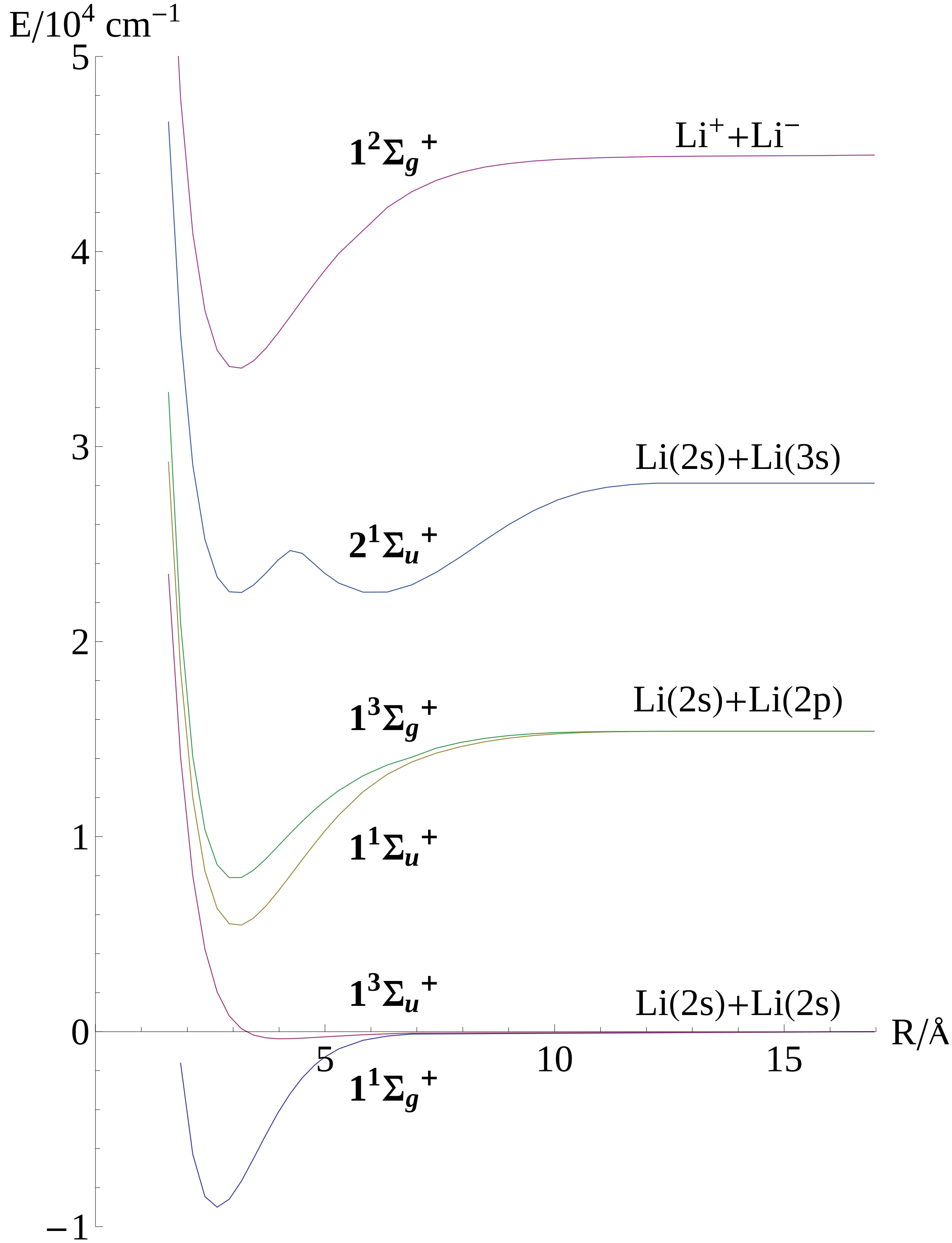

Figure 2.1: Potential energy curves for the Li_2 molecule. Large internuclear separations lead to dissociation, forming free atoms or ions. Curves obtained using published data.[24][25]

Some interesting work, illustrating the virtues of heavy Rydberg systems as subjects for coherent control experiments, was performed by Reinhold *et al.*.[26] Concentrating on the H^+–H^- system, coherent wave–packet evolution was observed on a time–scale orders of magnitude slower than would be expected for a conventional electronic Rydberg state, in accordance with their previously developed mass–scaling law. This results from a reduced mass $\mu \approx m_H/2$, which is far greater than any electronic Rydberg state.

2.3 Development of scientific instruments

The following three chapters detail the design, construction and characterization of electronic and optoelectronic devices. An excellent overview of most areas of electronics is provided by Horowitz and Hill,[27] while Saleh and Teich cover the theory and operation of optoelectronic devices.[28]

The acousto–optic modulator driver developed in chapter 3 is designed using the principles of RF electronics. Good texts covering this area are surprisingly difficult to find, however The Services' Textbook of Radio series, although out of date, provides an excellent grounding in the essential theory and practical details.[29]

There are a number of publications related to the development of optical spectrum analyzers (OSA) such as that developed in chapter 4. Some deal with the optimization of specific components aimed at commercial manufacturers: Borsuk *et al.* developed a design for a dedicated photosensor array for use in optical spectrum analyzers, producing a self–scanned device with 140 pixels having a 12 μm pitch.[30] These specifications would not have been sufficient for our purposes, however the discussion of sensor characteristics applies generally.

A simple, early OSA design was proposed by McIntyre *et al.* based on a monochromator, with a linear photodiode array placed at the exit slit.[31] Modern designs take advantage of technological developments to simplify construction or improve performance. Saitoh *et al.* have developed an OSA using a micro–electro–mechanical mirror mount to vary the angle between the laser beam under test and a fixed diffraction grating; the diffracted light is split into a power reference beam and an étalon transmission beam, which are detected by photodiodes, and the intensity ratio used as a normalized transmission measurement.[32]

Chapter 3

Construction and Characterization of a Driver for an Acousto–Optic Modulator

The practice of experimental atomic and molecular physics relies heavily on the ability to produce laser radiation at a precisely controlled frequency. This facilitates the trapping, cooling, excitation and ionization or dissociation of populations of atoms or molecules.

In order to address particular transitions within the hyperfine structure arising out of interaction between the nuclear magnetic moment and the magnetic field generated by the electron, it is useful to be able to tune the frequency of laser radiation over a range of tens to hundreds of MHz.

In the MOT experiment, we wish to address the D1 and D2 lines within atomic lithium-6 and lithium-7, illustrated in figure 3.1.[33] A laser in the region of either of these transitions can be fine-tuned to any of the specific hyperfine transitions using an acousto-optic modulator (AOM).

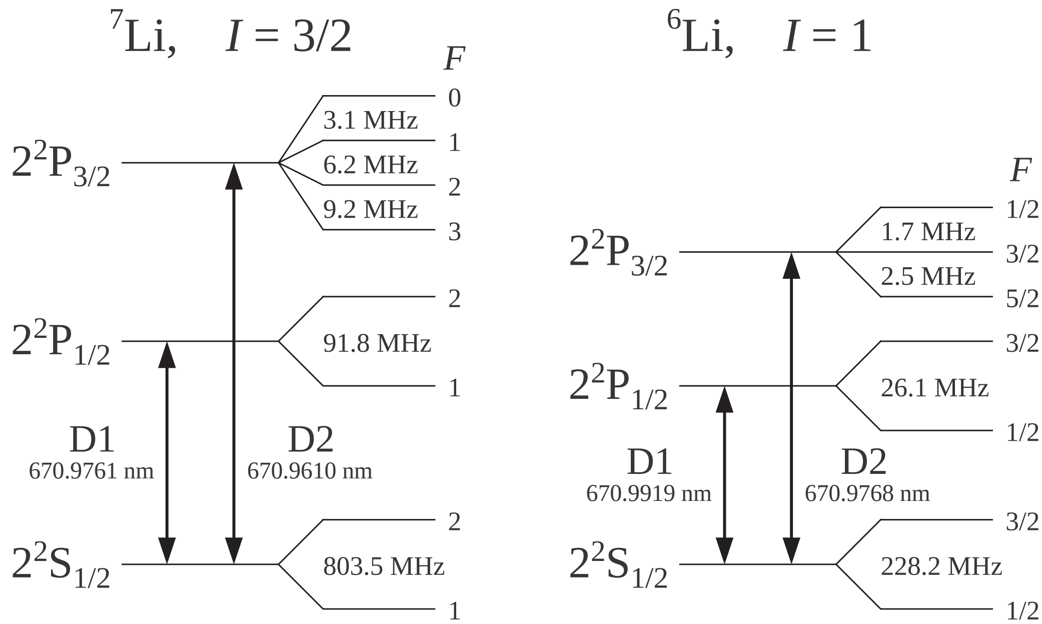

Figure 3.1: Schematic of the energy levels comprising the D1 and D2 lines in the two stable isotopes of lithium. Vacuum wavelengths are given.

3.1 Acousto–optics

The acousto-optic effect is the diffraction of electromagnetic waves by acoustic wavefronts due to Brillouin scattering of photons by acoustic phonons. The compressions and rarefactions constituting the acoustic wave produce variations in refractive index, periodic in both time and space, which can be modelled as a moving diffraction grating that imparts a Doppler shift to the diffracted light.[34]

The interaction length is the length along the direction of propagation of the light over which the electromagnetic wave interacts with the acoustic wave. There are two different diffraction regimes corresponding to different interaction lengths for a given acoustic wavelength, determined by a dimensionless quantity Q, given in equation 3.1,

$$Q = \frac{2\pi\lambda L}{n\Lambda^2}, \tag{3.1}$$

where λ is the optical wavelength in the acousto-optic medium, L is the interaction length, n is the refractive index of the medium and Λ is the acoustic wavelength.[35]

3.1.1 The Bragg regime

The acoustic wave train is effectively a plane wave if its wavelength Λ is small compared to the width of a wavefront (corresponding to $Q \gg 1$). To a first approximation, the acousto–optic effect is similar to Bragg scattering by atomic planes within a crystal lattice, with a Doppler shift due to the motion of the acoustic wave. At a certain angle θ_B between the wavefront and the direction of propagation of the light, the scattered light interferes constructively and forms the frequency shifted beam at an angle of $2\theta_B$ to the incident beam; see figure 3.3 in section 3.1.3 below. The angle θ_B is called the Bragg angle and is given by

$$\sin\theta_B = \frac{\lambda}{2\Lambda}, \tag{3.2}$$

where λ is the wavelength of the light in the acoustic medium and Λ is the wavelength of the acoustic wave.

Light entering the acoustic medium is refracted through an angle given by Snell's law, thus, in practice, we are more interested in the effective Bragg angle θ'_B which takes account of this effect, giving the required angle of incidence on the acoustic medium, given by

$$\sin\theta'_B = \frac{n\lambda}{\Lambda} = \frac{\lambda_0}{\Lambda}, \tag{3.3}$$

where n is the refractive index of the acoustic medium and λ_0 is the vacuum wavelength of the light.

There are different ways one can explain the properties of Bragg diffraction.[36][37] We will use the photon-phonon scattering model. The wave-vector diagram in figure

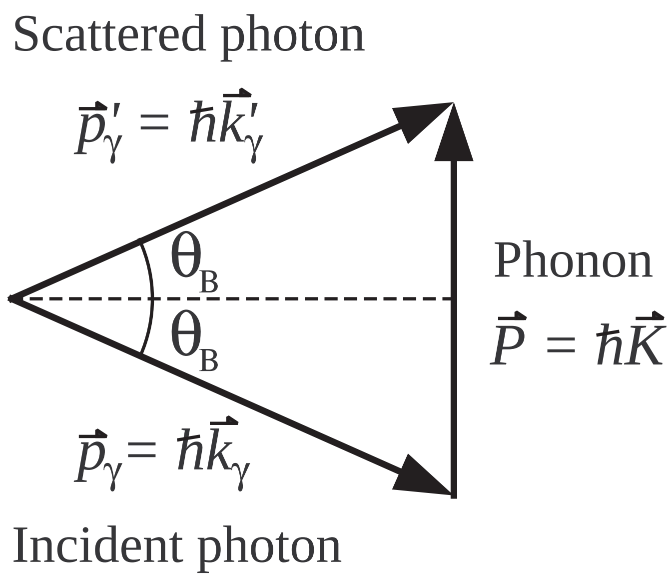

Figure 3.2: Acousto-optic Bragg scattering can be explained by photon–phonon collisions. Conservation of momentum ensures that the scattered photon momentum $\mathbf{p}'_\gamma$ is the sum of the incident photon momentum $\mathbf{p}_\gamma$ and the phonon momentum $\mathbf{P}$. The frequency shift is equal to the acoustic frequency as demonstrated by equation 3.4.

3.2 illustrates a collision between a photon with momentum $\mathbf{p}_\gamma = \hbar\mathbf{k}_\gamma$ and a phonon with momentum $\mathbf{P} = \hbar\mathbf{K}$; the scattered photon has momentum $\mathbf{p}'_\gamma = \hbar\mathbf{k}'_\gamma$. The frequency shift follows if we consider conservation of energy,

$$\begin{aligned} \hbar\omega'_\gamma &= \hbar\omega_\gamma + \hbar\Omega, \\ \Rightarrow \Delta\omega &= \omega'_\gamma - \omega_\gamma = \Omega, \end{aligned} \tag{3.4}$$

where ω is the frequency of the incident light, ω' is the frequency of the diffracted light and Ω is the frequency of the acoustic wave.

The Bragg relation is easily derived if we consider conservation of momentum in the photon–phonon scattering event shown in figure 3.2,

$$\sin\theta_B = \frac{|\mathbf{K}|/2}{|\mathbf{k}_\gamma|} = \frac{\lambda}{2\Lambda}. \tag{3.5}$$

3.1.2 The Raman–Nath regime

If the lateral extent of the acoustic wavefronts is small compared to Λ (corresponding to $Q \ll 1$) then the wavefronts exhibit significant curvature, producing constructive interference at multiple angles of the diffracted beam. This effect is known as Raman-Nath scattering (also known as Debye-Sears scattering) and can be explained by the presence of many plane waves with different directions of propagation, a superposition of which produces the curved wavefront.

For each constituent plane wave, there exists an angle analogous to the Bragg angle, for which the scattered light will interfere constructively, see figure 3.4. The m^{th} order diffraction component is deflected by an angle θ_m and has a frequency ω_m, given by equations 3.6 and 3.7 respectively,

$$\sin\theta_m = -\frac{m\lambda}{\Lambda}, \tag{3.6}$$

$$\omega_m = \omega_0 + m\Omega, \tag{3.7}$$

where ω_0 is the unshifted optical frequency and Ω is the acoustic frequency.[38]

In general, we wish to use AOMs in the Bragg scattering regime, in order to avoid losing intensity due to the presence of higher–order diffraction components. Larger frequency shifts may be efficiently obtained by multiple passes through the acoustic wave.[39] Due to the finite width of the interaction region, we expect to lose some energy to higher–order components.

3.1.3 Acousto–optic modulators

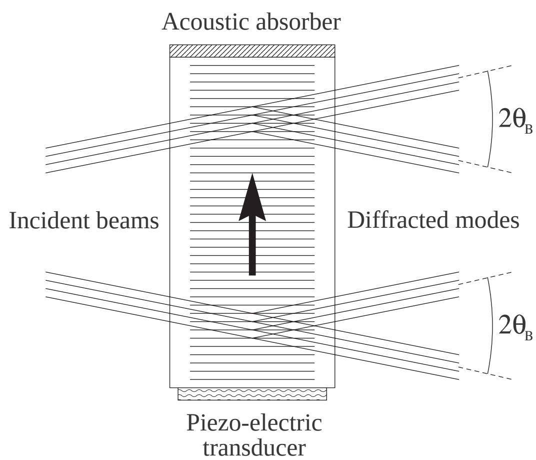

Figure 3.3: An AOM operating in the Bragg regime, showing the incident light downshifted (top) and upshifted (bottom).

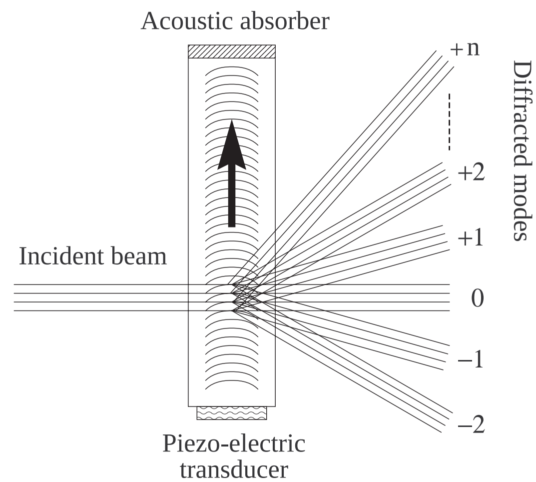

Figure 3.4: An AOM operating in the Raman–Nath regime produces many diffracted orders, both upshifted and downshifted.

Acousto–optic modulators are extremely versatile devices which give some degree of control over every property of light. A single device with a good driver can control the frequency, intensity and phase of the diffracted beam through control of the frequency, amplitude and phase, respectively, of the acoustic wave.[37] The diffracted beam deflection also depends on the acoustic-wave frequency, thus controlling the direction of propagation,[35] while the polarization depends on the amplitude of the acoustic wave.[40]

While our primary interest in AOMs is for frequency shifting, the ability to precisely control the phase of a laser beam without changing the path length greatly simplifies some of the exciting work planned on phase–dependent electromagnetically induced transparency (see chapter 7).

Our acousto–optic modulator

After careful consideration of the available models, the decision was made to purchase an IntraAction ATM–200–1A1,[41] with a tellurium dioxide (TeO_2) crystal providing the acousto-optic medium and a lithium niobate ($LiNbO_3$) piezo-electric transducer used to generate the radio–frequency (RF) acoustic travelling wave. The TeO_2 crystal is coated with a multi-layer dielectric anti-reflection coating, effective across the whole visible spectrum. See table 3.1 for full details.[42]

Table 3.1: Specifications of the IntraAction ATM–200–1A1 AOM

AOM Specifications			
Parameter	Condition	Value	Units
Centre frequency	–	200	MHz
Tuning range	–	100	MHz
Optical wavelength range	–	440–700	nm
Diffraction efficiency	Max.	85	%
Optical rise time	1 mm beam diameter	151	ns
Active aperture height	–	1	mm
Sound velocity	–	4260	ms^{-1}
RF drive power	Max.	1	W
RF input impedance	–	50	Ω
VSWR	Centre frequency	1:1.5	–

3.2 AOM driver

A driver is required to provide a stable RF bias to the piezo-electric actuator producing the acoustic wave. It is instructive to begin with a wish-list defining the qualities of an ideal AOM driver before considering the physical restrictions, engineering practicalities and compromises that are an inevitable part of the design process. Our ideal AOM would have:

- Stable frequency, tunable over the range supported by the AOM
- Narrow bandwidth, minimizes dispersion in the diffracted beam
- Stable amplitude, tunable over the required diffraction efficiency range
- Stable phase, tunable over 360°

In the following discussion, we will see how the choices of components and design parameters affect these characteristics and attempt to optimize them for our purposes.

3.2.1 Design

The basic layout of this design was inspired by the work of V. L. Ryjkov[43] and is illustrated in figure 3.5. A low–power, tunable RF signal is provided by a voltage–controlled oscillator, amplitude control is provided by a tunable attenuator, a low power signal for real-time monitoring is provided through the coupled output of a directional coupler, while the power to drive the acoustic wave–train is provided by an RF–amplifier.

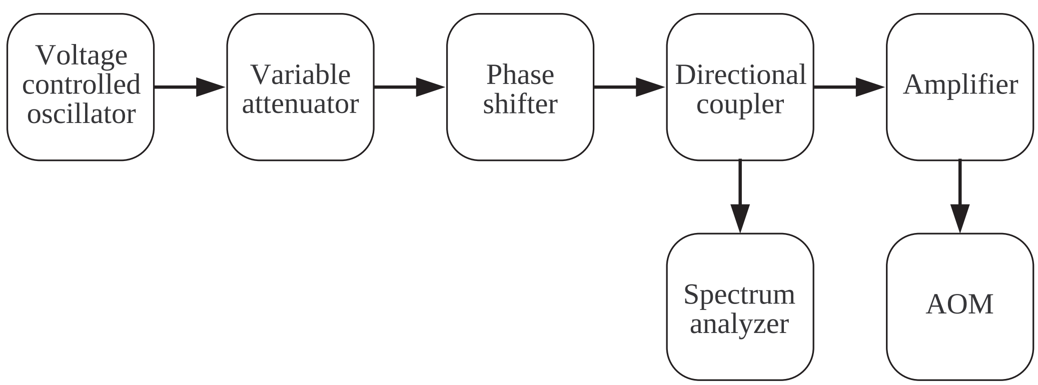

Figure 3.5: Schematic diagram of the AOM driver, showing the main components: a voltage controlled oscillator (VCO), a variable attenuator, a variable phase shifter, a directional coupler and an RF amplifier. A spectrum analyzer can be used to monitor the frequency and power output.

Circuit design

The quote from IntraAction for our AOM, described in section 3.1.3 included details of the ME Series Modulator Drivers.[44] We decided not to purchase a driver for several reasons:

- The specifications do not include amplitude or phase control
- No circuit diagrams are available, complicating any intended modification
- With a footprint of 9 in × 13.25 in, the casing seemed unnecessarily large
- At a cost of US$1125, it seemed unreasonably expensive given the cost of individual components

The RF components used were all purchased from Mini–Circuits[1] and are described in section 3.2.3. The voltage controlled oscillator (VCO) requires a tuning *voltage* of 0–15 V to cover its dynamic range, while the variable attenuator requires a tuning *current* of 0–8 mA. The attenuator datasheet specifies a 0–20 mA tuning current, however the signal was observed to reach its maximum power at around 8 mA.

Initially the intention was to produce a customized version of the IntraAction driver and a circuit diagram was produced including all relevant RF components and control electronics. Many problems were encountered due to cross-talk between different components and subsequent instability; these are described in section 3.2.2.

During a visit to the laboratory of Prof. J. D. D. Martin at the University of Waterloo, useful discussions included the suggestion to use a modular approach. This provides significantly improved isolation between components and increased versatility as different modules can be added and removed at will. Good impedance matching ensures minimal losses on the transmission lines between the modules.

The diagrams for the VCO and attenuator circuits are illustrated in figure 3.6. The RF amplifier was purchased as a complete unit with SMA coaxial connectors,

[1] http://minicircuits.com/, application notes provide a great deal of useful information.

as component level versions did not meet centre–frequency, bandwidth and output–power requirements.

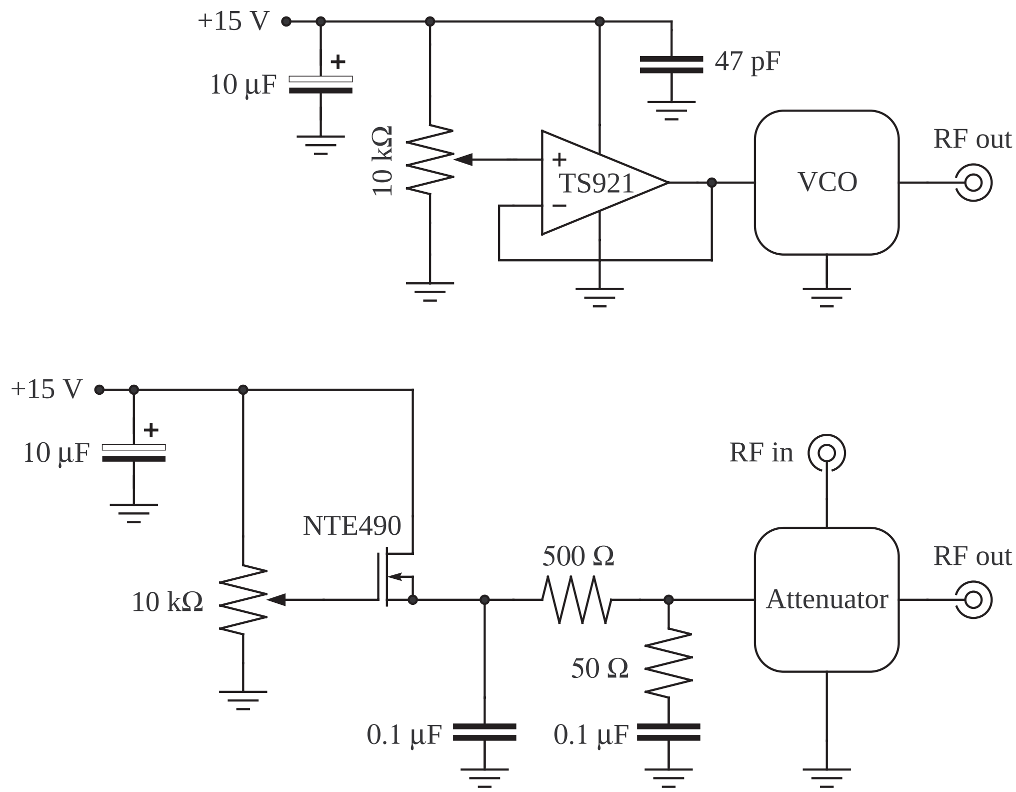

Figure 3.6: Component–level schematic diagram of the voltage–controlled oscillator (VCO) and variable attenuator circuits used in the AOM driver.

3.2.2 RF issues

While the laws of physics remain the same at all frequencies, the circuit techniques employed at high frequencies are often radically different to the familiar DC techniques, as effects such as junction capacitance, wiring inductance and signal wavelength begin to dominate circuit behaviour.

Electromagnetic interference

Long wires and printed circuit board (PCB) traces act as antennae, generating and receiving electromagnetic interference. Shielded enclosures, grounded internal partitions between circuit elements, PCB ground planes and shielded transmission lines all help to reduce electromagnetic coupling which can distort and attenuate high frequency signals.[45]

Shielding used in and around RF circuits works on the same principle as a Faraday cage; free charges in the shielding material are constantly redistributed to cancel any stray electric fields, either external or generated by a nearby section of the circuit.

Grounding

At radio frequencies, solid grounding is essential; stray inductances can lead to high impedance on a return line resulting in floating grounds at different potentials in different sections of a circuit. Internal shielding must be soldered along its entire length, and partitions and covers require many screws to maintain a good chassis ground.

A potential difference between two points supposedly held at ground can lead to ground loops. This can be particularly problematic for RF circuits, causing spurious signals due to return line oscillations and coupling to and from conductors expected to carry only DC signals. The grounded shielding described in **Electromagnetic interference**, section 3.2.2, can provide paths for ground loops. A separate connection to the common ground terminal is provided for each RF component to minimize current flow through the casing.

Skin depth

At high frequencies, current tends to be restricted to regions near the surface of a conductor; a phenomenon known as the skin effect. From Maxwell's equations for a linear, conducting medium, we have,

$$\nabla.\mathbf{E} = \frac{\rho}{\epsilon_0}, \tag{3.8}$$

$$\nabla \times \mathbf{E} = -\frac{\partial \mathbf{B}}{\partial t}, \tag{3.9}$$

$$\nabla.\mathbf{B} = 0, \tag{3.10}$$

$$\nabla \times \mathbf{B} = \mu_0 \epsilon_0 \frac{\partial \mathbf{E}}{\partial t} + \mu_0 \mathbf{J}, \tag{3.11}$$

where, for a non–magnetic conductor, the bound charge and polarization currents are negligible compared with the free charge current, giving a total current density

$$\mathbf{J} \approx \sigma \mathbf{E}. \tag{3.12}$$

Using the vector identity,

$$\nabla \times \nabla \times \mathbf{A} = \nabla(\nabla.\mathbf{A}) - \nabla^2 \mathbf{A}, \tag{3.13}$$

and noting that the gradient of the charge density, ρ, is zero in a conductor, we can obtain the wave equation for the electric field in a conducting medium,

$$\nabla^2 \mathbf{E} = \mu_0 \epsilon_0 \frac{\partial^2 \mathbf{E}}{\partial t^2} + \mu_0 \sigma \frac{\partial \mathbf{E}}{\partial t}. \tag{3.14}$$

There is a plane wave solution to the wave equation given, for a wave propagating in the positive z–direction, by

$$\tilde{\mathbf{E}}(z,t) = \tilde{\mathbf{E}}_{\mathbf{0}} e^{i(\tilde{k}z - \omega t)}, \tag{3.15}$$

with a complex wavenumber,

$$\tilde{k} = k_R + ik_I, \tag{3.16}$$

which leads to an exponential decrease in electric field amplitude as the field penetrates the conductor,

$$\tilde{\mathbf{E}}(z,t) = \tilde{\mathbf{E}}_{\mathbf{0}} e^{-k_I z} e^{i(k_R z - \omega t)}. \tag{3.17}$$

The skin depth d is the characteristic length of the exponential decay,

$$d = \frac{1}{k_I}, \tag{3.18}$$

where k_I comes from the solution to equation 3.14,

$$k_I = \omega\sqrt{\frac{\epsilon_0\mu_0}{2}}\left[\sqrt{1+\left(\frac{\sigma}{\epsilon_0\omega}\right)^2} - 1\right]^{1/2}. \tag{3.19}$$

For good conductors such as the annealed copper used for the internal wires in the AOM driver, we can simplify equation 3.19 and substitute it into equation 3.18 to give:[46]

$$d \approx \sqrt{\frac{2}{\mu_0\sigma\omega}}. \tag{3.20}$$

Inserting the values for the conductivity ($\sigma \approx 60$ MSm^{-1}) and permeability ($\mu \approx \mu_0$) of copper, along with the centre frequency of the AOM (200 MHz) we obtain a skin depth $d \approx 4.6$ μm. For wires with a diameter D much greater than the skin depth, the AC resistance is equal to that of a hollow cylindrical conductor with the same outer diameter and with thickness d,

$$R_{AC} \approx \frac{\rho L}{\pi d(D-d)} \approx \frac{\rho L}{\pi d D}. \tag{3.21}$$

The multi–core wire that was used consisted of seven circular cross–section conductors with a combined area of 0.22 mm^2, and has an effective area approximately 2.6 times larger than a solid conductor of equivalent cross–sectional area.

Transmission lines

An RF transmission line consists of two conductors (with one held at RF ground) separated by a dielectric; the two most common geometries are twisted pair and coaxial, and each has its own specific characteristics. Two of the key attributes determining the behaviour of a transmission line are the capacitance per unit length $\mathcal{C}$ and the inductance per unit length $\mathcal{L}$. The characteristic impedance is given by,

$$Z_0 = \sqrt{\frac{\mathcal{L}}{\mathcal{C}}}. \tag{3.22}$$

To elucidate the effect of a given characteristic impedance between a source and a load, we will consider a model system composed of an RF voltage source with impedance $Z_S = 50\ \Omega$, a twisted pair transmission line with characteristic impedance $Z_0 = 100\ \Omega$ and a resistive load with impedance $Z_L = 50\ \Omega$; the system is illustrated in figure 3.7.

For a twisted pair transmission line (see figure 3.8) the relevant attributes can be calculated using the following equations,[47]

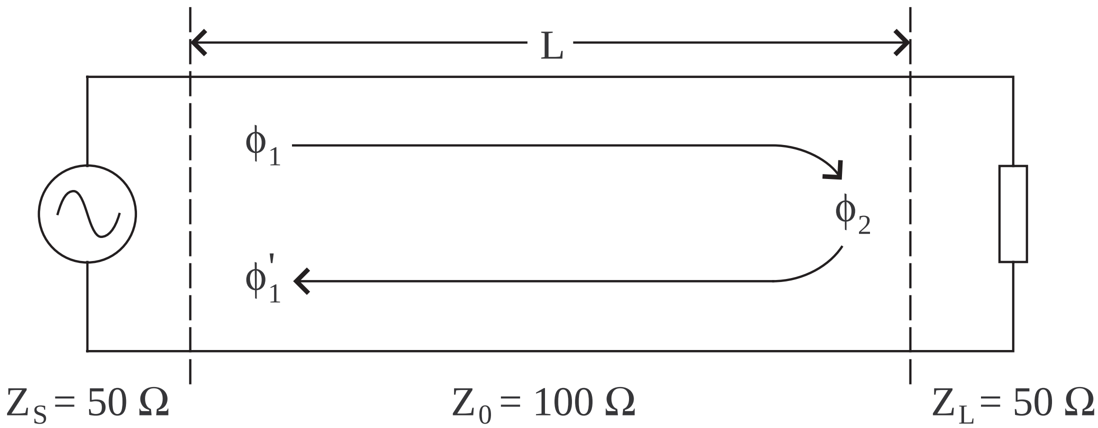

Figure 3.7: A model RF circuit with source impedance Z_S, a twisted pair transmission line of length L and characteristic impedance Z_0 and a resistive load with impedance Z_L. The phase of the RF travelling wave has been labelled as it enters the transmission line (ϕ_1), on reflection from the load junction (ϕ_2) and on its return to the source junction (ϕ'_1).

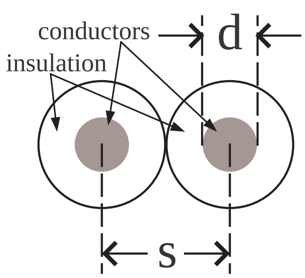

Figure 3.8: Geometry of a twisted pair transmission line.

$$\mathcal{L} = \frac{\mu_0}{\pi}\cosh^{-1}\left(\frac{s}{d}\right) \tag{3.23}$$

$$\mathcal{C} = \frac{\pi\epsilon_0\epsilon_r}{\cosh^{-1}\left(\frac{s}{d}\right)} \tag{3.24}$$

$$\Rightarrow Z_0 = \frac{c\mu_0}{\pi\sqrt{\epsilon_r}}\cosh^{-1}\left(\frac{s}{d}\right) \tag{3.25}$$

Using these values, the velocity factor $VF = v/c$ can be calculated,

$$VF = \frac{1}{c\sqrt{\mathcal{L}C}} = \frac{1}{\sqrt{\epsilon_r}}. \tag{3.26}$$

Note that for our model system there is an impedance mismatch at both ends of the transmission which will lead to partial reflection of the RF signal. This can be expressed quantitatively in terms of the voltage standing wave ratio (VSWR). The interference of the incident and reflected signals produces a standing wave; the VSWR is the ratio of the net voltage amplitude at a maximum to the net amplitude at an adjacent minimum.

We can define a complex reflection coefficient which is the voltage ratio of the reflected V_r and incident V_i waves:

$$\tilde{\Gamma} = \frac{\tilde{V_r}}{\tilde{V_i}} = \frac{|\tilde{V_r}|}{|\tilde{V_i}|} e^{j(\phi_r - \phi_i)} \tag{3.27}$$

It is instructive to examine the behaviour of the signal at a termination for three cases in which $\tilde{\Gamma}$ is entirely real, and in the general case:

- Open circuit ($Z_L = \infty$): $\tilde{\Gamma} = 1$, maximum reflected amplitude, no phase shift
- Matched impedance ($Z_L = Z_0$): $\tilde{\Gamma} = 0$, no reflection
- Short circuit ($Z_L = 0$): $\tilde{\Gamma} =$ -1, maximum reflected amplitude, π phase shift
- General case: reflected amplitude $|V_r| = |V_i||\tilde{\Gamma}|$, phase shift $\phi_r = \phi_i + \phi_\Gamma$

In order to calculate the VSWR we need the voltage amplitude at a maximum V_{MAX} and an adjacent minimum V_{MIN},

$$V_{MAX} = V_i + V_r = V_i(1 + |\tilde{\Gamma}|),$$
$$V_{MIN} = V_i - V_r = V_i(1 - |\tilde{\Gamma}|),$$

$$\Rightarrow VSWR = \frac{1 + |\tilde{\Gamma}|}{1 - |\tilde{\Gamma}|}. \tag{3.28}$$

A high VSWR leads to high RF losses due to the finite resistance of the transmission line. Multiple reflections effectively increase the length of the transmission line; there is energy stored in the standing wave in addition to the transmitted power. A matched impedance minimizes these losses and therefore maximizes the power dissipated in the load.

The model system was constructed using a Mini–Circuits POS–300 VCO as the source (output impedance 50 Ω, nominal output power 9.5 mW at 200 MHz) and a Hameg HM5012-2 spectrum analyzer as the load (input impedance 50 Ω) connected by a length of homemade twisted pair cable ($\epsilon_r \approx 2.8 \Rightarrow Z_0 \approx 100$ Ω, see equation 3.25). As the length L of the transmission line is varied we expect the power supplied to the spectrum analyzer to oscillate as we pass through maxima and minima, see figure 3.9.[29]

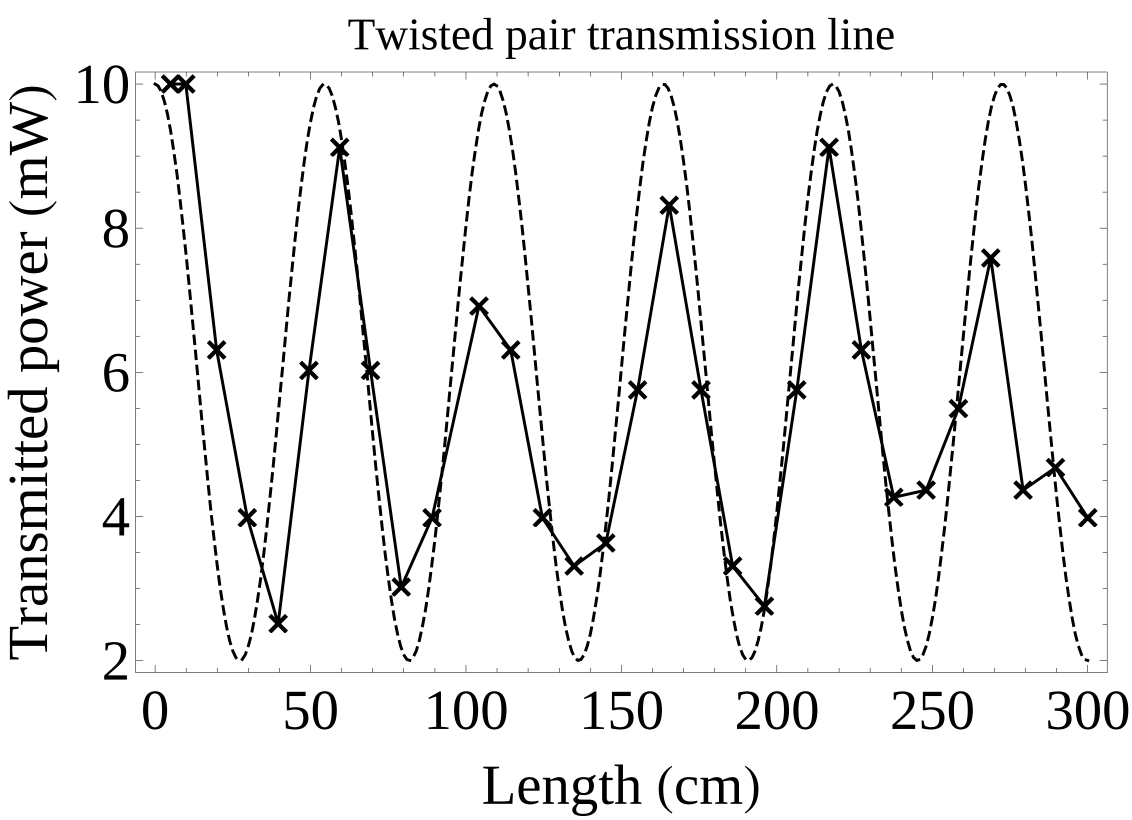

Figure 3.9: An analysis of power transmitted by a twisted pair transmission line of varying length, with a 9.5 mW source at 200 MHz and a 50 Ω load.

The maxima in the power transmission occur when the incident and reflected waves interfere constructively ($\phi_1' - \phi_1 = 2m\pi$ where m is an integer, see figure 3.7).

The phase relationship can be calculated in terms of the RF wavelength λ_{RF},

$$\phi_2 = \phi_1 + \frac{2\pi L}{\lambda_{RF}},$$
$$\phi_1' = \phi_2 + \frac{2\pi L}{\lambda_{RF}},$$
$$\Rightarrow \phi_1' = \phi_1 + \frac{4\pi L}{\lambda_{RF}},$$

thus we can deduce the lengths for which we expect maximum power transmission,

$$L = \frac{m\lambda_{RF}}{2} \tag{3.29}$$

To check the data, we obtain a formula for L in terms of the velocity factor $VF = v/c$,

$$\lambda_{RF} = \frac{c\,VF}{\nu}, \tag{3.30}$$
$$\Rightarrow L = \frac{mc\,VF}{2\nu}, \tag{3.31}$$
$$\Rightarrow VF = \frac{2\nu}{c}(L_{m+1} - L_m). \tag{3.32}$$

Using the data illustrated in figure 3.9 we obtain an experimental value $VF_{exp} = 0.73$, which we can compare with a theoretical value obtained from equation 3.26, $VF_{th} = 0.60$. This discrepancy is mostly likely due to errors in the length measurements caused by inconsistency in the pitch.

Decoupling capacitors

In precision RF circuits, liberal use of decoupling capacitors can significantly improve performance; two types of capacitor are used in the AOM driver circuits for this purpose.

- *Ceramic disk capacitors* are suitable for high frequency signals. 47 pF ceramic disk capacitors are used to provide a path to ground for any stray RF signals that might otherwise couple into a DC section of the circuit.

- *Electrolytic capacitors* are available with high values, but have poor high frequency characteristics. 10 μF electrolytic capacitors are used to provide a path to ground for power line fluctuations which would otherwise cause instability in the control electronics for the VCO and attenuator.

3.2.3 Construction

The modular design of the system greatly simplified construction, allowing individual sub–systems to be tested individually using a basic VCO circuit as a high frequency signal generator and monitoring the output on a spectrum analyzer.

Components

Table 3.2: List of Mini-Circuits RF components for the AOM driver.

AOM driver components			
Component	Model	Characteristic	Range
Voltage–controlled oscillator	POS–300	Output frequency	150 $\rightarrow$ 280 MHz
Variable attenuator	PAS–1	Signal attenuation	3.6 $\rightarrow$ 50 dB
Variable phase shifter	ELS–450	Phase shift	0 $\rightarrow$ 360°
Directional coupler	PDC–20–3	Mainline loss	0.35 $\rightarrow$ 0.6 dB
RF amplifier	ZFL–1000VH	Gain	21.6$\pm$0.5 dB

All RF components were sourced from Mini-Circuits due to the author's prior familiarity with their range. It should be noted that components from other manufacturers may offer equivalent or superior performance.

Printed circuit boards

The printed circuit board (PCB) designs were produced using the EAGLE electronic design package, an almost fully functional version of which is available free for non–commercial use.[2] EAGLE contains a set of libraries including many commonly–used electronic devices with associated schematic symbols, and board layouts for specific models; for specialist components such as the RF devices, a set of tools is provided to create custom libraries.

One of the key design considerations was provision of appropriate grounding for each module in the device, thus a ground plane was included that separated all components, signal lines and power lines. The PCB layout is shown in figure 3.10.

The completed device

Figure 3.11 shows the completed system. The modular design allows individual sub–systems to be removed; the minimal required system consists of the VCO to produce the RF signal, and the RF amplifier to increase the signal amplitude to provide enough power to drive the piezo–electric actuator within the AOM.

3.2.4 Characterization

Having completed construction of the AOM driver, data was collected to assess the performance of the device under varying conditions. The tests performed fall into two categories: electrical tests performed on the driver, and optical tests to assess the capabilities of the AOM controlled by the driver.

[2] http://www.cadsoft.de/freeware.htm

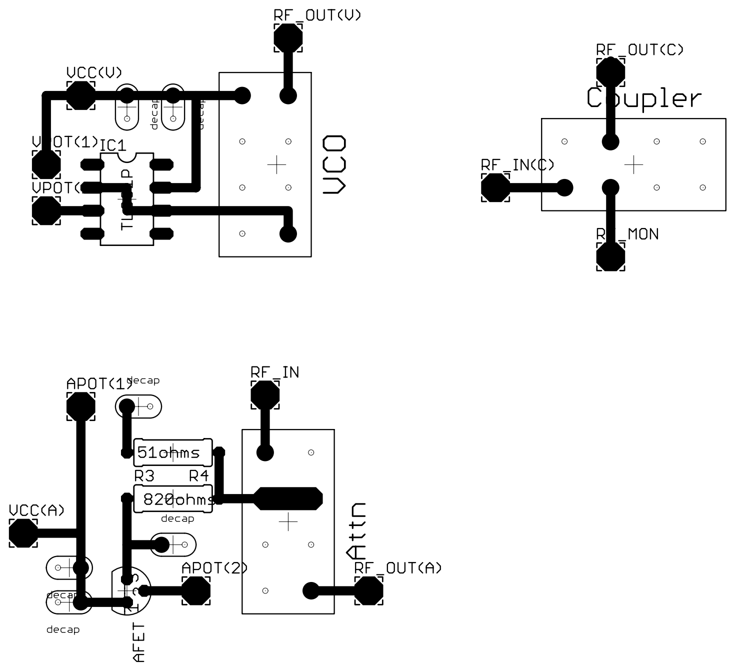

Figure 3.10: Diagram illustrating the printed circuit board (PCB) layouts for the voltage–controlled oscillator (VCO), variable attenuator (Attn) and directional coupler (Coupler) circuits used in the AOM driver. The ground plane has been omitted for clarity.

Electronic testing

The attenuator requires a control current provided through an n-channel FET as shown in figure 3.6. During testing of how diffraction efficiency depends on RF power it became clear that the attenuation varies in an extremely non–linear way as the controlling potentiometer is adjusted. In order to quantify this, measurements were taken to assess how tuning current and output power vary as the potentiometer is adjusted; the results are shown in figures 3.12 and 3.13 respectively.

The current source providing the tuning current is extremely linear for the range 2–30 mA; one can conclude that the non–linear change in diffraction efficiency is due to a non–linear relationship between attenuation and tuning current. It may be worth attempting to provide a non–linear tuning current in order to “smooth out” the attenuation curve to some extent.

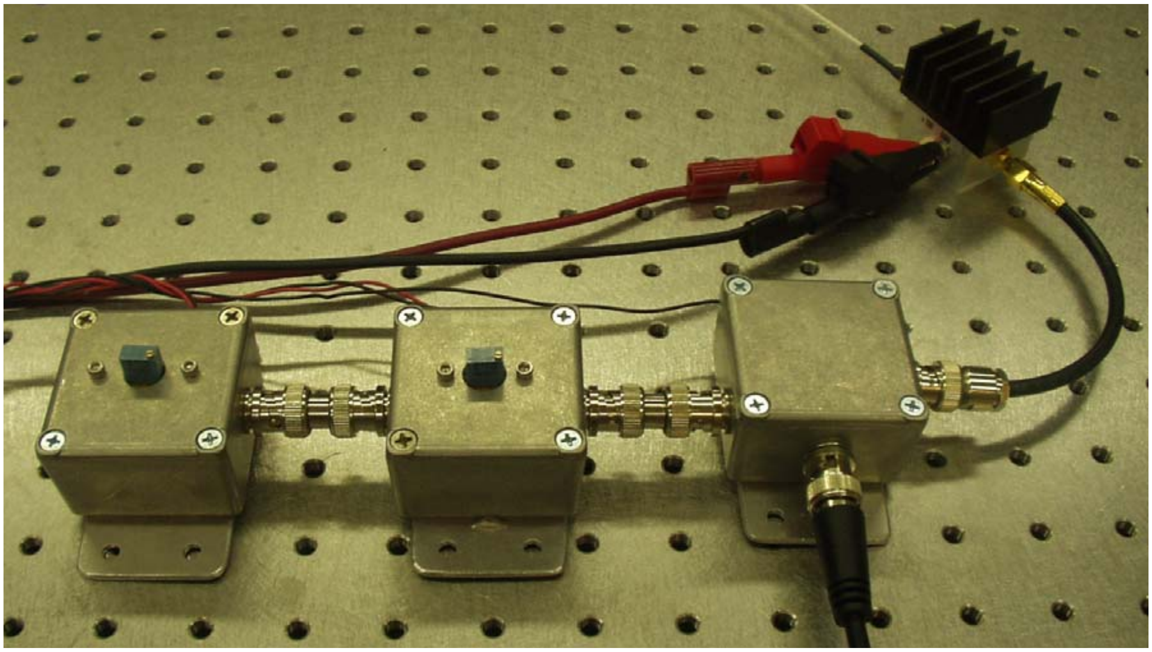

Figure 3.11: Image of the AOM driver including (from the left) the VCO unit and variable attenuator (both with control potentiometers), the directional coupler (with low power coupled output a the base of the image) and the RF amplifier.

Optical testing

An acousto–optic modulator is a device used to control the properties of laser light. As such, the most important tests are those which determine the effect of the device on a laser beam passing through the acoustic wave. Optical testing was accomplished using the light from an external cavity diode laser (ECDL) at 670 nm,[48] and a Coherent LaserMate–Q laser power meter.

Due to variation in the VCO power output as it is tuned off its centre frequency, as well as small variations in amplifier gain (less than 0.1 dB over the VCO frequency range), one expects to see frequency dependent changes in the diffraction efficiency. Figure 3.14 shows the diffraction efficiency spectrum which remains fairly flat at just over 50 % within the 150 $\rightarrow$ 280 MHz range stated in the VCO datasheet.

The variable attenuator is provided to allow direct tuning of the diffraction efficiency and hence provide control over the intensity of the diffracted beam. Figure 3.15 illustrates the dependence of diffraction efficiency on RF power supplied to the

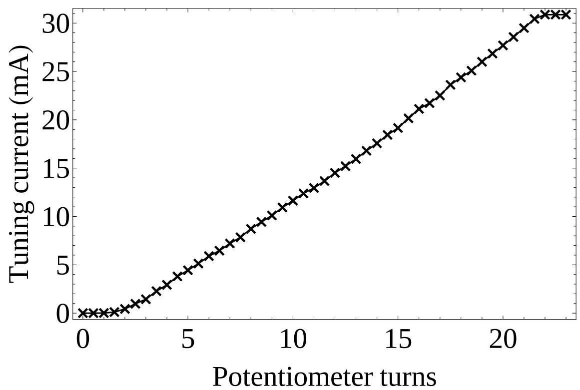

Figure 3.12: The current provided by the FET in the attenuator circuit in figure 3.6 is linear over most of the range, however the attenuation only varies below 8 mA.

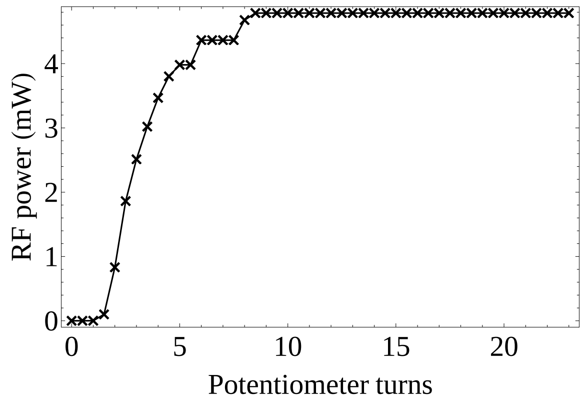

Figure 3.13: Tuning the RF power supplied to the amplifier using the attenuator. The steps are caused by the 0.4 dBm resolution of the spectrum analyzer used to take the measurements.

AOM. The RF power was monitored from the coupled output and the actual power delivered was calculated from the specifications of the directional coupler, assuming 18 dB amplifier gain. The stated maximum output power of the amplifier is 25 dBm, causing the roll off at high power.

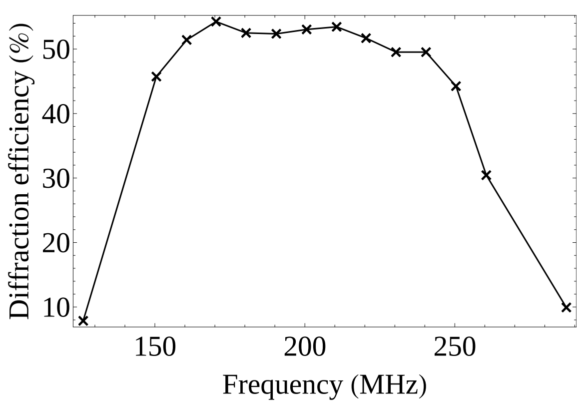

Figure 3.14: Establishing the dependence of diffraction efficiency on acoustic frequency for the AOM–driver system, using a diode laser at 670 nm.

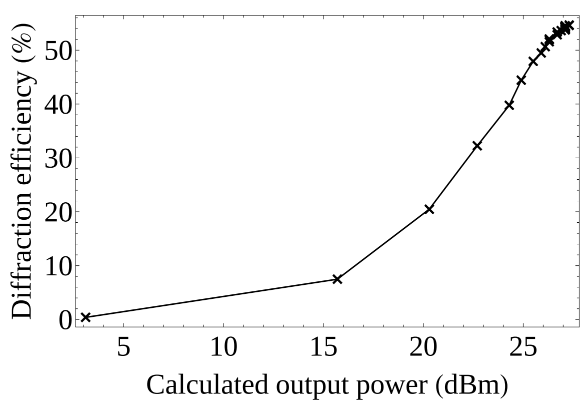

Figure 3.15: Tuning the diffraction efficiency of the AOM–driver system, using the variable attenuator included in the AOM driver. Frequency = 200 MHz.

Chapter 4

Real Time Laser Mode Structure Analysis

One of the many advantages of using lasers as a light source for addressing transitions in atoms and molecules is their extremely narrow bandwidth. The actual frequencies emitted by a laser subject to inhomogeneous broadening due to the effects of the velocity distribution, spatial field inhomogeneities, or the presence of impurities in the gain medium, are given by the product of the active medium gain profile and the allowed modes of the laser cavity; see figure 4.1.[49]

Figure 4.1: Diagram illustrating the origin of the observed mode–structure of a typical laser. The product of the gain profile with the spectrum of allowed cavity modes produces the characteristic "peaks under a curve" spectrum.

For applications requiring precise frequency control, it is important that the laser radiation includes only a single longitudinal cavity mode; there are many locking techniques used to achieve this.[50][51][52][53]

As no frequency locking system is totally reliable, it is extremely useful to have a way of monitoring laser mode structure in real time over the course of an experiment. The typical approach uses an optical spectrum analyzer (OSA) which varies the separation between a pair of highly reflecting mirrors, arranged as a Fabry–Pérot interferometer, and detects the transmitted intensity from incident laser light. While this system is simple to use and effective, it is expensive, requires a dedicated oscilloscope, and occupies a large footprint, making it impractical to provide one for each laser system required to operate on a single mode.

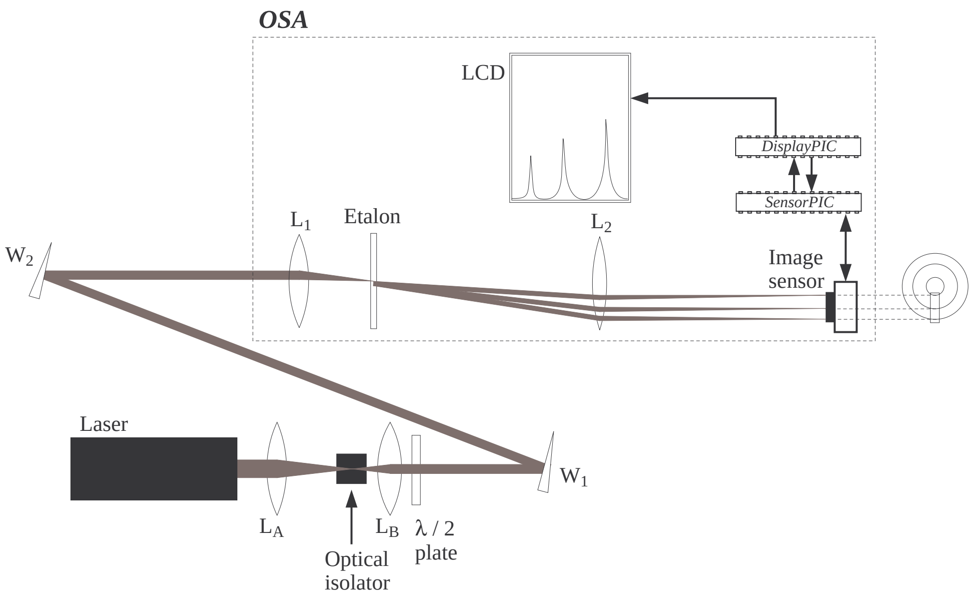

Figure 4.2: The experimental setup illustrating the optical train which produces the Fabry–Pérot interference pattern, the digital image sensor used to record the pattern, the microcontrollers which record and reformat the data and the LCD used to display the resulting trace. Lenses L_A and L_B focus the beam through an optical isolator and subsequently recollimate it. Optical wedges W_1 and W_2 have approximately 4 % reflectivity at 670 nm, leaving 0.16 % of the initial beam incident on the OSA. Lens L_1 ensures a high intensity beam illuminates the étalon, while lens L_2 both focuses the individual fringes onto the image sensor, and collimates the beam.

In this chapter, a novel system is presented which has been constructed in our laboratory with a device cost and footprint which make it realistic to provide one for each laser system. A diagram illustrating the concept is shown in figure 4.2. A low power laser beam, which may be obtained from the back reflection off any uncoated optical element, incident on a solid étalon produces a spatially varying interference pattern characteristic of the laser mode structure. The Fabry–Pérot pattern illuminates a CMOS digital image sensor, the data is recorded and reformatted by a pair of programmable microcontrollers and displayed on a component level LCD.

4.1 Producing an interference pattern

A laser beam incident on an étalon at a range of angles produces a stationary interference pattern. As the pattern is circularly symmetric, all of the information can be obtained in a radial scan. Accordingly, the image sensor is placed such that the pattern is vertically aligned with its central row, with the edge of the sensor pixel array positioned between the centre of the pattern and the first order fringe.

The optical train we have used to obtain the interference pattern is included in figure 4.2. The laser beam is focused through an optical isolator, a second lens ensures the resulting beam is parallel. Reflection from a pair of optical wedges reduces the beam power to approximately 4 μW before it is focused onto the étalon. The beam has a width $d_1 = 2.5$ mm at lens L_1 and a width $d_2 = (f_2/f_1)d_1 = 8$ mm at the image sensor, which has an active area width of 6.66 mm. The fringe of order p is focused at the back focal plane of lens L_2 with a diameter given by

$$D_p^2 = \frac{4f_2^2 n' \lambda}{n^2 h}(p - 1 + \varepsilon), \tag{4.1}$$

where λ is the wavelength of the light, h is the thickness of the étalon, f_2 is the focal length of lens L_2, n and n' are the refractive indices outside and inside the étalon respectively, and ε is the excess fraction.[54] Lens L_2 is chosen such that three intensity peaks can fit within the active width of the image sensor. This ensures that at least two fringes are always visible, clearly delineating a free spectral range.

4.2 The image sensor

The device used to record the interference pattern is a Micron MT9M001C12STM 1.3 megapixel CMOS digital image sensor,[55] with 1024 rows $\times$ 1280 columns (SXGA). Inputs and outputs are entirely digital, using low power 3.3 V logic. Intensity values are provided on a 10–bit wide bus (of which 8 bits are used) synchronized with an external clock source, which must lie within the range 1 to 48 MHz. This clock is provided by a microcontroller configured to output a clock signal at $1/4$ of its 8 MHz internal clock frequency, giving a sensor clock frequency of 2 MHz.

A commercial digital camera would not give direct access to the digital intensity values for each pixel, would be challenging to synchronize with a microcontroller due to the internally generated clock signal, and, in general, would not give direct access to the windowing capabilities required to read data from a narrow strip across the sensor array.

A CMOS image sensor consists of a two–dimensional array of photodiodes which accumulate charge at a rate proportional to the intensity of incident light within a certain spectral range. The primary difference between a CCD and a CMOS image sensor lies in the way the charge is read by the associated electronics. CCDs transport the charge across the chip so that it can be read off pixel–by–pixel using a transistor placed at a corner of the array. Achieving this without significant distortion requires a special manufacturing process which is incompatible with the CMOS class of integrated circuits. A CMOS image sensor has readout transistors integrated into each pixel, obviating the need for charge transport.[56]

Three major practical advantages of a CMOS image sensor over a CCD are the low power consumption due to simpler control electronics, low cost due to the ubiquity of the CMOS manufacturing process, and easy integration of ADC allowing CMOS sensors to give a digital output. CCDs can have a higher resolution as the entire active area consists of a photodiode array without the need for the associated readout transistors. The requirement for a digital output that can be read directly by a microcontroller proved to be the decisive factor in choosing a CMOS image sensor over a CCD.

4.2.1 Configuration settings

The image sensor contains a set of programmable 16–bit registers which are used to control internal settings such as gain, pixel integration time and windowing. The value of the registers are set through a two–wire serial interface using the I^2C (Inter–Integrated Circuit) protocol. See section 4.4.4 for details on how the serial communication was implemented.

Table 4.1: Micron MT9M001C12STM image sensor, configuration registers.

Register list with hex values			
Register #	Description	Default value	Chosen value
0x01	Row start	0x000C	0x01F4
0x02	Column start	0x0014	0x0014
0x03	Window height - 1	0x03FF	0x0002
0x04	Window width - 1	0x04FF	0x04FF
0x05	Horizontal blanking	0x0009	0x0000
0x06	Vertical blanking	0x0019	0x0000
0x09	Shutter width	0x0419	0x000A
0x0C	Shutter delay	0x0000	0x0000

Windowing

In order to implement a one–dimensional, radial scan of the interference pattern, only a single row of pixels is required. While linear photodiode arrays are available for specialist applications in spectroscopy, two–dimensional arrays used for photographic applications are inexpensive and widely available with a resolution higher than any linear array found to date. In order to use a two–dimensional image sensor, the active window is set to span the entire 6.66 mm active width, using the minimum height of just three rows. With a pixel spacing of 5.2 μm in both the horizontal and vertical directions, the effects of fringe curvature should be minimal.

Four registers control the window position and dimensions, setting the first row, first column, window height and window width. The first column and window width parameters are left as their default values, ensuring the entire width of the pixel array is utilized. The first row to be read is number 500 (hex value 0x01F4), approximately half way down the array; a value of two (0x0002) in the third register selects the three row window height.

Blanking

In addition to the region of optically black pixels surrounding the active area, the image sensor has the capability to blank a specified number of pixels at the beginning of each row (horizontal blanking) and a specified number of rows at the end of each frame (vertical blanking), to allow the active area to be changed without altering the dimensions of the pixel array, or the pixel integration time. The sensor outputs LINE_VALID and FRAME_VALID signals which remain low during horizontal and vertical blanking respectively.

The total frame time includes the time spent in the blanked regions; this overides previous window settings. The horizontal and vertical blanking registers have both been set to zero to maximize the frame rate, giving maximum flexibility in the display refresh rate.

Pixel integration time

The pixel sensitivity can be controlled by adjusting the period during which charge is accumulated in the photodiodes prior to readout; the period t_{INT} is specified as a number of sensor clock periods,

$$t_{INT} = (\text{Reg0x09} \times \text{row time}) - \text{overhead time} - \text{reset delay}, \tag{4.2}$$

where

$$\begin{aligned} \text{row time} &= [(\text{Reg0x04} + 1) + 244 + \text{Reg0x05} - 19] \times \tau_{CLK}, \\ \text{overhead time} &= 180 \times \tau_{CLK}, \\ \text{reset delay} &= 4 \times \text{Reg0x0C} \times \tau_{CLK}. \end{aligned}$$

The default shutter width 0x0419 (1049 lines) allows charge to accumulate for a full frame period giving maximum sensitivity. The shutter width is reduced to 0x000C (12 lines, $t_{INT} = 7.55$ ms) matching the sensitivity to the incident laser power and avoiding saturation due to ambient light.

4.2.2 Image sensor characterization

An experiment was performed to assess the variation in pixel sensitivity across the active width of the sensor. The program implemented on the microcontrollers was modified to record the maximum intensity detected by each pixel (see **Program extensions**, section 4.4.4 for details); a flashlight incident on a 300 μm circular aperture was used as a constant intensity light source while the sensor was translated through the beam. The fractional variation ($\sigma_{n-1}/\langle I \rangle$) in the intensity I was found to be 1.4 %.

4.2.3 The image sensor circuit

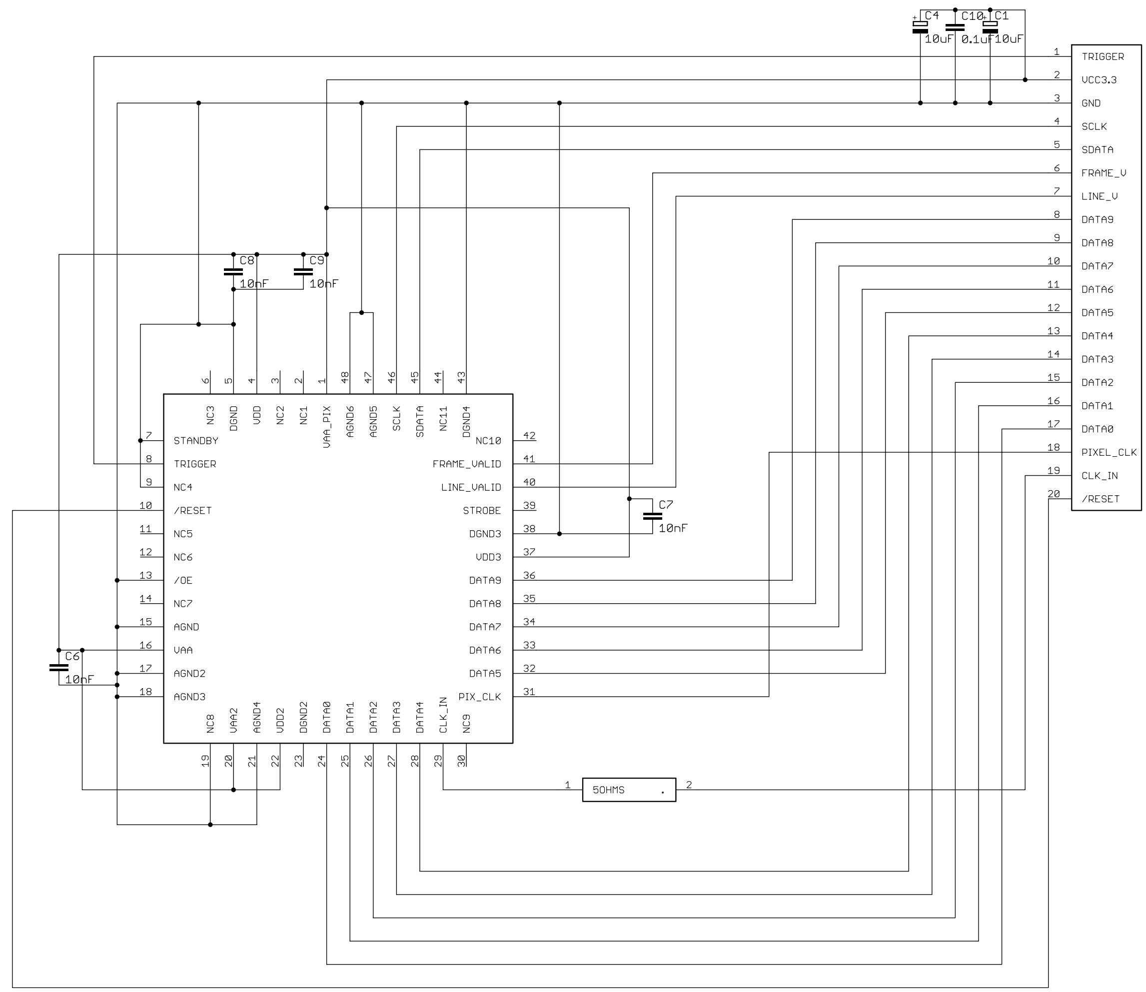

Figure 4.3: Schematic diagram of the image sensor circuit including the sensor, a ZIF connector for a 20–contact ribbon cable along with capacitors for signal conditioning. The "/" symbol denotes a signal which produces its effect during a logic zero.

The image sensor is housed in a 48–pin plastic leadless chip carrier (PLCC), a square surface mount package with twelve contacts along each side. Rather than soldering directly on to the board, a through–hole socket[1] was purchased, greatly simplifying board assembly and sensor replacement.

The sensor circuit includes a number of decoupling capacitors to reduce noise on the various signal lines and a 20–contact, vertical, zero insertion force (ZIF) connector

[1] Loranger International Corporation, part number 04440 481 X215.

for a 1 mm pitch ribbon cable used to transmit the signal lines to the main system board. The circuit diagram is shown in figure 4.3, while the layout of the board is depicted in figure 4.4.

The ribbon cable includes a 10–bit wide bus for the intensity data, of which only the eight most significant bits are used. The microcontroller inputs and outputs are arranged as 8–bit ports which can be addressed in a bytewise fashion (See section 4.4.3); obtaining the full 10–bit resolution would require a disproportionate increase in processing time. See section 4.6 for discussion of possible improvements to this system.

4.3 The display

The LCD used to display the mode structure information is an Optrex F–51477GNB–FW–AD with 240 rows $\times$ 320 columns. In order to produce a plot of intensity as a function of position on the image sensor, data points must be plotted consecutively according to their x–values; as the display must be written to sequentially by row, the display is rotated such that the y–axis, representing the intensity values, is the long axis. The 8–bit resolution of the intensity data leads to a dynamic range of 256 on the y–axis, similar to many commercial oscilloscope displays.

Every fifth sensor pixel is represented by a corresponding row on the display, such that the 240 rows of the display represents the width covered by 1200 out of the 1280 pixels spanning the active region of the sensor. The row position corresponds to the position of the sensor pixel; a marker is placed on each row such that the top of the marker indicates the intensity value and the length is set to ensure a continuous curve; see section 4.4.4.

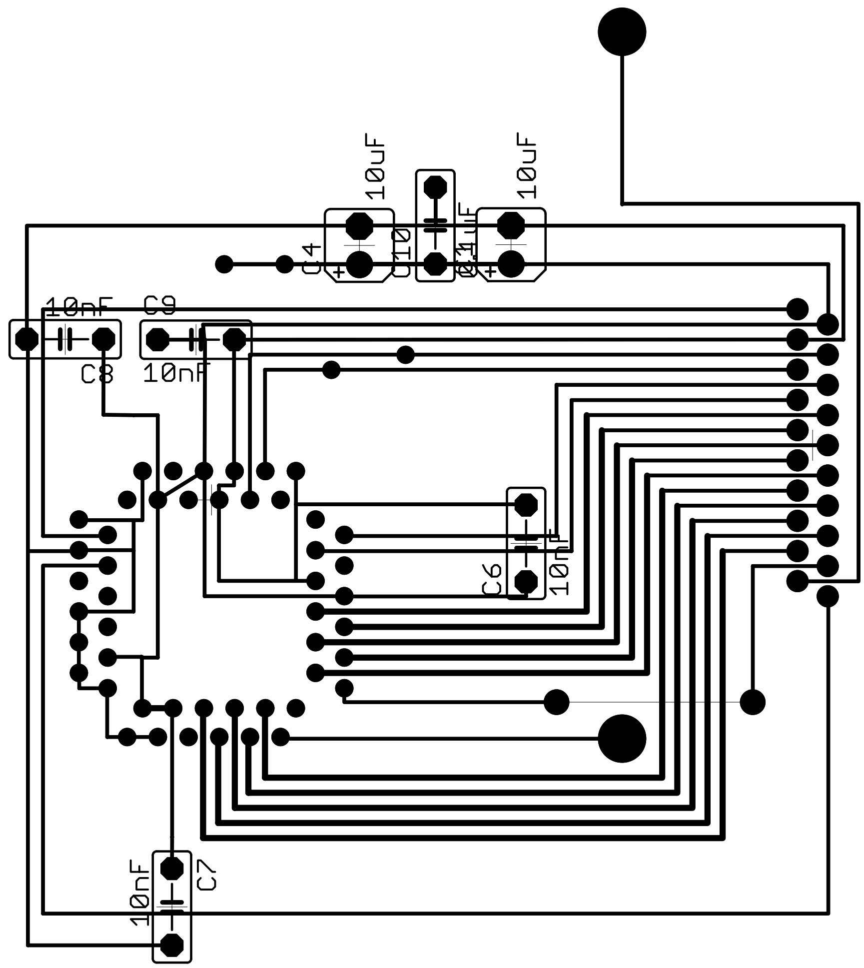

Figure 4.4: Layout of the printed circuit board housing the image sensor and a 20 conductor, 1 mm pitch, vertical ZIF connector along with a resistor and capacitors for signal conditioning.

4.3.1 Timing

The finite rise and decay times of the LCD pixels place significant constraints on the frame refresh rate and lead to variation in the apparent contrast with frame period. A variable delay is implemented after each row is written with real time control to permit user optimization. In order to objectively assess the optimum frame period, a photodiode was used to record light intensity from the centre of the display.

Figure 4.5 illustrates the complex nature of the variation in display intensity.

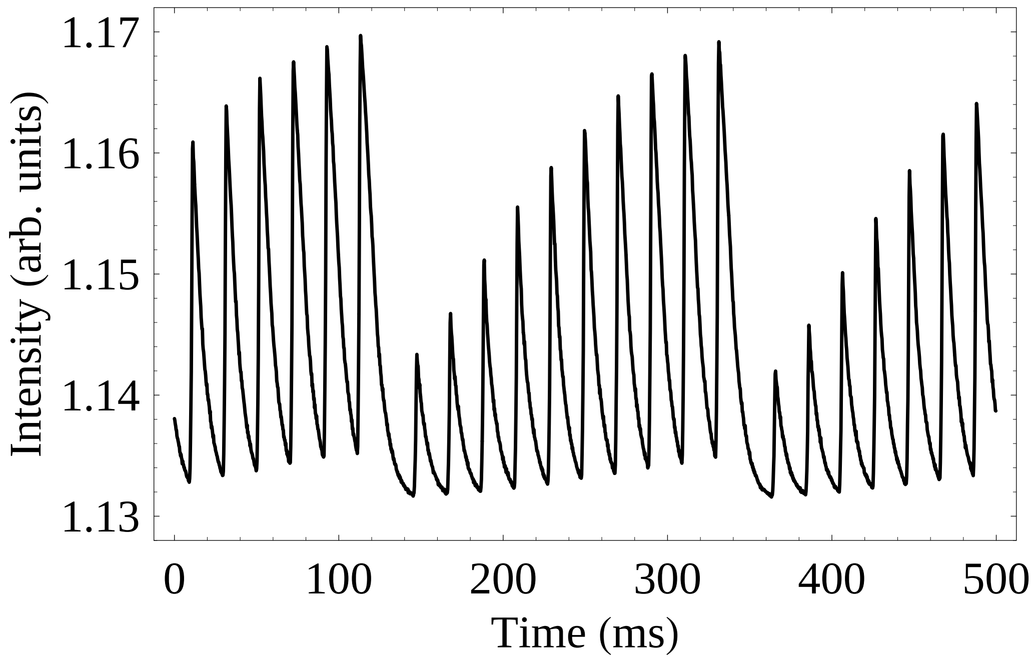

Figure 4.5: Variation in display intensity showing the characteristic rise and decay times of the LCD pixels. The structure of the variation gives some insight into the operation of the program; note the groups of ten identical frames separated by an additional delay as new data is transferred from the *SensorPIC* to the *DisplayPIC*, as described in section 4.4.4.

There is an oscillation at the frequency of the frame refresh rate; each new frame of data is displayed consecutively ten times, followed by an additional delay as new data is obtained.

Display intensity data, recorded for a variety of row–end delays, showed that time–averaged intensity increases with frame period as each pixel is given more time to reach full brightness. At a frame period of approximately 28 ms, the intensity, averaged over a full cycle of ten frames and a data update, reaches a maximum. Beyond this, increasing the delay simply decreases the frame rate, leading to a visible flicker. Figure 4.6 illustrates the effect of adjusting the delay on the time–averaged display intensity; at a frame period of 18.5 ms we observe an anomalously low average intensity due to the effect of beating between the display refresh rate and the acquisition of new data.

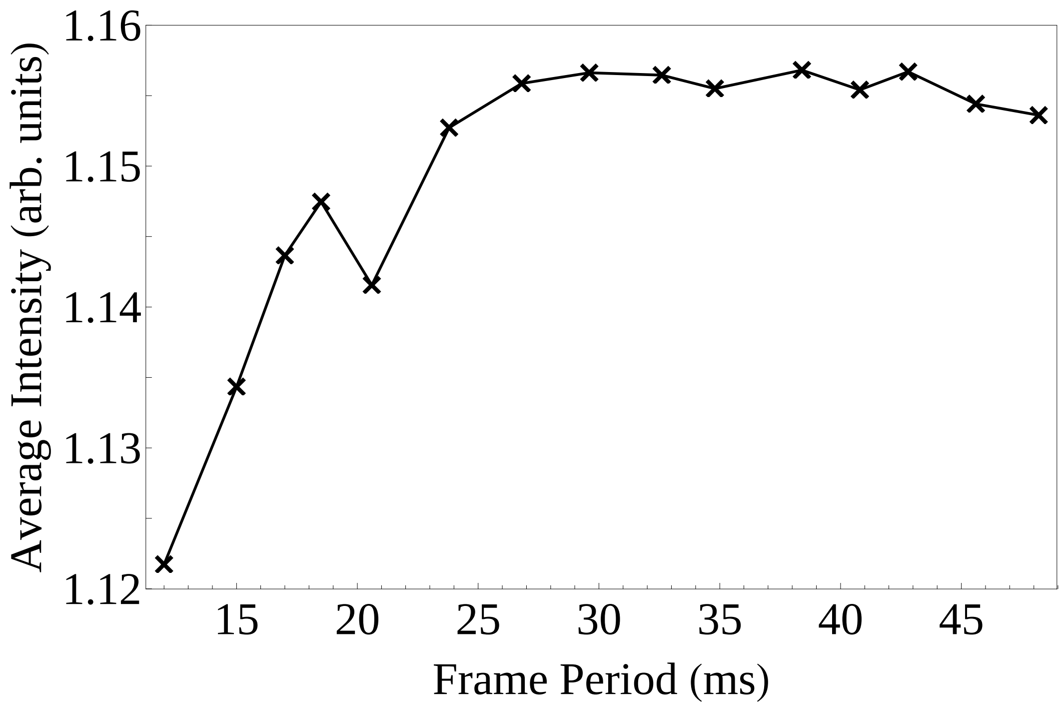

Figure 4.6: Average intensity increases with row–end delay, reaching a maximum at approximately 28 ms. Note the anomalous value at a delay of 20.5 ms due to beating between the frame refresh rate and the frequency of data updates by the *DisplayPIC*.

4.4 The microcontrollers

To achieve the precise control of multiple complex devices at the speeds required, low cost microcontrollers from the PICMicro® family were employed. The final design utilized two different microcontrollers; one used to control the sensor (subsequently referred to as the *SensorPIC*) and the other used to control the LCD (subsequently referred to as the *DisplayPIC*).[57]

SensorPIC

- Model PIC18LF2320 operating on the 3.3 V logic required by the sensor
- Configures sensor prior to system operation
- Provides 2 MHz clock signal used to synchronize output of intensity data
- Reads and stores a full frame of intensity data
- Makes intensity data available to *DisplayPIC* on request

DisplayPIC

- Model PIC18F2320 operating on the 5 V logic required by the LCD
- Requests intensity data from *SensorPIC*
- Reads and stores a full frame of intensity data
- Provides pixel, line and frame synchronization signals to display
- Outputs formatted intensity data to display
- Executes user adjustable delay to optimize display contrast

The F (Flash) and LF (low–voltage Flash) models, so called because they use flash memory to store programs, are identical other than the allowed logic voltage; the F model requires 5 V logic while the LF model can accept anything in the range 2.0–5.5 V with restrictions on clock frequency for lower voltages.

4.4.1 Memory

Three types of memory are available in the microcontrollers: non–volatile flash memory is used to store a program up to a maximum of 4096 single word instructions, volatile static RAM (SRAM) provides rapid access data memory, while non–volatile electronically erasable, programmable read–only memory (EEPROM) may be used to store data between uses.

Table 4.2: Memory available and memory used in the PIC18F2320 and PIC18LF2320 microcontrollers.

Microcontroller memory (bytes)			
Type	Available	Used in *SensorPIC*	Used in *DisplayPIC*
Flash	8192	394	582
SRAM	512	265	269
EEPROM	256	0	0

Flash memory

The user program, created in assembly language and compiled into hexadecimal format, is ultimately stored in binary form in the microcontroller program memory, implemented in Flash. Flash memory is readable, writable and erasable during operation; a read is executed in blocks of a single byte, a write is executed in blocks of 8 bytes, while an erase operation occurs in blocks of 64 bytes and cannot be implemented in user code. This architecture makes it possible, but impractical, to use program memory for storing data.

Note that the programs implemented in the *SensorPIC* and *DisplayPIC* use approximately 5 and 7 % respectively of the available program memory, giving plenty of scope for program extensions. See section 4.4.4 for further discussion of this.

Static RAM

High speed, volatile data memory is implemented as static RAM with 12–bit register addresses used to store special function registers (SFR) and general purpose registers (GPR). SFRs control specific functions of the device; for example, bits 6–4 of the OSCCON register set the frequency of the internal oscillator, used in the *SensorPIC*. GPRs are used for data storage in user applications; examples include the *Time* counters used to implement delays and the *LineCount* variable used to determine which LCD row is currently being addressed.

Data memory may be addressed directly or indirectly. Direct addressing has been used to reset counters to their initial values; in such cases the location of the register must be specified. An SFR called the Bank Select Register can be used to determine the data memory bank in which the register is stored; alternatively, a feature called the Access Bank can be used, providing access to limited sections of the data memory using 8–bit addresses. We have used the Access Bank for all direct addressing operations.

Indirect addressing of data memory does not specify a particular register address, rather it uses a set of SFRs to keep track of, write to and read from an abstract table. The File Select Register for the n^{th} table (FSRn) points to the current register, while writing to or reading from INDFn writes to or reads from the register currently selected by FSRn. The use of POSTINCn, PREINCn, POSTDECn and PREDECn works in the same manner as INDFn with an increment or decrement of FSRn, either before or after the operation. Indirect addressing is used to store the table of 240 8–bit intensity values which together constitute a single frame of data to be displayed on the LCD.

EEPROM

The inclusion of EEPROM allows user data to be stored while the device is unpowered. Currently this is not being exploited, however it is interesting to note that the 256 bytes available provide enough memory to store a full frame of 240 intensity values, allowing for the inclusion of a "frame save" feature. This is discussed further in section 4.4.4.

4.4.2 Clocking

One of the benefits of PIC microcontrollers is the precise temporal control they afford the user. A variety of clock sources can be used giving a known clock cycle period; each single word instruction takes exactly four clock cycles to execute.

SensorPIC: internal RC oscillator

Oscillator selection is achieved using the configuration register CONFIG1H; one of a set of registers stored in the dedicated configuration memory space described in **Flash memory**, section 4.4.1. Bits 3–0 → 1001 selects the internal RC oscillator with pin 6 of port A (RA6, see section 4.4.3) configured to provide a square wave output at a quarter of the internal oscillator frequency. This is the only special function pin exploited in the *SensorPIC* and it is used to provide the clock signal for the image sensor.

The internal RC oscillator has a selectable frequency of $2^n \times$ 125 kHz, where n is an integer between 0 and 6, giving a maximum frequency of 8 MHz, selected using the OSCCON SFR (see section 4.4.1).

DisplayPIC: high speed crystal oscillator with phase–locked loop

Timing is critical when driving an LCD as the finite rise and fall times of the pixels produce a limited window for the frame refresh rate outside of which no image is visible, see section 4.3.1. To provide maximum flexibility in the frame refresh rate, the *DisplayPIC* had to run at the maximum achievable frequency.

Again configuration register CONFIG1H is used to select the oscillator mode: bits 3–0 → 0110 select a high speed crystal oscillator with the phase–locked loop (PLL) function enabled. The oscillator used is a CTS Reeves MP101 parallel crystal which resonates at 10 MHz, while the PLL increases the frequency by a factor of four using an internal voltage controlled oscillator, with a secondary output reduced in frequency by a factor of four and phase–locked to the crystal oscillator output using a phase comparator in a negative feedback loop.[58]

High speed crystal oscillators up to 20 MHz may be used without the PLL, however the maximum frequency obtainable uses a 10 MHz crystal, producing a phase–locked loop output signal at 40 MHz. A stable supply voltage is essential in this clocking mode; a 10 μF electrolytic capacitor between V_{CC} and ground helps to ensure stable oscillation.

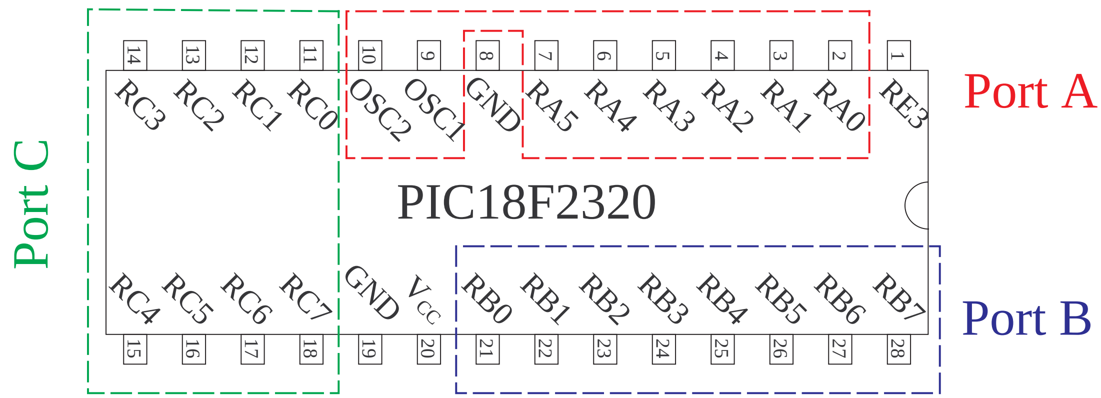

Figure 4.7: Pin configuration for the PIC18F2320; pins RA6 and RA7 of port A also function as OSC1 and OSC2. The crystal oscillator is connected across OSC1 and OSC2 on the *DisplayPIC*, while OSC2 is the output for the 2 MHz sensor clock signal. Although labelled as such in the datasheet, the RE3 port is not operational on this device.

4.4.3 Inputs/outputs

Both microcontrollers used have three principal 8–bit input/output (I/O) ports labelled A, B and C. The eight pins associated with each port default to tri-state logic I/O ports although many of them can be reconfigured to support special functions. As the name implies, tri–state logic can be in one of three states: output high (logic 1, pin is a current source), output low (logic 0, pin is a current sink) or input (logic level controlled by an external device, pin has a high input impedance).

To avoid high current conditions caused by shorts, each port has an associated 8–bit tri–state configuration register labelled TRISX for port X. Each bit within the resister controls the impedance state of the corresponding pin for the associated port; a logic 1 makes the pin an input (high impedance), while a logic 0 makes the pin an output (low impedance).

Used in the default I/O configuration, the pins associated with port A are labelled RA0 $\rightarrow$ RA7, however pins RA7 and RA6 can be configured as OSC1 and OSC2 respectively. When using a high speed crystal oscillator the crystal is connected across OSC1 and OSC2, while the sensor clock output, at $^1/_4$ of the internal RC oscillator frequency, is provided from OSC2.

4.4.4 The program

The program consists of two processes running separately on the two microcontrollers. The *SensorPIC* starts by configuring the image sensor, then reads a frame of intensity data and transfers the data to the *DisplayPIC* using a custom communication protocol. The *DisplayPIC* receives the frame of intensity data, then plots the resulting curve on the display. The program is illustrated in schematic form in figure 4.8.

Configuring the sensor

The PIC18LF2320 microcontroller used to communicate with the sensor has a built–in serial communications module called the Master Synchronous Serial Port (MSSP), with I^2C capability. Serial programming using the MSSP is an extremely simple automated process; unfortunately, hardware limitations necessitated a more complicated, low–level approach.

The two pins used to provide the serial clock (SCLK) and serial data (SDATA) signals are part of digital I/O port C, one of just three ports available. The master clock for the sensor is provided from a pin which would otherwise form part of port A. As we need one full port to receive data from the image sensor and another to output the reformatted data with the correct timing, we can only use special function pins from a single port, thus a subroutine was constructed within the assembly code (see appendix A) to allow serial communication using two general I/O pins.

Reading data from the sensor

Reading intensity data from the sensor commences when the 8–bit value representing the intensity detected by the first pixel in a row becomes available on the *SensorPIC* input data bus; this is synchronized with the rising edge of the LINE_VALID signal

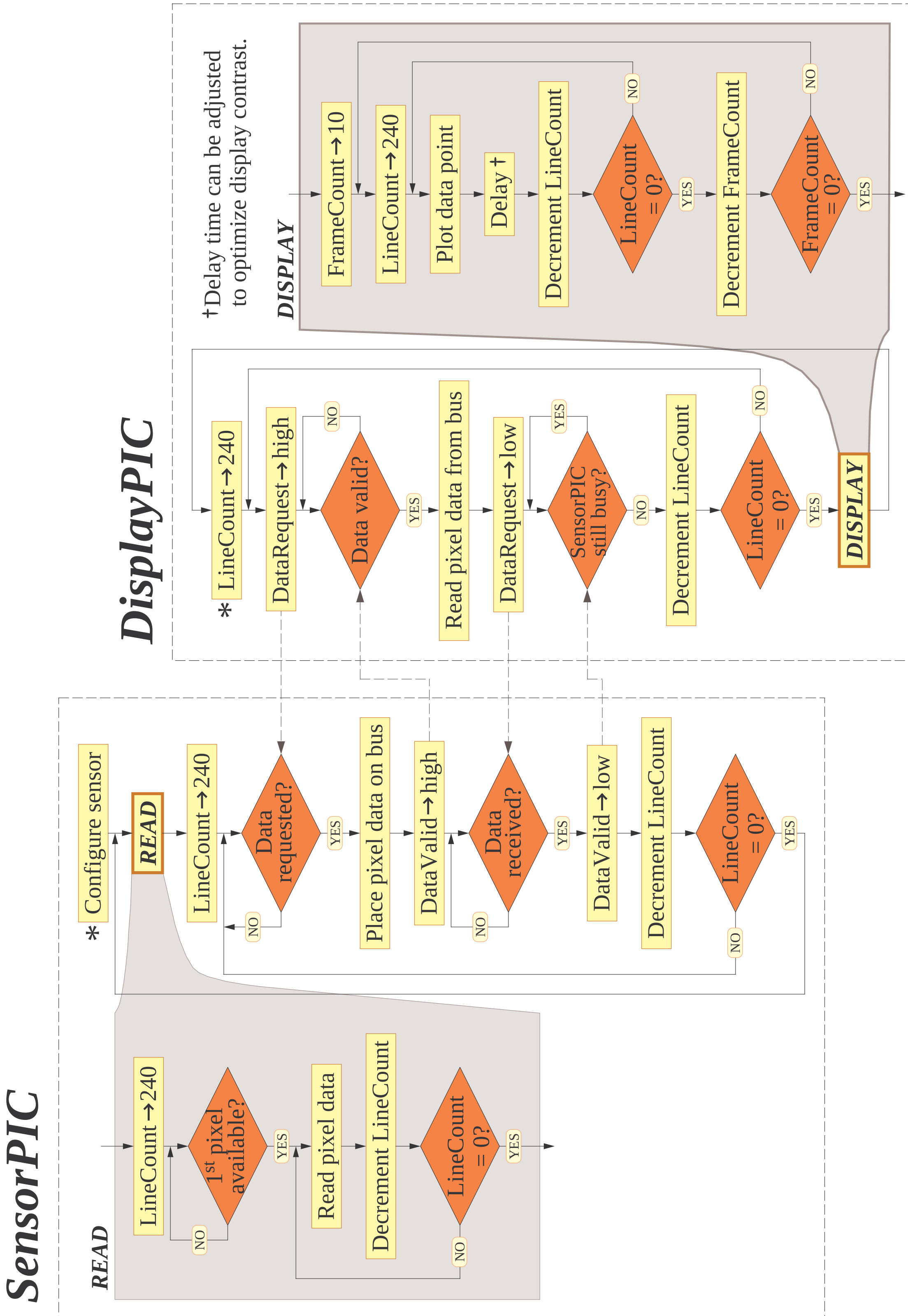

Figure 4.8: A flow chart illustrating the operation of and communication between the *SensorPIC* and *DisplayPIC* programs. The two processes begin with the operations marked with an asterisk.

from the sensor. Following this, the full frame of 240 values is read using a program loop composed of five instruction cycles; as each instruction cycle corresponds to a single cycle of the clock signal sent to the sensor, every fifth pixel intensity value is recorded. Thus the actual sensing width covers $240 \times 5 = 1200$ out of a total 1280 pixels across the active width of the sensor.

The full frame of data is stored using the indirect addressing approach described in section 4.4.1; each value is written to the POSTINC0 register, which subsequently transfers it into the register indicated by FSR0, then increments the value of FSR0. The *LineCount* variable, initially given a value of 240, is decremented after each value is read and the sequence is terminated once it reaches zero.

Data transfer

Due to the different requirements of their respective peripherals, the two microcontrollers run at different clock speeds; a custom protocol was implemented to facilitate communication and ensure that no data is lost. The system uses two control lines and an 8–bit data bus: the data request line is set high by the *DisplayPIC* to indicate that it is ready to receive a byte of intensity data, the data valid line is subsequently set high by the *SensorPIC* to indicate that a valid byte of data is available on the data bus. The *DisplayPIC* sets the data request line low to indicate that the data has been received and stored, and, finally, the *SensorPIC* sets the data valid line low to ensure that the same value is not retransmitted on the next data request.

Writing to the display

Upon receipt of each data valid signal, the *DisplayPIC* transfers a single byte of intensity data from the data bus into a table using the same indirect addressing system described in section 4.4.1. Once a full frame of 240 values has been stored, the display algorithm can begin.

The display is initialized by switching on the 5 V input to the voltage regulator supplying the 1.7 V power source for the LCD Drive and setting the $\overline{\text{DISPOFF}}$ signal high. A set of coordination signals are used to synchronize the writing operation: the data latch signal, LP, is used to indicate the start of a new row and the first line marker, FLM, is used to indicate the start of a new frame. The display clock signal, CP, is provided only as needed from a general I/O pin, and consequently has no defined duty cycle.

For convenience, while dealing with the coordination signals, the first line is written entirely as zeros, corresponding to bright pixels. Each following line includes a marker consisting of dark pixels (logic 0), the top of which indicates the intensity value, while the length is chosen such that it extends to the top of the lowest adjacent marker; if the two adjacent markers are both above, then just a single dark pixel is written. In order to facilitate this, each intensity value must be compared with the preceding and following values to assess their relative positions.

Because data is transferred to the display using a 4–bit bus, each display clock cycle corresponds to a four pixel block being written with the binary values available on the bus. Obtaining a marker of the correct length potentially requires a partially filled block at both ends. Once the intensity values corresponding to the maximum (MAX) and minimum (MIN) extent of the marker have been obtained, the partial block size is obtained mathematically as MAX mod 4 and MIN mod 4.

Once the appropriate length and position of the marker have been established, the program calls one of two possible delay subroutines used to adjust the display contrast as discussed in section 4.3.1. The logic level of a specified pin is tested to determine whether the user wishes to increase the delay time or use the current value; the increase delay subroutine uses a 9–bit cyclic counter, utilizing two 8–bit registers, to slow the rate of delay increase so that the reaction time of the operator does not significantly limit the temporal resolution in setting the delay time.

Program extensions

The processes running on the microcontrollers only use a fraction of the available program memory, as is clear from table 4.2. In spite of limitations due to the small number of available I/O pins, and timing constraints, the flexible nature of the microcontrollers affords the user the option of a multitude of modifications.

a) Maximum intensity persist

The *DisplayPIC* was reprogrammed to store the maximum value detected by each pixel, and in a later modification stored two tables of intensity data, representing both the current and the maximum values, with a switch to select which set of data is displayed. The original purpose was to assess the uniformity of the pixels across the sensor as described in section 4.2.2.

A potentially major application of this modification is to display the mode structure of pulsed lasers. The pixel integration time (see section 4.2.1) could be set to sum over a number of pulses, each of which produces a Fabry–Pérot fringe pattern dependent on the mode structure. A curve representing the maximum intensity detected by each pixel should provide a stable image, clearly illustrating the mode structure of the laser.

b) EEPROM frame save

To date in this project, no use has been made of the EEPROM data memory mentioned in section 4.4.1. As the 240 bytes of intensity data comprising a full frame is less than the 256 bytes of available EEPROM, the device has the capability to store a set of data, representing the mode structure of a particular laser, for later viewing. More useful would be a method to output the data in digital form, such that it can be transferred onto a more powerful computer. At present, there is no convenient way to accomplish this.

4.4.5 The microcontroller circuit

A second printed circuit board was produced to house the microcontrollers receiving inputs from the sensor board and outputting signals to the LCD. Two 28–pin dual in–line saddles permit easy access to the microcontrollers for reprogramming. A vertical ZIF connector is provided for the 20 conductor ribbon cable carrying signals to and from the image sensor. It is important that the orientation of the ZIF socket mirrors that of the one on the sensor board, as it connects to the same cable from the opposite end.

A DC power supply (described in section 5.2) provides 5 V referenced to earth ground. The 3.3 V logic supply for the image sensor and *SensorPIC*, and the 1.7 V LCD drive voltage, are provided by voltage regulators (LM317T) on the board. The *DisplayPIC* controls the 5 V supply to the 1.7 V regulator to ensure that the system adheres to the correct power–up timing schedule.

The eight signal lines from the *DisplayPIC* to the display include 3.4 kΩ pull–down resistors to ensure that the signal lines never float.

4.5 System characterization

The completed system was tested using an external cavity diode laser (ECDL) at 670 nm,[48] and a 0.5 $\pm$ 0.05 mm solid étalon (OFR IE–0.5–VIR–R–S) with a nominal reflectivity for each face of 90 % within the wavelength range 550–780 nm. Reflection from a pair of uncoated wedges reduced the beam power to 3.3 μW, which was used to produce an interference pattern incident on the image sensor.

The mode structure of the ECDL beam varies with changes in temperature, injection current and cavity length, and it operates on a single mode only for narrow parameter ranges. Figure 4.11 is a digital photograph of the display illustrating the single mode operation at an injection current of 55.5 mA, showing the 2$^{\text{nd}}$ order fringe

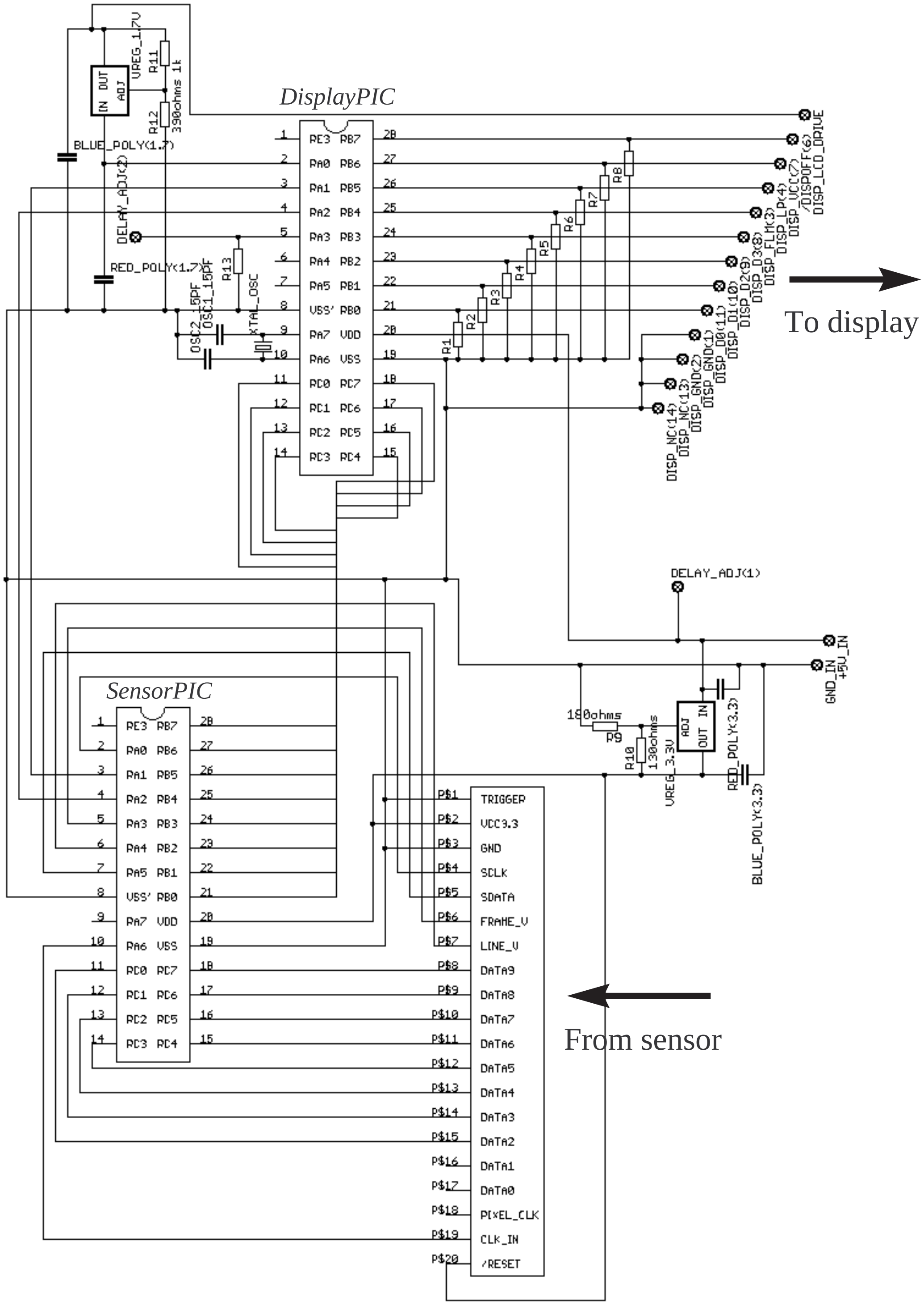

Figure 4.9: Schematic diagram of the main circuit, including the two microcontrollers, a ZIF socket for the ribbon cable from the sensor board, voltage regulators providing the 3.3 V logic supply and the 1.7 V LCD drive voltage, pull–down resistors for the display inputs and capacitors for signal conditioning.

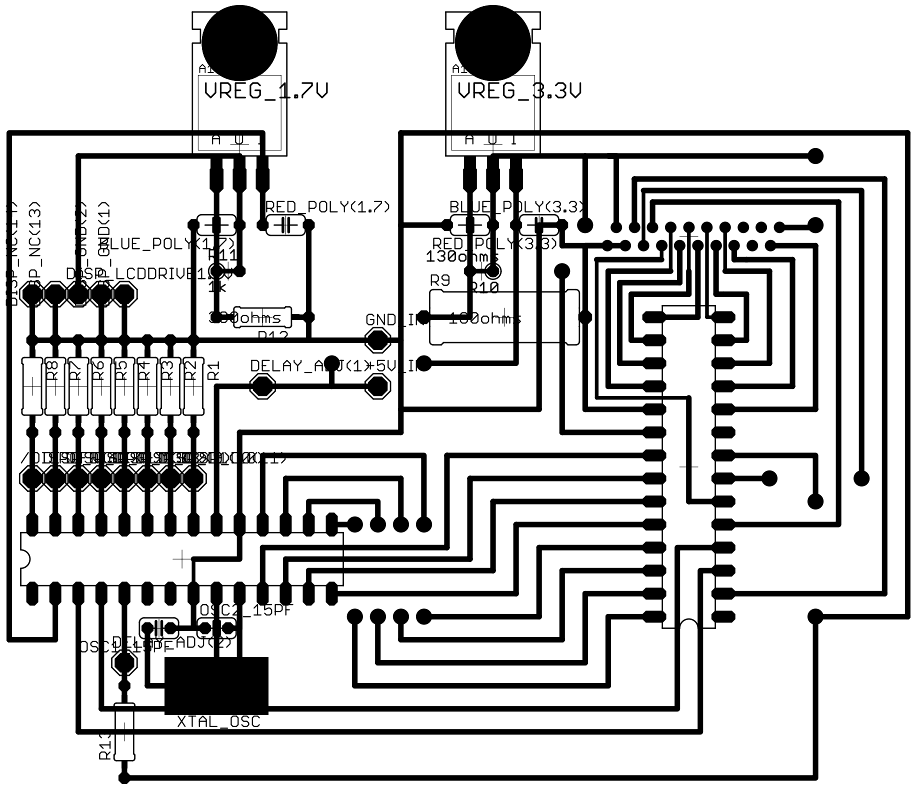

Figure 4.10: Layout for the printed circuit board housing the two microcontrollers, voltage regulators providing the 3.3 V logic supply and the 1.7 V LCD drive voltage, pull–down resistors for the display inputs and capacitors for signal conditioning.

($p = 2$, equation 4.1) on the right, with decreasing spacing and intensity for higher order fringes; the finesse is measured to be 23 ± 3, indicating a reflectivity of 93 %. The injection current was increased to 56.6 mA, resulting in multimode operation as illustrated in figure 4.12. The peak corresponding to the additional mode appears to the left of the original peak, the pattern is translated laterally due to movement of the final lens.

The mode separation is measured to be 47 GHz, close to the 40 GHz separation expected for typical diode lasers with a cavity length of 250 μm and in good agreement with a previous measurement using a calibrated wavemeter.[59]

For comparison with a commercial device, the same laser beam was analyzed using a Coherent model 240 optical spectrum analyzer, displaying the output on an oscilloscope (Agilent 54622A). The Coherent system is a typical piezoelectically driven

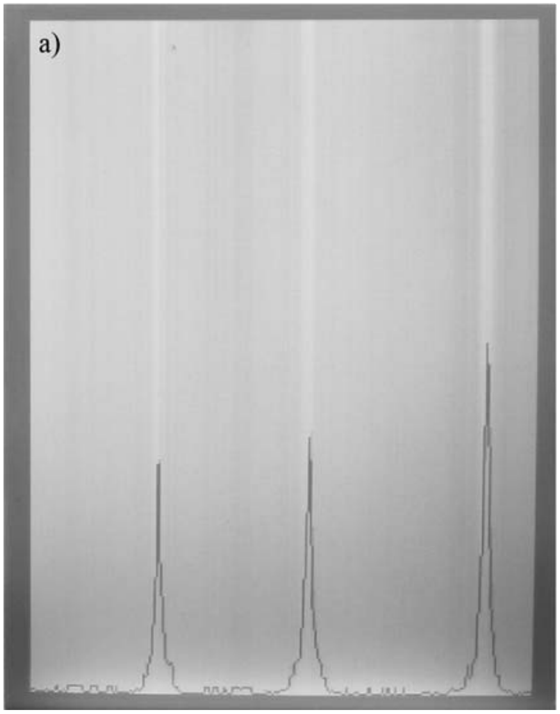

Figure 4.11: Displaying single mode operation of an external cavity diode laser at an injection current of 55.5 mA.

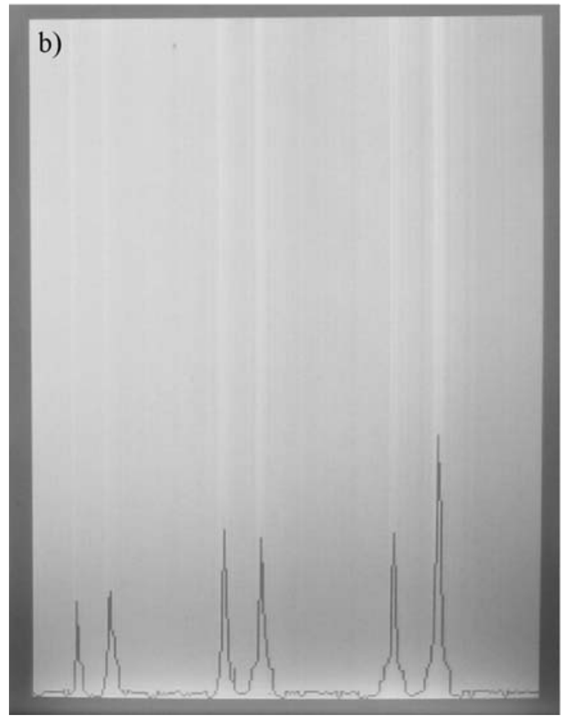

Figure 4.12: A small reduction in injection current leads to the appearance of a second mode to the left.

Fabry–Pérot based device which produces a temporally–varying interference pattern detected by a photodiode. With the 3.3 μW beam no signal was visible above the noise floor; the spectrum started to emerge from the noise at a beam power of 8 μW.

An experiment was performed to assess the linearity and sensitivity of the system. The image sensor recorded the far–field diffraction pattern from a 300 μm aperture illuminated by the ECDL. Nine traces were taken with the power adjusted using a linear polarizer and the laser beam power measured directly using a Coherent LaserMate–Q power meter. Each trace was fitted to an Airy function, from which the integrated intensity was compared with the measured power to calculate the peak intensity. Plotting actual intensity against the measured height of a peak in pixels produced the calibration curve shown in figure 4.13.

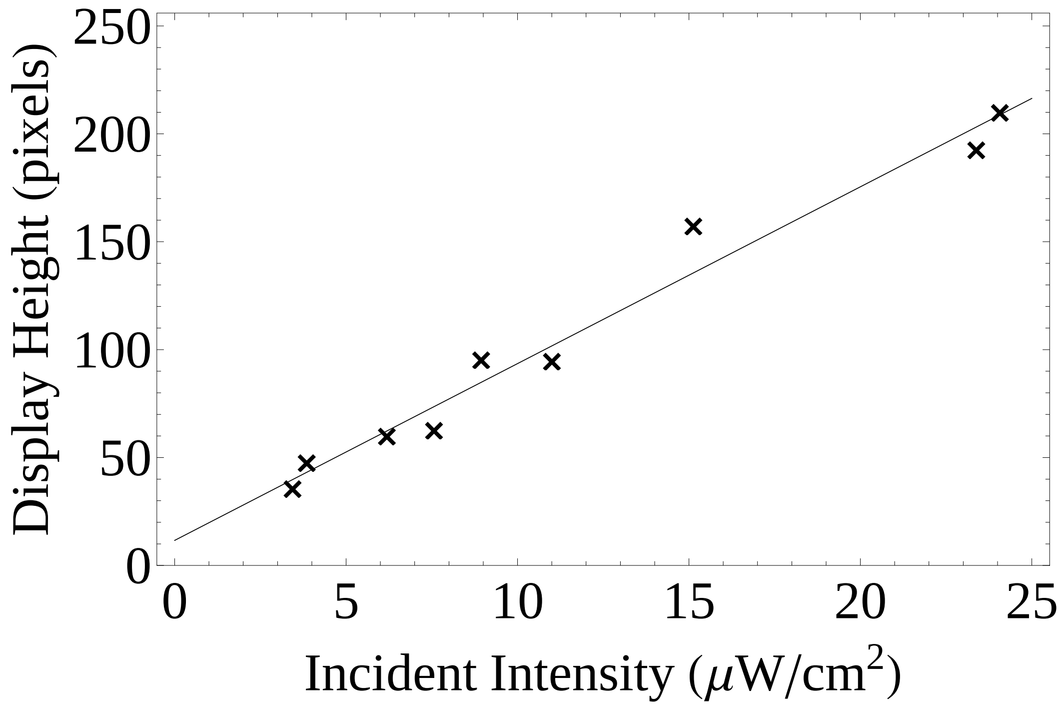

Figure 4.13: Calibration curve illustrating the sensitivity and linearity of the image sensor.

4.6 Future developments

The discussion of program extensions in section 4.4.4 illustrates the simplicity of software modification. There are a number of specific hardware modifications that could be made to improve the system.

The *SensorPIC* could trivially be made to read the eight least significant bits from the sensor, immediately increasing the sensitivity by a factor of four; this approach could be useful for experiments using low power lasers such as those based on nonlinear frequency conversion, however it has not yet been implemented as it would entail beam powers so low as to be barely visible, making alignment extremely challenging.

To increase the sensitivity without reducing the intensity at which the sensor saturates, the entire 10–bit values output by the sensor could be used. This would require different components than those used here: microcontrollers with 10–bit wide ports would be needed to efficiently transfer the intensity data, while a higher LCD resolution would be needed to display the full dynamic range of 1024.

Alignment of the optics could be made quicker and more convenient by using an optical fibre to send the beam under test into the OSA.

Chapter 5

Power Supplies

In an experimental physics lab, numerous devices must be provided with a stable, reliable power supply. The power supplied by a DC source is given by the product of voltage and current $P = IV$; the supplies fall into two broad categories: *current supplies* provide a constant current by varying the voltage as required, while *voltage supplies* provide a constant voltage by similarly varying the current.

5.1 Current supply

A high power current supply is required to power the heating element for the lithium oven to be used in the beam experiment discussed in chapter 1.

5.1.1 Initial design

The chosen design uses the emitter–follower configuration (also known as a common–emitter). The circuit diagram illustrating the concept is shown in figure 5.1.[60]

In order to maintain a constant current for a varying load an emitter–follower makes use of *return–line current sensing.* The voltage drop across a low–value, high–power sensing resistor, on the return line to the negative electrode of a constant voltage supply, is compared to a variable reference voltage providing the set–point.

During the construction of the device, many changes and additions were made,

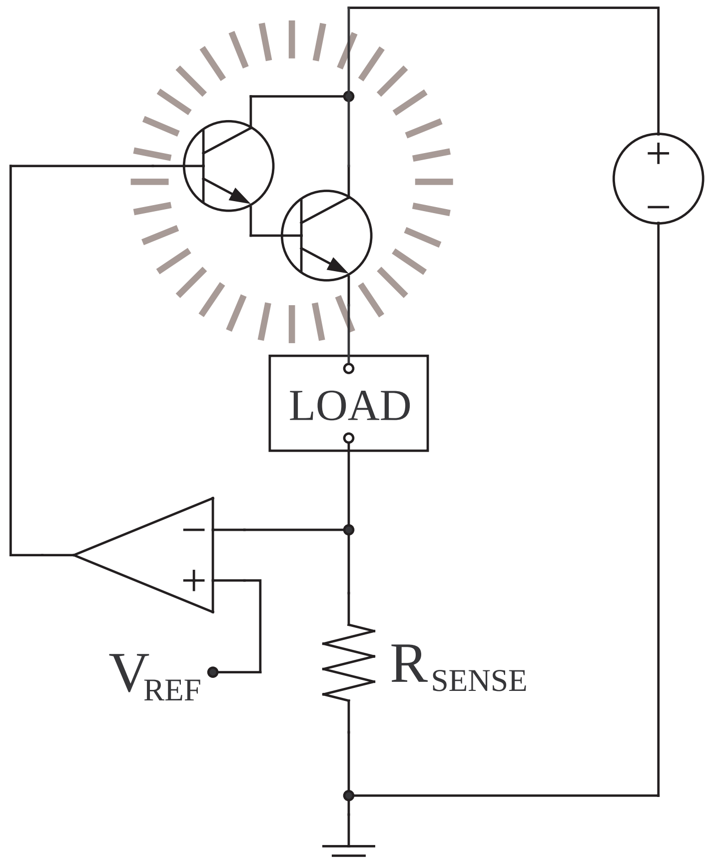

Figure 5.1: Schematic of an emitter–follower current supply; the active device is a Darlington transistor pair mounted on a heat sink. The load is floated above the sensing resistor R_{SENSE}, while an op–amp sets the current such that the voltage drop across the sensing resistor remains equal to the reference voltage V_{REF} at all times.

some for convenience, customization and safety, others to deal with fundamental problems in the design. There were three major design issues encountered:

1. **Power dissipated in the sensing resistor**

   All main–line current must flow through the sensing resistor to provide a measurement for the negative feedback loop used to set the current. At high currents the sensing resistor will dissipate a significant amount of power ($P = I^2R$, for a 4 A current flowing through a 1 Ω resistor, this amounts to 16 W of power). Two different approaches were used to deal with this.

- High power resistors with good heat–sinking

- Two different values of R_{SENSE} selectable for different current levels (1 Ω for $0 \leq I < 2$, 0.5 Ω for $2 \leq I \leq 4$)

As the set–point voltage V_{REF} is compared to the voltage across R_{SENSE}, the different resistor values require different set–point voltage ranges to ensure the mainline current remains within an acceptable range.

2. **Power dissipated in the transistor**

In terms of impedance, a transistor works much like a variable resistor with the resistance determined by the base current. For small base currents the collector–emitter impedance is high and the total load seen by the voltage supply is dominated by the transistor, leading to significant power dissipation in the transistor and ultimately to overheating.

The original design illustrated in figure 5.1 used a heat–sunk Darlington pair in place of a single NPN transistor in order to dissipate excess heat, however these measures proved inadequate given the power requirements of the unit. The final design, shown in figure 5.3, took this concept further.

- Two Darlington pair transistor combinations used in parallel, cuts the power dissipated in each by half
- An individual heat–sink for each Darlington pair, mounted externally to promote convective heat dissipation

3. **Maintaining an adequate base–emitter voltage**

A Darlington pair requires a 1.2 V base–emitter voltage before any collector–emitter current will flow. At high current levels the voltage drop across the load is such that the op-amp providing the base current cannot provide a sufficiently high voltage even if it can swing to the rails.

This problem could have been solved simply by furnishing the op-amp with a higher voltage supply. However, the standard lab supplies that we use (see section 5.2) provide a maximum of ±15 V and for the sake of convenience it seemed worthwhile pursuing a solution which did not require a supply voltage outside this range. The 48 V supply powering the device is not used to power the control electronics as this could lead to instability, due to fluctuations in the power supply being amplified by identical fluctuations in the control electronics.

The final design shown in figure 5.3 illustrates the simple solution employed. The load is floated above the transistor which means that the output of the op-amp need never rise above 1.2 V. The front panel of the high power current supply is illustrated in figure 5.2.

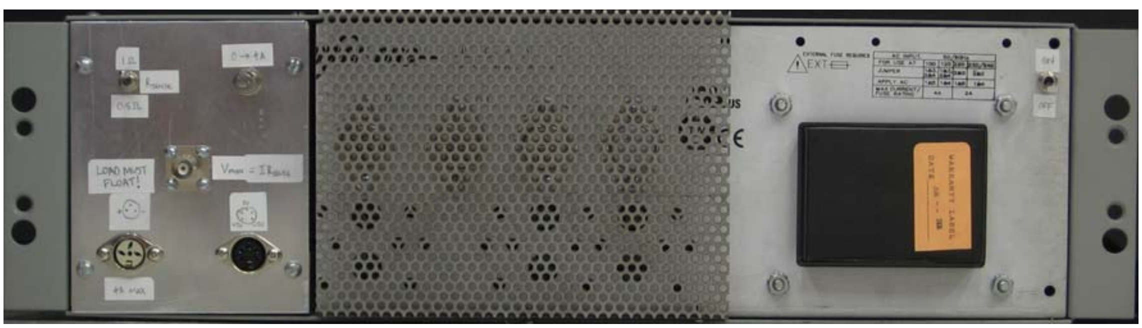

Figure 5.2: The high power, current source power supply, with a safety guard around the power transistors which have cases at high voltage.

5.1.2 A low power current supply

A simple, reliable, low power current supply is used to provide the tuning current to the RF attenuator described in chapter 3. A voltage divider is used to tune the gate–source voltage applied across a n–channel MOSFET. The layout is illustrated in figure 3.6, while the current linearity is demonstrated by the trace in figure 3.12.

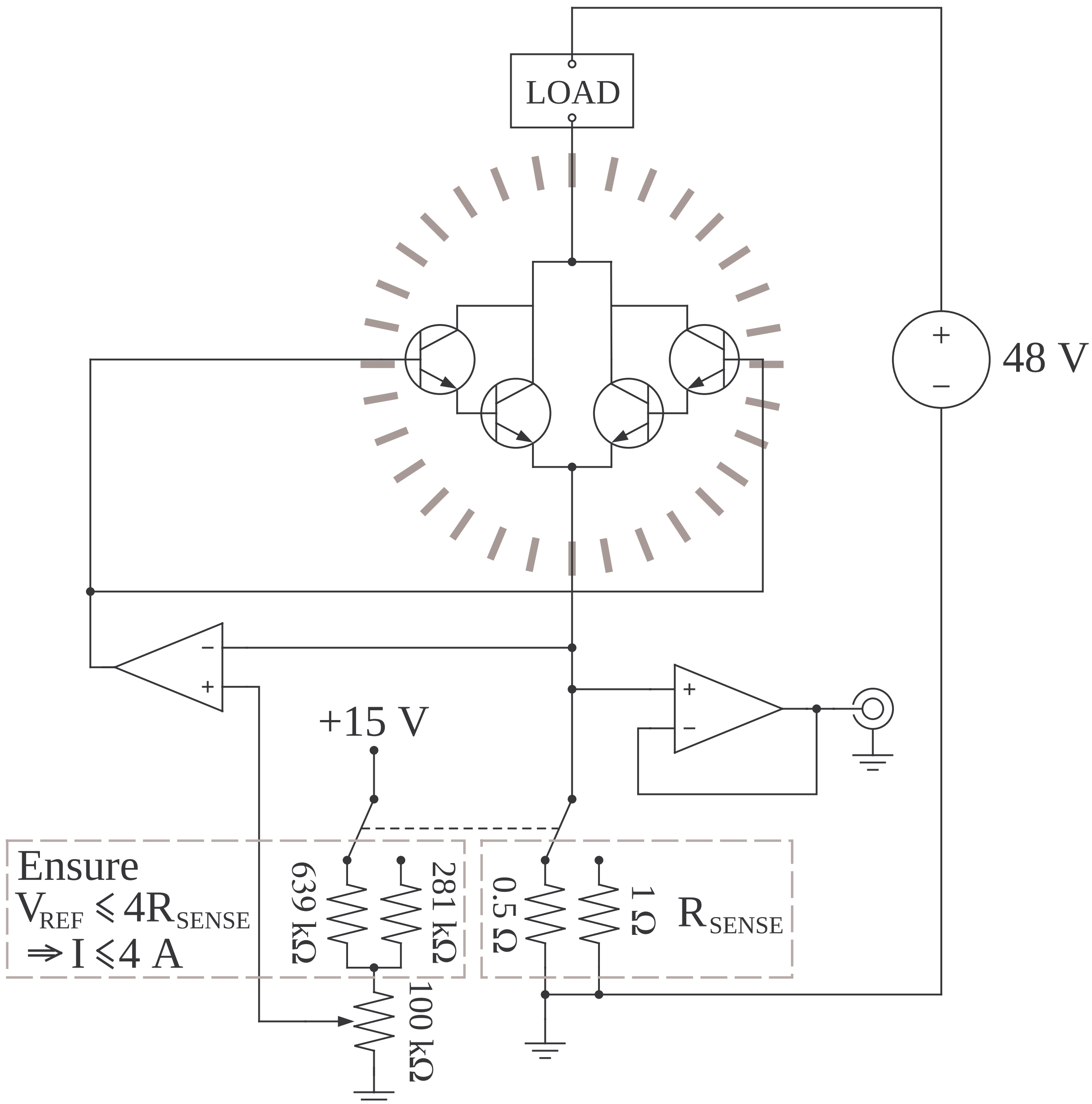

Figure 5.3: The final design; the device can provide more than 40 W to the heating element for a lithium oven, ample power to vaporize either stable isotope of lithium.

5.2 Voltage supply

Figure 5.4: An image of the voltage source power supply.

A search was undertaken to ascertain the best candidate for a standard DC voltage supply to use in the laboratory. A comparison was made of several commercial units available and the component level alternatives.

The device purchased was a Power–One HAD–15–0.4A component level voltage source consisting of a transformer and full–wave bridge rectifier, along with voltage regulators and capacitors to produce a stable ±15 V source. Construction involved mounting the device in a case with voltage regulators to provide additional outputs at ±12 V and +5 V. Figure 5.4 shows the front panel of the finished device.

Chapter 6

The Adiabatic Theorem of Quantum Mechanics: Beyond the Landau–Zener Approximation

A frequently occurring problem in experimental atomic and molecular physics involves the observation and control of a quantum mechanical system, including a perturbation parameter, q, which changes with time. We wish to predict the final state of the system for a given change in q.

The perturbation parameter can represent the internuclear distance during an atomic collision, or the amplitude of an applied electric or magnetic field. After a modification of q and a corresponding change in the system Hamiltonian, the final state depends critically on the profile of the change in $q(t)$ and the time τ during which the modification takes place.[61][62]

A highly relevant example of a system undergoing such a transition is a lithium–fluoride molecule (LiF), which can exist as a predominantly covalently bound or predominantly ionically bound molecule, Li^+–F^-. Figure 6.1 illustrates how these energy states depend on the internuclear distance R; if the internuclear distance of an ionically bound LiF molecule on curve $X^1\Sigma^+$ increases sufficiently slowly, the nature of the bond will change such that the molecule dissociates, forming free lithium and fluorine atoms. If the change in R occurs rapidly there is no time for reconfiguration of the system; the molecule will remain ionic in nature, cross over to the curve labeled $B^1\Sigma^+$ and dissociate to form free Li^+ and F^- ions.

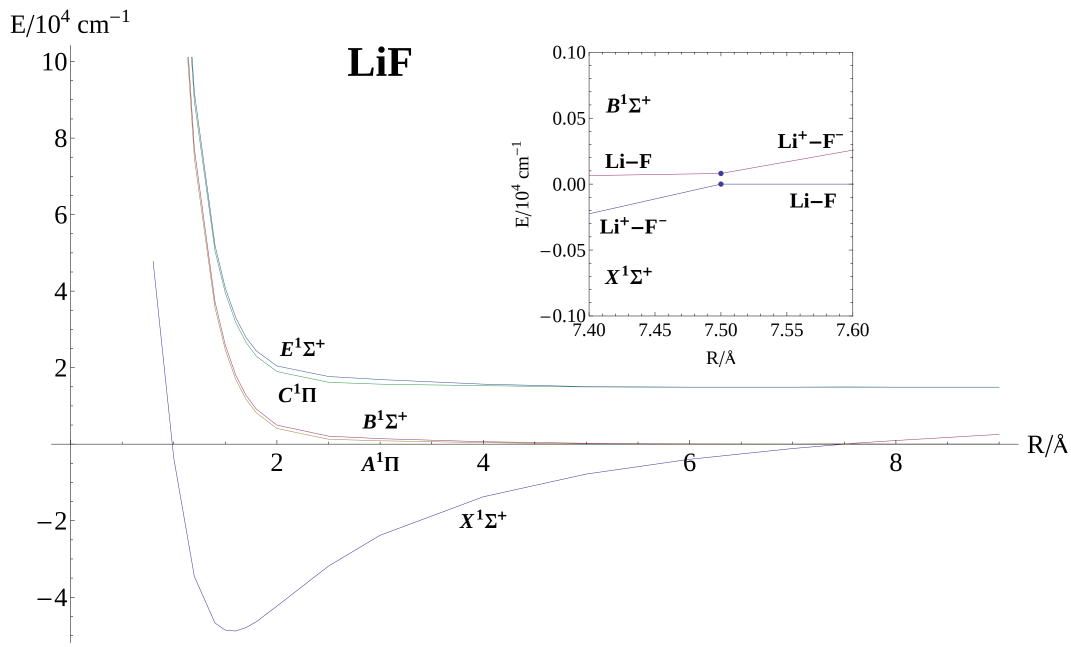

Figure 6.1: An avoided crossing in lithium–fluoride potential energy curves. If the internuclear distance varies adiabatically, the molecule remains on a single curve. Curves obtained using published data.[63]

States that retain their configuration through a crossing are called diabatic states; those that adapt their configuration as the conditions change are called adiabatic states. In order to elucidate this distinction, we will examine the behaviour of a simple model system under the influence of an applied electric field.

6.1 The model system

We will initially examine a hydrogen–like (i.e. Rydberg) atom in an electric field $\mathbf{F}$, with a Hamiltonian given by

$$\hat{H} = \hat{H}_0 + \hat{H}_I, \tag{6.1}$$

where $\hat{H}_0$ is the diabatic Hamiltonian, including the unperturbed kinetic and potential energy and the Stark shift due to the applied field, and $\hat{H}_I$ is the interaction Hamiltonian, which adds an additional short range $1/r^2$ potential due to polarization of the core. The complete Hamiltonian for the system is given by equation 6.2,

$$\hat{H} = -\frac{\hbar^2}{2m}\nabla^2 - \frac{e^2}{4\pi\epsilon_0 r} - \mathbf{d}\cdot\mathbf{F} - \frac{A}{r^2}. \tag{6.2}$$

6.1.1 Diabatic states

For simplicity we will include just two states in the basis $|1\rangle$, $|2\rangle$, with energies $E_1(\mathbf{F})$ and $E_2(\mathbf{F})$, separated at $\mathbf{F} = 0$ by $\hbar\omega_0$. If we take the electric field to be oriented in the positive z–direction, we have a Hamiltonian matrix in the diabatic basis given by,

$$\underline{\underline{H}}(F) = \begin{pmatrix} ea_0F(t) - \frac{1}{2}\hbar\omega_0 & a \\ a^* & \frac{1}{2}\hbar\omega_0 - ea_0F(t) \end{pmatrix}, \tag{6.3}$$

where we have taken the zero point of energy to lie at the halfway point between the two states and assumed that the magnitude of the Stark shift matrix element is the same for the two states. It is clear that at a particular value of the applied field, the two states are degenerate and we have a crossing.

We wish to solve the amplitude equations for the system in the Schrödinger picture, in which the state vectors exhibit spatial dependence but no time dependence (i.e. the phase is arbitrary, but not varying with time),

$$|\psi\rangle = c_1(t)|1\rangle + c_2(t)|2\rangle. \tag{6.4}$$

The time dependence of the state vector amplitudes is given by the time–dependent Schrödinger equation.

$$\underline{\dot{c}} = \frac{1}{i\hbar}\underline{\underline{H}}\,\underline{c}. \tag{6.5}$$

Note that states $|1\rangle$ and $|2\rangle$ are *not* eigenvectors of the Hamiltonian.

Examining equation 6.3 we can deduce the behaviour of the system under a changing field. For a system in state $|2\rangle$, the expectation value of the energy is given by $E_2(t) = \hbar\omega_0/2 - ea_0F(t)$, thus the energy *decreases* linearly with electric field. The expectation value of the energy for a system in state $|1\rangle$ is given by $E_1(t) = ea_0F(t) - \hbar\omega_0/2$, and thus *increases* linearly with electric field. At time $t_\times$, the two energies are equal, with an electric field strength given by equation 6.6.

$$F(t_\times) = \frac{\hbar\omega}{2ea_0}. \tag{6.6}$$

6.1.2 Adiabatic states

We now choose to describe the system in a new basis, using as our state vectors the eigenvectors of the Hamiltonian operator, which we denote $|\phi_1(t)\rangle$ and $|\phi_2(t)\rangle$ with energies given by the eigenvalues $\varepsilon_1(t)$ and $\varepsilon_2(t)$. The system wavefunction given in the diabatic basis by equation 6.4, can also be given in the adiabatic basis as in equation 6.7,

$$|\psi\rangle = c_1^A(t)|\phi_1(t)\rangle + c_2^A(t)|\phi_2(t)\rangle. \tag{6.7}$$

The inclusion of the perturbative interaction Hamiltonian couples the levels, breaking the degeneracy and ensuring that the eigenvalues of the Hamiltonian remain distinct,

$$\varepsilon_1(t) \neq \varepsilon_2(t), \qquad \forall\ t.$$

At time $t_\times$ (see equation 6.6) the adiabatic energies have the lowest energy separation $\varepsilon_2(t_\times) - \varepsilon_1(t_\times) = 2|a|$. Note that a does not vary with time. In the general case, the coupling is a function of the perturbation variable and, therefore, does depend on time. The energy eigenvalues, $\varepsilon_1(F)$ and $\varepsilon_2(F)$, are hyperbolae that each approach $E_1(F)$ and $E_2(F)$ asymptotically.

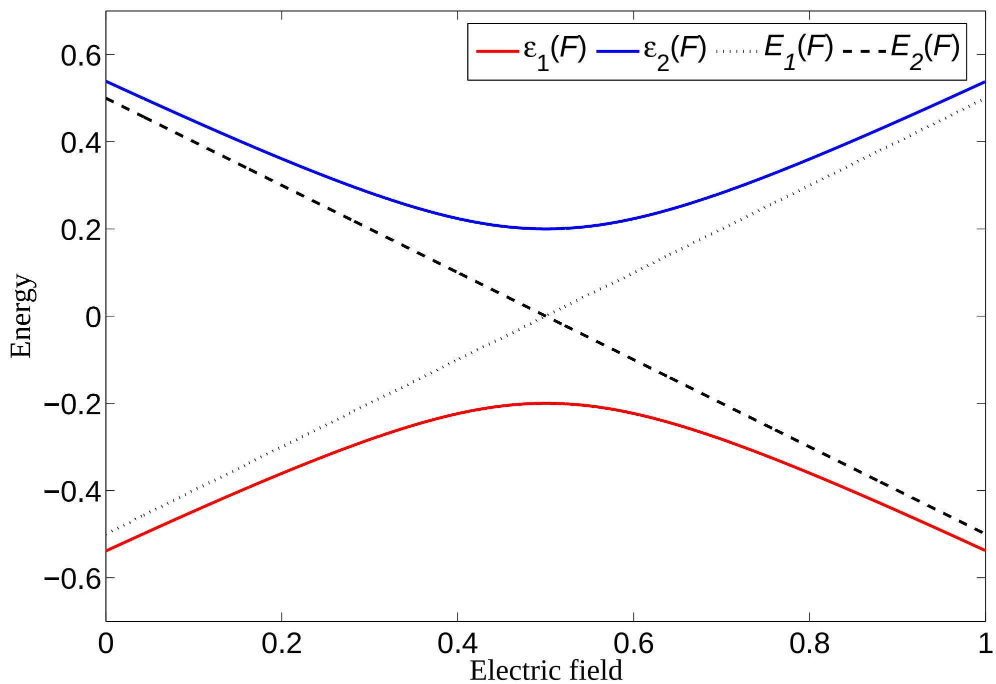

Figure 6.2: Level energies of the diabatic ($E_1(F)$, $E_2(F)$) and adiabatic ($\varepsilon_1(F)$, $\varepsilon_2(F)$) states. Finite coupling between the states leads to the avoided crossing for a system following an adiabatic path.

For a time–independent system, the energy eigenvalues are obtained by diagonalizing the Hamiltonian with a time–*independent* unitary transformation. If the system evolves sufficiently slowly (adiabatic evolution) then the energy eigenvalues calculated for the time–independent solution remain valid. The unitary transformation matrix is constructed from the eigenvectors $|\phi_1\rangle$, $|\phi_2\rangle$.

$$|\phi_1\rangle = \begin{pmatrix} \phi_1^{(1)} \\ \phi_1^{(2)} \end{pmatrix} \qquad |\phi_2\rangle = \begin{pmatrix} \phi_2^{(1)} \\ \phi_2^{(2)} \end{pmatrix}, \tag{6.8}$$

giving a transformation matrix $\underline{\underline{U}}$,

$$\underline{\underline{U}} = \begin{pmatrix} \phi_1^{(1)} & \phi_2^{(1)} \\ \phi_1^{(2)} & \phi_2^{(2)} \end{pmatrix}, \tag{6.9}$$

which can be used to obtain the diagonalized Hamiltonian $\underline{\underline{H}}_D$ through the unitary transformation,

$$\underline{\underline{H}}_D = \underline{\underline{U}}^{-1}\underline{\underline{H}}\,\underline{\underline{U}} = \begin{pmatrix} -\varepsilon & 0 \\ 0 & +\varepsilon \end{pmatrix}, \tag{6.10}$$

where the diagonal elements are the eigenvalues of the Hamiltonian matrix in equation 6.3, given by

$$\pm\varepsilon = \pm\sqrt{\left(ea_0F(t) - \frac{1}{2}\hbar\omega_0\right)^2 + a^2}. \tag{6.11}$$

For a system which changes with time the adiabatic eigenvectors can be obtained from the diabatic state vectors, using the same transformation matrix,

$$\begin{pmatrix} |\phi_1(t)\rangle \\ |\phi_2(t)\rangle \end{pmatrix} = \underline{\underline{U}}^{-1}(t) \begin{pmatrix} |1\rangle \\ |2\rangle \end{pmatrix}. \tag{6.12}$$

The full time–dependence of the state vector in the adiabatic basis can be obtained from the transformed Hamiltonian given in equation 6.13.[64] The full derivation is given in appendix B.

$$\underline{\underline{H}}_A = \underline{\underline{U}}^{-1}\underline{\underline{H}}\,\underline{\underline{U}} - i\hbar\underline{\underline{U}}^{-1}\frac{d}{dt}\underline{\underline{U}}, \tag{6.13}$$

giving the full, time–dependent, adiabatic Hamiltonian:

$$\underline{\underline{H}}_{ad} = \begin{pmatrix} -\varepsilon & -i\gamma \\ i\gamma & \varepsilon \end{pmatrix}, \tag{6.14}$$

where

$$\gamma = \frac{aea_0}{2\varepsilon}\frac{dF}{dt},$$

giving equations of motion for the adiabatic states:

$$\frac{dc_1^A}{dt} = \frac{i\varepsilon(t)}{\hbar}c_1^A(t) - \frac{\gamma(t)}{\hbar}c_2^A(t), \tag{6.15}$$

$$\frac{dc_2^A}{dt} = \frac{\gamma(t)}{\hbar}c_1^A(t) - \frac{i\varepsilon(t)}{\hbar}c_2^A(t). \tag{6.16}$$

6.2 The adiabatic theorem

If we define the time–evolution operator $\hat{T}(t, t_0)$ by the integral equation

$$\hat{T}(t, t_0) = 1 - \frac{i}{\hbar}\int_{t_0}^{t} \hat{H}(t')\hat{T}(t', t_0)dt' \tag{6.17}$$

then it can be used to determine the dynamic evolution of the system through equation 6.18.

$$\psi(t) = \hat{T}(t, t_0)\psi(t_0) \tag{6.18}$$

where the duration of the evolution is given by $\tau = t - t_0$.

The problem described at the beginning of this chapter is now simply to determine how $\hat{T}(t, t_0)$ depends on τ. In the limit $\tau \to 0$ for a given final state, we have an infinitely rapid passage and the dynamical state of the system remains unchanged,

$$\lim_{\tau \to 0} \hat{T}(t, t_0) = 1, \tag{6.19}$$

the system follows the *diabatic path*.

In the limit $\tau \to \infty$, for a given final state we have an infinitely slow passage. If the system is initially in an eigenstate of $\hat{H}(t_0)$, it will pass through the corresponding stationary states of $\hat{H}(t)$ for all t, ending in a stationary state of $\hat{H}(t)$. This important result is known as the adiabatic theorem of quantum mechanics.[65]

6.2.1 The Landau–Zener Approximation

For a fully quantum–mechanical treatment of a general system, the equations of motion for the system (equations 6.5) cannot be solved analytically. In 1932, two closely related papers by Landau[66] and Zener[67] were published on the subject of diabatic transitions between quantum states. Such transitions occur between states of the *entire system*, hence any description of the system must include all external influences, including collisions and external electric and magnetic fields.

In order that the equations of motion for the system might be solved analytically, a set of simplifications are made, known collectively as the Landau–Zener approximation. The simplifications are as follows:

1. The perturbation parameter is a known, linear function of time

2. The energy separation of the diabatic states varies linearly with time
3. The coupling a in the diabatic Hamiltonian matrix is independent of time

The first simplification makes this a semi-classical treatment. In the case of our model system, a Rydberg atom in an electric field, the field strength becomes a classical variable which can be precisely measured during the transition. This requirement is quite restrictive as a linear change may not be the optimal profile to achieve the desired transition probability.

The second simplification allows us to make the substitution $E_2(t) - E_1(t) \equiv \alpha t$; for our model system this corresponds to a linear change in electric field strength. For a linear Stark shift this follows directly from point 1.

The final simplification requires that the time–dependent perturbation does not couple the diabatic states; rather, the coupling must be due to a static deviation from a $1/r$ coulomb potential, commonly described by a quantum defect.

The details of Zener's solution are somewhat opaque, relying on a set of substitutions to put the equation of motion into the form of the Weber equation[1] and using the known solution. A more transparent solution is provided by Wittig using contour integration.[68]

Probability calculations

A key figure of merit is known as the Landau–Zener velocity v_{LZ}, given in general by

$$v_{LZ} = \frac{\dfrac{\partial}{\partial t}\left|E_2 - E_1\right|}{\dfrac{\partial}{\partial q}\left|E_2 - E_1\right|} \approx \frac{dq}{dt}. \tag{6.20}$$

Zener's model system used the internuclear distance within a diatomic molecule as the perturbation variable with the consequence that his v_{LZ} was in fact the relative

[1]See *Handbook of Mathematical Functions,* 9th *edition*, M. Abramowitz and I. A. Stegun, p. 498.

nuclear velocity. For our model system, v_{LZ} is given by

$$v_{LZ} = \frac{dF}{dt}, \tag{6.21}$$

where F is the magnitude of the electric field strength. This can be understood with reference to the time evolution operator given in equation 6.18. A large v_{LZ} corresponds to a small τ and the system follows the diabatic path, while a small v_{LZ} ensures the system follows the adiabatic path.

The final result given by Zener (and previously by Landau with an error of 2π in the exponent) is given in equation 6.22, which gives the probability that the system has followed the diabatic path.

$$\begin{aligned} P_D &= e^{-2\pi\Gamma} \\ \Gamma &= \frac{a^2/\hbar}{\left|\frac{\partial}{\partial t}(E_2 - E_1)\right|} = \frac{a^2/\hbar}{\left|\frac{dq}{dt}\frac{\partial}{\partial q}(E_2 - E_1)\right|} \\ &= \frac{a^2}{\hbar|\alpha|} \end{aligned} \tag{6.22}$$

To summarize; if the system is prepared initially in state $|1\rangle$ and q is increased linearly with time, P_D is the probability that the system will end in state $|1\rangle$.

The behaviour of the system around the avoided crossing depends on the slopes of the energy levels, which for an atom in an electric field is equivalent to the electric dipole moment, and the rate of change of q, equivalent to the electric field slew–rate.

Solutions for the adiabatic state amplitudes were obtained through numerical solution of the equations of motion given in equations 6.15 and 6.16; see appendix C for code implementing these solutions. As a test of these solutions, the probability of a diabatic transition was compared with that predicted by the Landau–Zener formula, under the required conditions, for a variety of field slew–rates. The results are shown in figure 6.3.

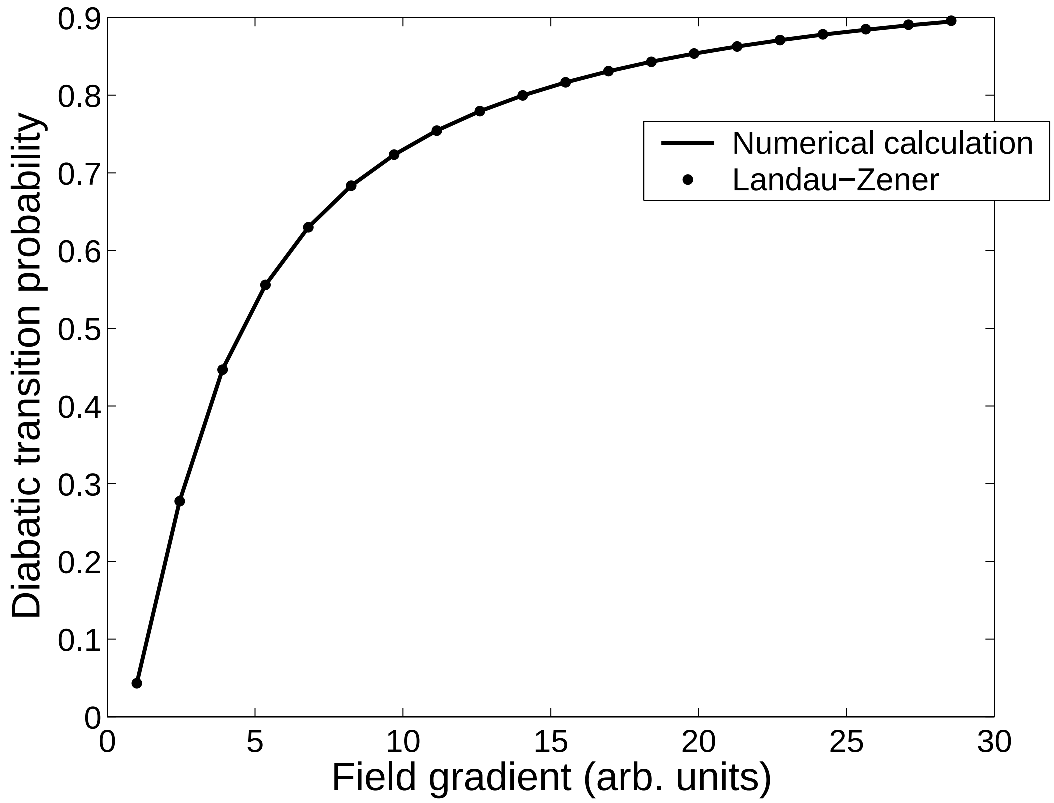

Figure 6.3: Comparing the results of a numerical solution with the Landau–Zener solution; the curve representing the Landau–Zener solutions has been translated slightly for clarity.

6.2.2 Beyond the Landau–Zener approximation

Having established the veracity of the numerical solutions, we now have the tools to move beyond the restrictions imposed by the Landau–Zener formula. We are able to observe the probability of a diabatic transition, for any arbitrary electric field profile. Figure 6.4 shows the effects of three different field profiles on the adiabatic state energies and populations. While the three profiles are different, the durations of the

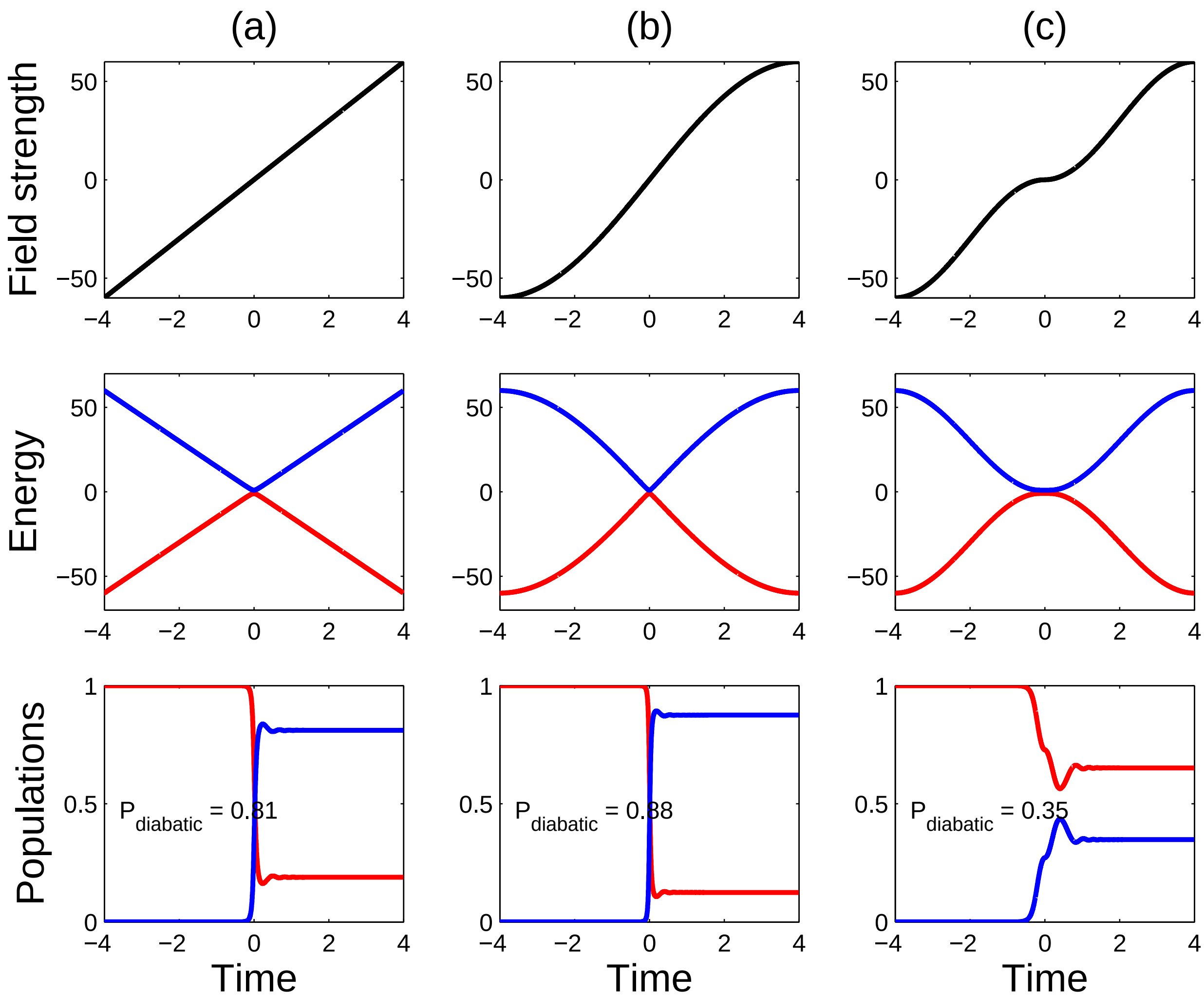

Figure 6.4: Adiabatic state populations and energies for different field ramp profiles. Note that the linear ramp leads to the highest probability of a diabatic transition.

interactions and the total field strength changes are identical.

It is immediately clear that restricting oneself to profiles that can be described by the Landau–Zener formula is extremely problematic if the probability of a diabatic transition is to be minimized. By reducing the Landau–Zener velocity (time–derivative of the electric field strength) at the time when the two states are energetically closest, the probability of a diabatic transition can be significantly reduced compared to the Landau–Zener case.

Obtaining the profile that minimizes the diabatic transition probability for a given duration and change in field strength will be left for future work.

Chapter 7

Adiabatic Population Transfer

The ability to precisely control the state of a population of atoms or molecules is the key to the efficient production of electronic Rydberg states and opens up pathways through the energy level manifolds to heavy Rydberg states just below the continuum.

Optical excitation using a narrow–band laser light source can be used effectively to populate an excited state separated from the ground state by the laser frequency. However, the state remains coupled to the light field, and stimulated emission can lead to rapid depletion of the excited state population.

For a certain class of atomic and molecular systems, there exists a coherent superposition of low lying states which does not couple to the light field. Consequently the population is effectively trapped, in a phenomenon known as *coherent population trapping* (CPT).[69] The use of the non–coupled or “dark” state as a bridging state to effect transfer between the two constituent states provides a powerful tool for precise control over the energetic states of atoms and molecules.

The code used to implement solutions to the amplitude equations describing the population dynamics of multi–level systems is given in appendix D.

7.1 The 3–level system: Λ configuration

The simplest system in which coherent population trapping can be observed is a 3–level system in the Λ configuration; see figure 7.1. Such systems appear in the energy level schemes of most, if not all, atomic and molecular species. In a real physical system the dynamics are complicated by the presence of additional states in the energetic vicinity of the target Λ system; a model system, comprising only the requisite three levels, serves to simplify the problem.

7.1.1 Features of the Λ system

- Closely spaced "ground" states $|1\rangle$ and $|2\rangle$
- Large separation between ground states and excited state $|3\rangle$
- The $|1\rangle \leftrightarrow |2\rangle$ transition is dipole forbidden
- Monochromatic light fields, with frequencies ω_{13}^L and ω_{23}^L, near–resonant with $|1\rangle \leftrightarrow |3\rangle$ and $|2\rangle \leftrightarrow |3\rangle$ transitions respectively, henceforth referred to as laser 1 and laser 2
- Δ_1 and Δ_2 are detunings for each transition, $\Delta_x = w_{x3}^L - \omega_{3x}$
- Ω_{31} and Ω_{32} are the Rabi frequencies for the transitions and the respective laser beams, $\Omega_{ij} = \frac{e\langle i|\vec{r}|j\rangle.\vec{E}_0}{\hbar}$
- Separation of ground states sufficient to prevent 'crosstalk', i.e. Ω_{3x} depends only on intensity of light with frequency ω_x
- Relaxation from $|3\rangle$ with rate Γ, to states outside the Λ–system. No relaxation within system

Note: figure captions include a statement of conditions in the form:

$$\{[\rho_{11}^0,\rho_{22}^0,\rho_{33}^0],[\Delta_1\ (\mathrm{s}^{-1}),\Delta_2\ (\mathrm{s}^{-1})],\left[\frac{\Omega_{31}}{ea_0(1000\ \mathrm{Vm}^{-1})/\hbar},\frac{\Omega_{32}}{ea_0(1000\ \mathrm{Vm}^{-1})/\hbar}\right],\Gamma\ (\mathrm{s}^{-1})]\},$$

where ρ_{ii}^0 is the initial population of state $|i\rangle$ and the Rabi frequency is given in units of $ea_0(1000\ \mathrm{Vm}^{-1})/\hbar = 8.08 \times 10^7\ \mathrm{s}^{-1}$. For reference, a laser intensity of 1 mWmm^{-2}, with a transition dipole moment of ea_0, gives $\Omega = 7.01 \times 10^7 \mathrm{s}^{-1}$. The Rabi frequencies noted for the adiabatic population transfer figures are peak values.

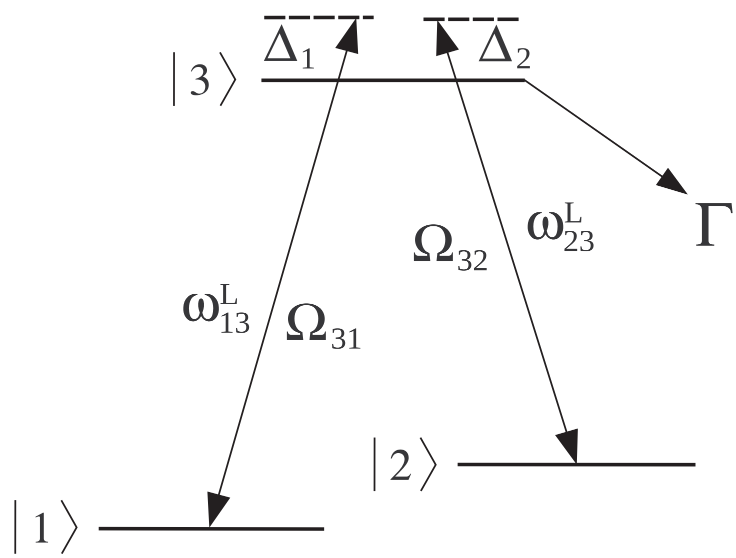

Figure 7.1: Energy level scheme of a 3–level system in a Λ configuration, including the Rabi frequency for each allowed transition and corresponding light field, the frequency of each light field, the detunings and the excited state decay rate.

The system wavefunction in the interaction picture is given by

$$|\Psi\rangle = \sum_{n=1}^{3} \tilde{c}_n e^{-iE_n t/\hbar} |n\rangle. \tag{7.1}$$

Through a judicious choice of phase factors, explicit time dependence can be removed from the Hamiltonian matrix:

$$\begin{aligned} c_1 &= \tilde{c}_1 \\ c_2 &= \tilde{c}_2 e^{i(\Delta_1 - \Delta_2)t/\hbar} \\ c_3 &= \tilde{c}_3 e^{i\Delta_1 t/\hbar} \end{aligned} \tag{7.2}$$

From the time–dependent Schrödinger equation,

$$i\hbar \frac{d}{dt}\underline{c} = \underline{\underline{H}}\,\underline{c}, \tag{7.3}$$

we derive the equations of motion for the state amplitudes within the Λ system:

$$\begin{pmatrix} \dot{c}_1 \\ \\ \dot{c}_2 \\ \\ \dot{c}_3 \end{pmatrix} = \begin{pmatrix} 0 & 0 & -i\frac{\Omega_{31}^*}{2} \\ \\ 0 & i(\Delta_1 - \Delta_2) & -i\frac{\Omega_{32}^*}{2} \\ \\ -i\frac{\Omega_{31}}{2} & -i\frac{\Omega_{32}}{2} & i\Delta_1 - \frac{\Gamma}{2} \end{pmatrix} \begin{pmatrix} c_1 \\ \\ c_2 \\ \\ c_3 \end{pmatrix}. \tag{7.4}$$

7.1.2 Coherent Population Trapping

Figure 7.2 shows the population dynamic of a 3–level system iluminated with two light fields, resonant with the two dipole allowed transitions, with no relaxation. Figure 7.3 shows the same system with relaxation from the excited state, illustrating the concept of coherent population trapping in which there is a coherent superposition of ground states $|1\rangle$ and $|2\rangle$ which will not absorb energy from either light field and is hence not coupled to state $|3\rangle$. As atoms in this state are non–absorbing, this effect is also known as electromagnetically induced transparency.

To further understand this phenomenon it is instructive to examine the system in a new basis. The ground states are now represented by the non–absorbing dark state,

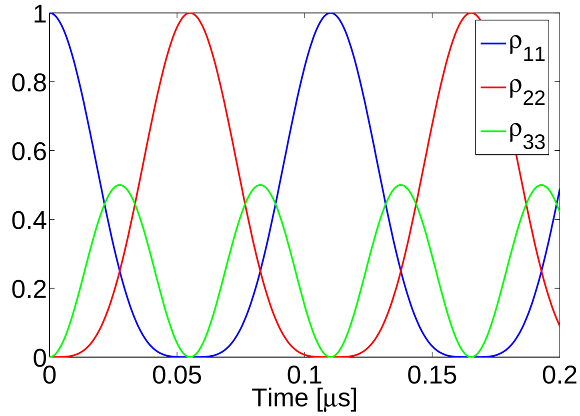

Figure 7.2: Rabi flopping in a 3–level Λ system; population oscillates between states $|1\rangle$ and $|2\rangle$, passing through state $|3\rangle$, with no more than half the population in the excited state at any time. {[1,0,0],[0,0],[1,1],0}

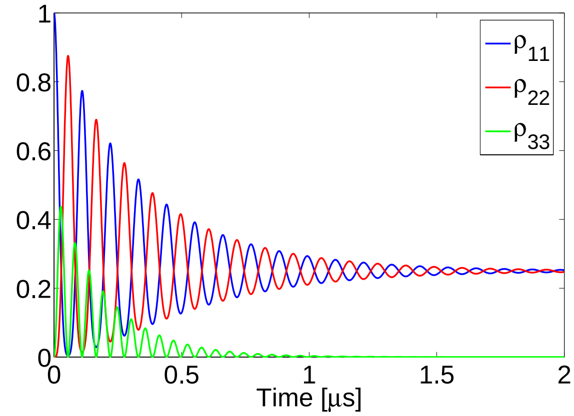

Figure 7.3: Coherent population trapping in a 3–level Λ system; relaxation from state $|3\rangle$ decreases the total system population, however a finite steady state population remains, split between states $|1\rangle$ and $|2\rangle$.

$|D\rangle$, and an absorbing state, $|A\rangle$; the excited state $|3\rangle$ remains.

$$|D\rangle = \left(\frac{\Omega_{32}}{\Omega}\right)|1\rangle - \left(\frac{\Omega_{31}}{\Omega}\right)|2\rangle \tag{7.5}$$

$$|A\rangle = \left(\frac{\Omega_{31}^*}{\Omega}\right)|1\rangle + \left(\frac{\Omega_{32}^*}{\Omega}\right)|2\rangle \tag{7.6}$$

$$|3\rangle = |3\rangle$$

$$\Omega = \sqrt{|\Omega_{31}|^2 + |\Omega_{32}|^2}$$

On deriving the Hamiltonian matrix in the new basis, the condition under which the dark state is decoupled from the light fields is immediately clear. Under the condition known as *Raman detuning*, expressed mathematically as $\Delta_1 = \Delta_2$, the rate of change of the dark state amplitude is identically zero.

$$\begin{pmatrix} \dot{c_D} \\ \\ \dot{c_A} \\ \\ \dot{c_3} \end{pmatrix} = \begin{pmatrix} i(\Delta_1-\Delta_2)\frac{|\Omega_{31}|^2}{\Omega^2} & -i(\Delta_1-\Delta_2)\frac{\Omega_{31}^*\Omega_{32}^*}{\Omega^2} & 0 \\ \\ -i(\Delta_1-\Delta_2)\frac{\Omega_{31}\Omega_{32}}{\Omega^2} & i(\Delta_1-\Delta_2)\frac{|\Omega_{32}|^2}{\Omega^2} & -i\frac{\Omega}{2} \\ \\ 0 & -i\frac{\Omega}{2} & i\Delta_1-\frac{\Gamma}{2} \end{pmatrix} \begin{pmatrix} c_D \\ \\ c_A \\ \\ c_3 \end{pmatrix}. \quad (7.7)$$

Figure 7.4 illustrates the behaviour of the same system, under the same conditions, as figure 7.3, described in the dark/absorbing basis. The steady state population is entirely in the dark state, which has remained unaffected by relaxation from the excited state. The oscillation and decay of the population in states $|1\rangle$ and $|2\rangle$ are entirely in the absorbing state.

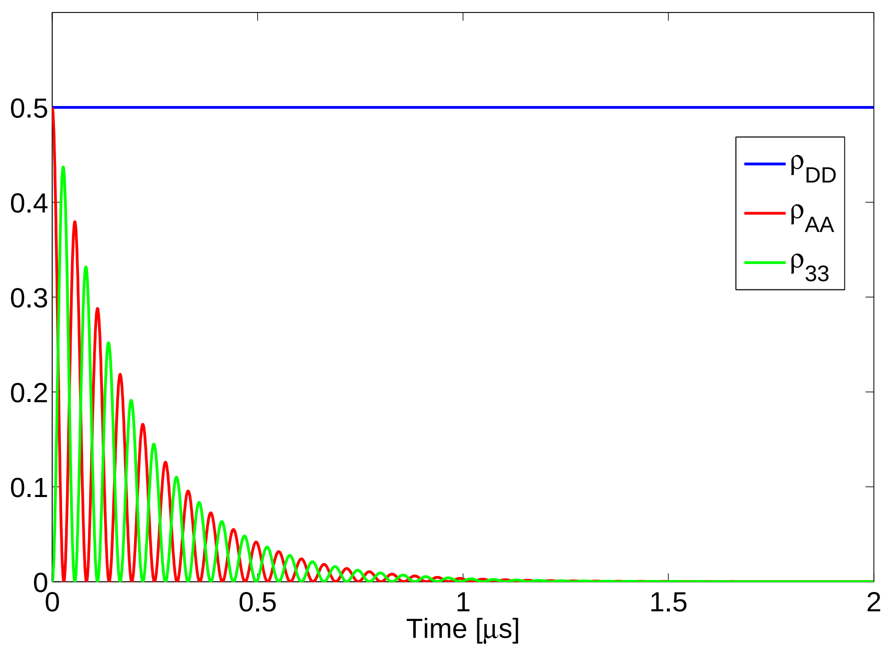

Figure 7.4: Coherent population trapping in a 3–level Λ system, examined in the dark/absorbing basis. The population of the dark state remains constant, resulting in the observed steady state population; the decay from states $|1\rangle$ and $|2\rangle$ is due to the coupling between the absorbing state, and the excited state with its finite relaxation rate. {[1,0,0],[0,0],[1,1],10^7}

7.1.3 Adiabatic population transfer

An important application of this phenomenon is the ability to transfer populations between the ground states (a dipole forbidden transition) via the dark state, with very little population transferred to the excited state from where it can be lost through relaxation processes.

Equation 7.8 gives the dark state amplitude, c_D, in terms of the amplitudes of states $|1\rangle$ and $|2\rangle$, c_1 and c_2 respectively. The coefficients are the Rabi frequencies, which are proportional to the electric field amplitudes,

$$c_D = \frac{\Omega_{32}^*}{\Omega} c_1 - \frac{\Omega_{31}^*}{\Omega} c_2. \tag{7.8}$$

Turning on laser 2 creates a dark state composed entirely of state $|1\rangle$. If this is then turned off slowly, while laser 1 is turned on slowly, the composition of the dark state changes until it is composed entirely of state $|2\rangle$. The process is illustrated in figures 7.5 and 7.6.

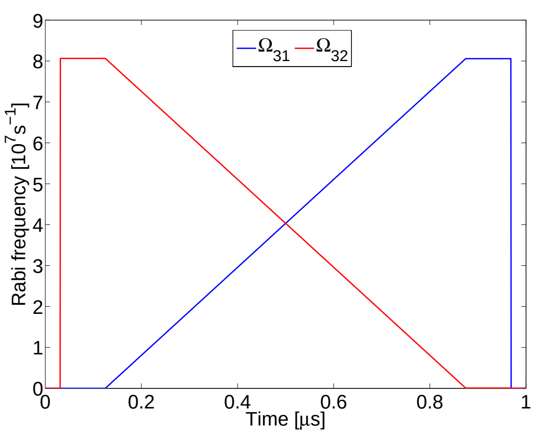

Figure 7.5: Change in Rabi frequencies due to a linear electric field ramp; the Rabi frequencies are proportional to the electric field amplitudes of their respective light fields.

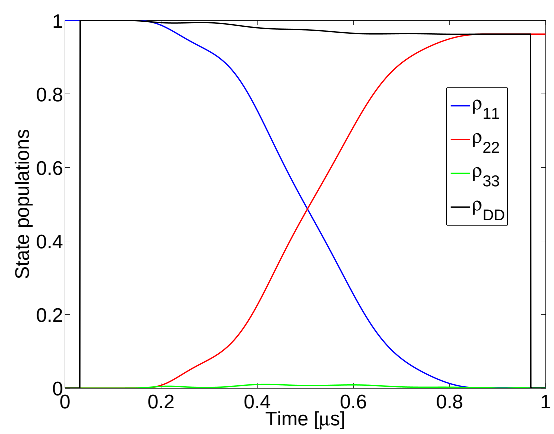

Figure 7.6: Population is transferred adiabatically from state $|1\rangle$ to state $|2\rangle$ utilizing the fact that the composition of the dark state depends on the relative magnitudes of the relevant Rabi frequencies. $\{[1,0,0],[0,0],[1,1],10^7\}$

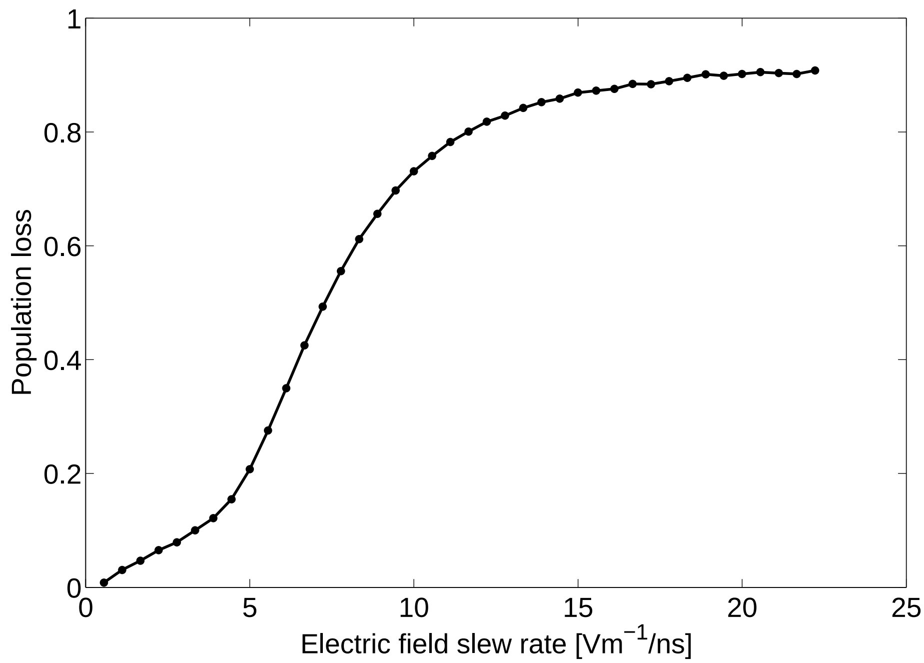

Figure 7.7: Population loss as a function of electric field slew rate; note the nearly linear relationship at rates below about 4 Vm^{-1}/ns. {[1,0,0],[0,0],[1,1],10^7}

Note that a truly adiabatic process occurs at a rate of zero; the non-zero rate of the electric field ramps leads to a finite non–adiabaticity, resulting in some population transfer to state $|3\rangle$, and hence the population loss through relaxation seen in figure 7.6, given by

$$\text{population loss} = \Gamma \int \rho_{33}\, dt. \tag{7.9}$$

In order to quantify this, a series of simulations were done using different rates; the results are shown in figure 7.7.

The population transfer shown in figure 7.6 is accomplished using a linear change in electric field strength. In order to simulate more realistic experimental conditions, two other forms were investigated.

There are numerous ways to directly control laser intensity. These can be as simple as adjusting the injection current supplied to a diode laser, however the changing charge density in the cavity will modify the frequency emitted by the laser. A practical solution is to pass a laser, resonant with the $|1\rangle \leftrightarrow |3\rangle$ transition, through an acousto–optic modulator (see section 3.1.3) such that the diffracted beam is downshifted by the ground state splitting. The amplitudes of the diffracted and undiffracted beams depend on the amplitude of the acoustic wave, which can be controlled by varying the applied RF bias. Intensity is related to electric field amplitude by

$$I = \frac{1}{2} c\epsilon_0 |\vec{E}_0|^2. \tag{7.10}$$

Figure 7.9 shows the results of a simulated population transfer achieved with a linear change in *intensity*; figure 7.8 illustrates the changes in the Rabi frequencies during this process. This was expected to give a very similar result to that achieved with a linear change in electric field strength, possibly with a slightly larger population loss due to the rapid initial change in electric field strength. In fact the results show dramatic oscillations, which are difficult to relate to changing Rabi frequencies. As yet the oscillations are unexplained and may be an artifact of the simulation.

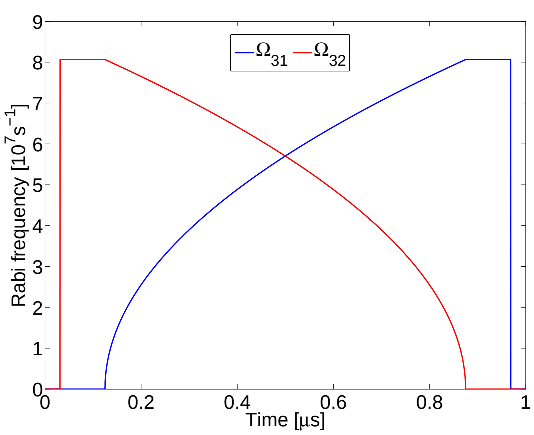

Figure 7.8: Change in Rabi frequencies due to a linear change in intensity.

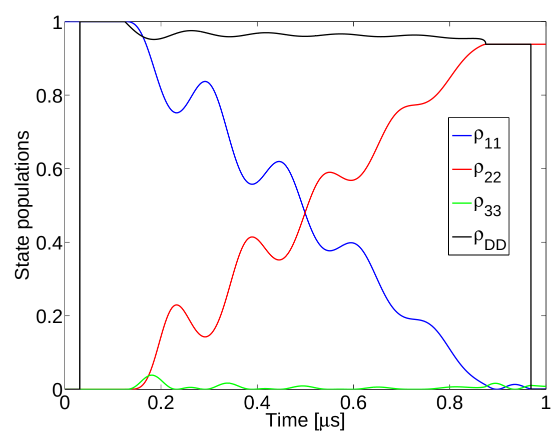

Figure 7.9: Population transfer still occurs, however there is an unexplained oscillation which may or may not be physical. $\{[1,0,0],[0,0],[1,1],10^7\}$

There is a technique for implementing adiabatic population transfer in an atomic or molecular beam, known as stimulated Raman adiabatic passage (STIRAP).[70] Atoms or molecules passing consecutively through the overlapped beams of lasers 2 and 1 experience a pair of approximately Gaussian intensity profiles due to the two beams. If the two beams are parallel and partially overlap it should effect adiabatic population transfer; i.e. a dark state composed entirely of state $|1\rangle$ is created as an atom enters the beam of laser 2; as it passes into the beam of laser 1, the composition of the dark state will change until it is entirely composed of state $|2\rangle$. Once out of the beam region there will be no dark state and the atom will simply be in state $|2\rangle$.

A simulation of the beam experiment was constructed including the likely experimental conditions. The beamwidth was chosen to be 1 mm; the velocity of the atoms was calculated using equation 7.11 and assuming ^{7}Li was vaporised at an oven temperature of 500°C, leading to a velocity of approximately 1500 ms^{-1}. Figure 7.10 shows how the Rabi frequencies vary as the atoms traverse the beam; figure 7.11 shows the resulting changes in the populations of the states.

$$v = \sqrt{\frac{3kT}{m}} \tag{7.11}$$

7.1.4 Departure from Raman detuning

The existence of the dark state depends on a condition known as Raman detuning, whereby the detunings of the lasers from their respective transitions are equal; $\Delta_{12} = \Delta_1 - \Delta_2 = 0$ (see figure 7.1). In an experimental setting such requirements can never be met exactly and it becomes useful to know how sensitive the system is to deviations from ideal conditions. With perfect Raman detuning, we expect a steady state population of 0.5 (see figure 7.3). Any deviation from this will lead to population decay, eventually resulting in total depopulation of the system. By approximating the decay as exponential, a time constant can be calculated giving a quantitative measure

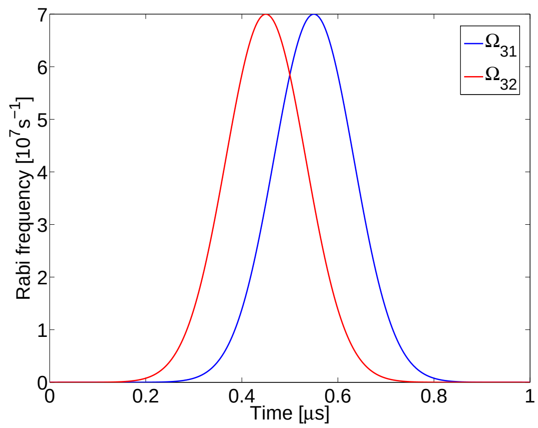

Figure 7.10: Variation in Rabi frequency as an atomic beam passes through a pair of Raman detuned laser beams with peak intensities 1 mWmm^{-2}.

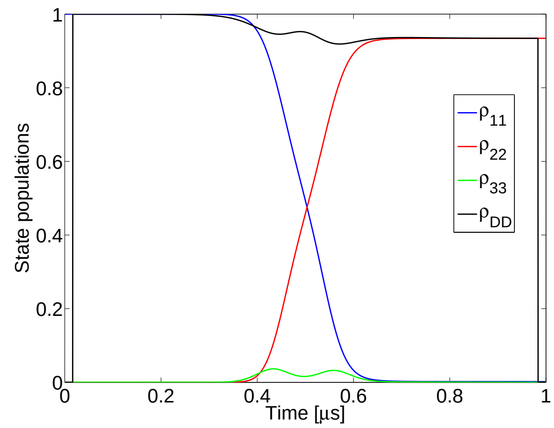

Figure 7.11: By optimising parameters such as beam width, peak intensity and beam overlap in order to minimise the electric field slew rate, population loss can be minimised. $\{[1,0,0],[0,0],[1,1],10^7\}$

of the life–time of the dark state for a given Δ_{12}. Figure 7.12 illustrates the decay of the total system population for different values of Δ_{12}; figure 7.13 shows how the time–constant of the decay varies with Δ_{12}.

7.2 The 4–level system – double Λ configuration

Extending the model, we now look at the effect of adding a second excited state with allowed transitions to each of the ground states.

7.2.1 Features of the double Λ system

- Second excited level $|4\rangle$ with separation from $|3\rangle$ given by Δ_4, small enough that laser with frequency ω_{x3}^L couples to both $|x\rangle \leftrightarrow |3\rangle$ and $|x\rangle \leftrightarrow |4\rangle$ transitions.

- $\Delta_x + \Delta_4$ gives the detuning of laser frequency ω_{x3}^L from the $|x\rangle \leftrightarrow |4\rangle$ transition.

- Relaxation rates from excited state $|y\rangle$ to state(s) outside the system, given by Γ_y.

- Both $|1\rangle \leftrightarrow |2\rangle$ and $|3\rangle \leftrightarrow |4\rangle$ transitions dipole forbidden.

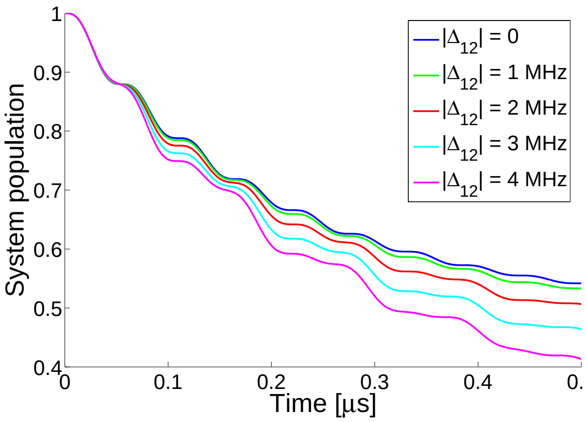

Figure 7.12: As ω_{13}^L increases, $\Delta_{12} = \Delta_1 - \Delta_2$ increases leading to a more rapid decay. {[1,0,0],[0,0],[1,1],10^7}

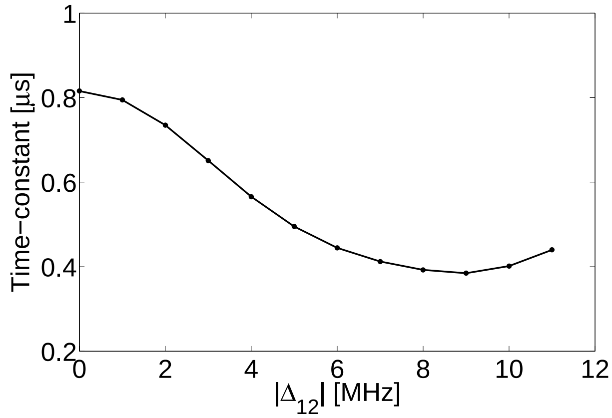

Figure 7.13: As the system moves further from Raman detuning the decay time–constant decreases. At a certain point Δ_1 is such that the slow transfer of population from $|1\rangle$ to $|3\rangle$ increases the time–constant.

- Again no relaxation within the system.

The double Λ system illustrated in figure 7.14 displays much of the same behaviour as the Λ system illustrated in figure 7.1, the lasers tuned to the $|x\rangle \leftrightarrow |3\rangle$ transitions couple only weakly to the $|x\rangle \leftrightarrow |4\rangle$ transitions. There is however a stringent additional condition required to produce a dark state which is associated with any system that allows different paths to be taken between the ground states. Known as closed level schemes, the existence of a dark state in such systems shows a strong dependence on the phase of the wavefunction, including the phase of the atom and the phases of the light fields.[71] A nice analogy is a wave on a piece of string; the wave can have any phase until the string is closed to form a loop, at which point the phase difference around the loop must be an integer multiple of 2π. The phase condition is given by equation 7.12,

$$\Phi = \Phi_{atom} + (\phi_{13} - \phi_{23}) = 2\pi n, \qquad n = 1, 2, 3, ..., \tag{7.12}$$

$$\Phi_{atom} = (\chi_1 - \chi_2) - (\chi_3 - \chi_4),$$

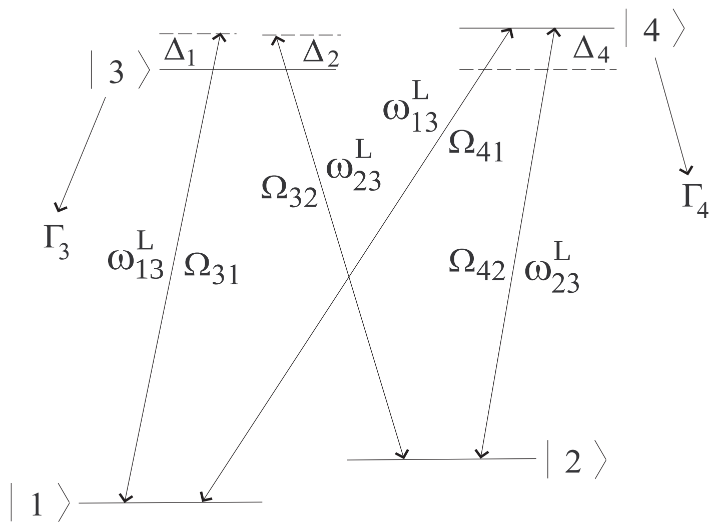

Figure 7.14: Energy level scheme of a 4–level system in a double Λ configuration, including the Rabi frequency for each allowed transition and corresponding light field, the frequency of each light field, the detunings and the excited state decay rate. An example of such a system is the hyperfine structure of the D1 line in lithium–6 and lithium–7, see figure 3.1.

where ϕ_{x3} is the initial phase of the laser with frequency ω^L_{x3} and χ_y is the initial phase of the $\langle y|\hat{d}|y\rangle$ element of the electric dipole matrix.

Both stable isotopes of lithium (^{6}Li and ^{7}Li) have a classic double Λ system in the hyperfine structure of the $^2S_{1/2} \leftrightarrow {}^2P_{1/2}$ transition, see figure 3.1.

Note: Subsequent figure captions include a statement of conditions in the form:

$$\{[\rho^0_{11},\rho^0_{22},\rho^0_{33},\rho^0_{44}],[\Delta_1\ (\mathrm{s}^{-1}),\Delta_2\ (\mathrm{s}^{-1})],\frac{1}{ea_0(1000\ \mathrm{Vm}^{-1})/\hbar}[\Omega_{31},\Omega_{32},\Omega_{41},\Omega_{42}],[\Gamma_3\ (\mathrm{s}^{-1}),\Gamma_4\ (\mathrm{s}^{-1})]\}.$$

Figures 7.15 and 7.16 show the level populations in the 4 level system with relaxation from states $|3\rangle$ and $|4\rangle$. Figure 7.15 shows the evolution of the system under the *symmetric* phase condition described in equation 7.12, equivalent to the statements:

$$\frac{|\Omega_{41}|}{|\Omega_{31}|} = \frac{|\Omega_{42}|}{|\Omega_{32}|}, \qquad \Omega_{ij} = |\Omega_{ij}|e^{i\theta_{ij}} \tag{7.13}$$

$$\Theta = (\theta_{42} - \theta_{32}) - (\theta_{41} - \theta_{31}) = 2n\pi, \qquad n = 1, 2, 3, ...$$

Figure 7.16 shows the result of deviation from symmetric phase: the dark state decays even though the Raman detuning condition is satisfied.

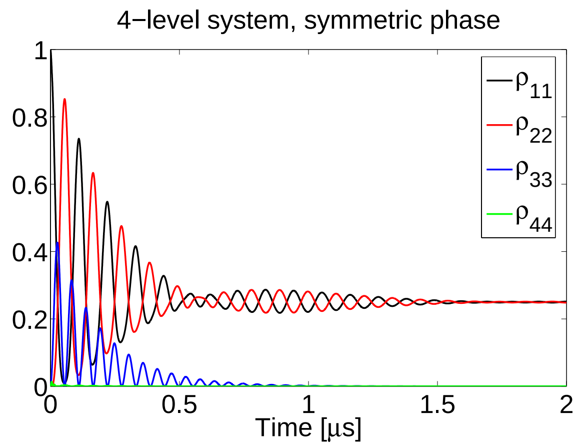

Figure 7.15: Coherent population trapping in a double Λ system under a symmetric phase condition. {[1,0,0,0],[0,0],[1,1,1,1],[10^7,10^8]}

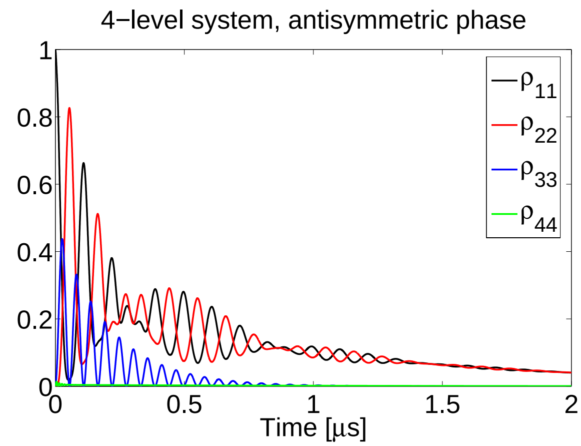

Figure 7.16: Under a non–symmetric phase condition, the dark state population decays. {[1,0,0,0],[0,0],[1,1,1,-1],[10^7,10^8]}

7.2.2 Decoupling the 4th level

The frequency splitting Δ_4 between the two excited levels is important in determining the strength of the phase dependence. As $\Delta_4 \to \infty$, state $|4\rangle$ is decoupled from the system and we have a 3–level Λ system with no phase dependence. In order to quantify this effect, a study was made of the dark state lifetime as a function of Δ_4. In the anti–symmetric phase condition described by equation 7.14, there is no dark state; the system absorbs energy from the light fields and decays rapidly due to the relaxation from states $|3\rangle$ and $|4\rangle$.

$$\Phi = \Phi_{atom} + (\phi_{13} - \phi_{23}) = (2n+1)\pi, \qquad n = 1, 2, 3, ... \tag{7.14}$$

Figures 7.17 and 7.18 demonstrate how increasing the frequency splitting between $|3\rangle$ and $|4\rangle$ increases the time constant of this decay, by decoupling the 4th level.

These results demonstrate the potential of phase–dependent coherent population

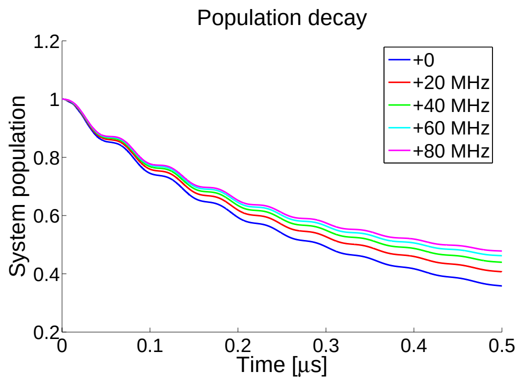

Figure 7.17: Decoupling the 4^{th} level. Decay of the total system population is slower for a larger Δ_4 due to the weaker coupling between the light fields and state $|4\rangle$ (smaller Ω_{41} and Ω_{42}, due to less overlap between state $|4\rangle$ and the ground states, hence smaller $\langle 4|\hat{r}|x\rangle$). {[1,0,0,0],[0,0],[1,1,1,-1],[10^7,10^8]}

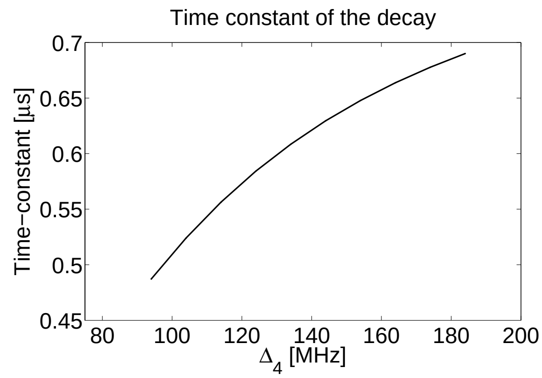

Figure 7.18: Modelling the decay as exponential, the time constants are calculated for a range of values of Δ_4.

trapping as the basis for future experiments involving coherent control of quantum systems. Using the AOM driver presented in chapter 3, direct control of the phase of the light field is simply a matter of providing a tuning voltage to the RF phase shifter, providing a simple mechanism for control over the existence of the dark state.

Chapter 8

Conclusions and Future Work

Significant progress has been made in the provision of tools to facilitate efficient production of heavy Rydberg systems.

The construction of a full–featured, low–cost driver for an acousto–optic modulator began a series of projects aimed at providing a recently established experimental physics laboratory with the tools required for experiments planned for the near future. Characterization of this device has demonstrated its utility for the purpose of accessing hyperfine transitions within the D1 and D2 lines of the stable isotopes of lithium.

Many of the planned experiments will require lasers to operate on a single longitudinal mode. A device has been realized which enables real time monitoring of the mode structure of CW lasers, using as little as 3.3 μW from the beam under analysis. Should it become necessary to decrease this power requirement, a fourfold increase in sensitivity could be trivially introduced by reading the eight least significant bits from the sensor. In addition, future work may include adaptation for use with pulsed lasers, as described in **Program extensions**, section 4.4.4. Through the construction of this device, the applicability of programmable microcontrollers to the solution of problems encountered in experimental physics has been clearly demonstrated.

Results from numerical calculations showing the behaviour of a model quantum system in the vicinity of an avoided crossing have been presented, shedding light on a mechanism behind the formation of heavy Rydberg states from covalently bound molecules. The fundamental importance of the adiabatic theorem and the calculation of diabatic transition probabilities give this model system a wide applicability across a range of topics in atomic and molecular physics. These include collision theory, the design and implementation of magnetic and magneto–optical traps, and spectroscopic studies based on field ionization and dissociation. Limitations inherent in the assumptions made while deriving the Landau–Zener formula have been demonstrated, and numerical results for conditions violating these assumptions have been shown to provide superior results. Future development of the model will focus on adapting calculation to correspond with systems of interest in the laboratory, including atomic and molecular lithium.

The development of a simulation of the phenomenon of coherent population trapping in 3– and 4–level systems, has provided insight into the experimental implementation and optimization of coherent control techniques such as STIRAP. The effect of experimental errors in the frequencies of the two light fields has been quantified, along with the use of the phase of the light fields to control the formation of the non–coupled state. These results will form the basis for future experimental work on the study of electronic and heavy Rydberg states.

Bibliography

Introduction

[1] J. R. Anglin and W. Ketterle
Bose–Einstein Condensation of Atomic Gases
Nature, **416** (6877), 211–218, (2002).

[2] E. Reinhold and W. Ubachs
Heavy Rydberg States
Molecular Physics, **103** (10), 1329–1352, (2005).

[3] T. F. Gallagher
Rydberg Atoms
Cambridge University Press, (1994).

[4] A. J. Yencha and A. Hopkirk
Ion–Pair Formation in Halogen–Containing Molecules via VUV Photoexcitation of Rydberg States
Journal of Electron Spectroscopy and Related Phenomena, **79**, 377–380, (1996).

Literature Review

[5] A. Fowler
New Series of Lines in the Spark Spectrum of Magnesium
Proceedings of the Royal Society of London, **71**, 419–420, (1903).

[6] J. Roncin, N. Damany and J. Romand
Far Ultraviolet Absorption Spectra of Atoms and Molecules Trapped in Rare Gas Matrices at Low Temperature
Journal of Molecular Spectroscopy, **22**, 154–164, (1967).

[7] J. Lundin and L. Holmlid
Electron Excitation Energy Transfer from Highly Excited Cs Atoms Forming High Rydberg State Atoms and Molecules
Journal of Physical Chemistry, **95** (3), 1029–1034, (1991).

[8] F. J. Deck, E. A. Hessels and S. R. Lundeen
Population of High–L Sulfur Rydberg Levels by Ion–Rydberg Atom Charge Exchange
Physical Review A, **48** (6), 4400–4404, (1993).

[9] A. J. Melmed and J. J. Carroll
CW Operation of an Organic Dye Solution Laser
Applied Physics Letters, **17** (6), 245–247, (1970).

[10] J. Farley, P. Tsekeris and R. Gupta
Hyperfine–Structure Measurements in the Rydberg S and P States of Rubidium and Cesium
Physical Review A, **15** (4), 1530–1536, (1977).

[11] P. M. Koch
Rydberg States of Atoms and Molecules
Cambridge University Press, (1983).

[12] J. Deiglmayr, M. Reetz–Lamour, T. Amthor, S. Westermann, A. L. de Oliveira and M. Weidemüller
Coherent Excitation of Rydberg Atoms in an Ultracold Gas
Optics Communications, **264**, 293–298, (2006).

[13] H. J. Metcalf and P. van der Straten
Laser Cooling and Trapping of Atoms
Journal of the Optical Society of America B, **20** (5), 887–908, (2003).

[14] J. Guo, E. Korsunskyz and E. Arimondo
Laser Cooling of Rydberg Atoms by Velocity–Selective Coherent Population Trapping
Quantum Semiclassical Optics, **8**, 557–569, (1996).

[15] H. L. Bethlem, G. Berden and G. Meijer
Decelerating Neutral Dipolar Molecules
Physical Review Letters, **83** (8), 1558–1561, (1999).

[16] T. P. Softley, S. R. Procter, Y. Yamakita, G. Maguire and F. Merkt
Controlling the Motion of Hydrogen Molecules: Design of a Two–Dipole Rydberg Decelerator
Journal of Electron Spectroscopy and Related Phenomena, **144**, 113-117, (2005).

[17] L. E. Wright, E. L. Snow and S. R. Lundeen
Optical Spectroscopy of High-L Rydberg States of Argon
Physical Review A, **75**, 022503–022503-5, (2007).

[18] J. H. Choi, J. R. Guest, A. P. Povilus, E. Hansis and G. Raithel
Magnetic Trapping of Long-Lived Cold Rydberg Atoms
Physical Review Letters, **95** (24), 243001–243001-4, (2005).

[19] D. H. Tuan, S. Liberman and J. Pinard
Detection and Study of Rb I Rydberg States
Optics Communications, **18** (4), 533–535, (1976).

[20] A. Kalamarides, C. W. Walter, B. G. Lindsay, K. A. Smith and F. B. Dunning
Post–Attachment Interactions in K(nd)–CF_3I *Collisions at Intermediate n*
Journal of Chemical Physics, **91** (7), 4411–4413, (1976).

[21] A. G. Suits and J. W. Hepburn
ION PAIR DISSOCIATION: Spectroscopy and Dynamics
Annual Review of Physical Chemistry, **57**, 431–465, (2006).

[22] J. D. D. Martin and J. W. Hepburn
Determination of Bond Dissociation Energies by Threshold Ion–Pair Production Spectroscopy: An Improved D_0HCl
Journal of Chemical Physics, **109** (19), 8139–8142, (1998).

[23] R. C. Shiell, X. Hu, Q. J. Hu and J. W. Hepburn
Threshold Ion–Pair Production Spectroscopy (TIPPS) of H_2 and D_2
Faraday Discussions, **115**, 331–343, (2000).

[24] D. D. Konowalow and J. D. Fish
The Molecular Electronic Structure of the Twenty–Six Lowest Lying States of Li^2 at Short and Intermediate Internuclear Separations
Chemical Physics, **84**, 463–475, (1984).

[25] D. D. Konowalow and J. D. Fish
Low–Lying Electronic States of ${Li_2}^+$ and ${Li_2}^-$
Chemical Physics Letters, **104** (2,3), 210–215, (1984).

[26] E. Reinhold and W. Ubachs
Observation of Coherent Wave Packets in a Heavy Rydberg System
Physical Review Letters, **88** (1), 013001–013001-4, (2002).

[27] P. Horowitz and W. Hill
The Art of Electronics, 2^{nd} *edition*
Dover Publications, Inc. (1989).

[28] B. E. A. Saleh and M. C. Teich
Fundamentals of Photonics, 2^{nd} *edition*
John Wiley & Sons, Inc. (2007).

[29] E. V. D. Glazier and H. R. L. Lamont
The Services Textbook of Radio, Volume 5: Transmission and Propagation
Her Majesty's Stationary Office, (1958).

[30] G. M. Borsuk, A. Turley, G. Marx and E. Malarkey
Photosensor Array for Integrated Optical Spectrum Analyzer Systems
IEEE Transactions on Electron Devices, **26** (11), 1852–1853, (1979).

[31] I. A. McIntyre and M. H. Dunn
An Inexpensive Optical Spectrum Analyser for Measuring Laser Linewidths
Journal of Physics E: Scientific Instruments, **17**, 274–276, (1984).

[32] T. Saitoh, K. Nakamura, Y. Takahashi and K. Miyagi
Optical Spectrum Analyzer Utilizing MEMS Scanning Mirror
IEEE Photonics Technology Letters, **18** (6), 767–769, (2006).

Construction and Characterization of a Driver for an Acousto-Optic Modulator

[33] E. Arimondo, M. Inguscio and P. Violino
Experimental Determinations of the Hyperfine Structure in the Alkali Atoms
Reviews of Modern Physics, **49** (1), 31–75, (1977).

[34] R. Corey, A. Schmidt and P. Saulnier
Using a Moving Diffraction Grating to Simulate the Function of an Acousto-Optic Modulator
American Journal of Physics, **64** (5), 614–617, (1996).

[35] A. Korpel
Acousto-Optics – A Review of Fundamentals
Proceedings of the IEEE, **69** (1), 48–53, (1981).

[36] C. F. Quate, C. D. W. Wilkinson and D. K. Winslow
Interaction of Light and Microwave Sound
Proceedings of the IEEE, **53** (10), 1604–1622, (1965).

[37] E. I. Gordon
A Review of Acousto-Optical Deflection and Modulation Devices
Applied Optics, **5** (10), 1629–1639, (1966).

[38] C. V. Raman and N. S. N. Nath
The Diffraction of Light by High Frequency Sound Waves: Part IV
Proceedings of the Indian Academy of Science, **A** (3), 119–125, (1936).
`http://www.ias.ac.in/j_archive/proca/3/2/119-125/viewpage.html`
Retrieved July 11$^{\text{th}}$, 2007.

[39] V. Kotov, J. Stiens, G. Shkerdin and R. Vounckx
Cascade Acousto-Optic Frequency Shift of Light
Journal of Optics A: Pure and Applied Optics, **3** (6), 517–520, (2001).

[40] H. Eklund, A. Roos and S. T. Eng
Rotation of Laser Beam Polarization in Acousto-Optic Devices
Optical and Quantum Electronics, **7** (2), 73–79, (1975).

[41] IntraAction Corp.
ATM–A1/A2 Series Acousto-optic Frequency Shifters
`http://www.intraaction.com/FAQ_s/Contact_US/Definitions/Refrences/do_not_delete_page/ATM_A1-A2_series_05991.pdf`
Retrieved July 11$^{\text{th}}$, 2007.

[42] IntraAction Corp.
Model ATM–2001A1 Acousto–Optic Modulator
Instruction Manual, (2006).

[43] V. L. Ryjkov
Laser Cooling and Sympathetic Cooling in a Linear Quadrupole RF Trap
PhD Dissertation, Texas A&M University, (2003).

[44] IntraAction Corp.
ME Series Acousto–Optic Modulator Drivers
http://www.intraaction.com/Drivers/ME_Series.pdf
Retrieved July 11th, 2007.

[45] P. Horowitz and W. Hill
The Art of Electronics, 2nd *edition*
Dover Publications, Inc.
ch. 13, page 902, (1989).

[46] D. J. Griffiths
Introduction to Electrodynamics, 3rd *edition*
Prentice Hall International, Inc., (1999).

[47] M. N. O. Sadiku
Elements of Electromagnetics, 4th *edition*
Oxford University Press, (2007).

[48] F. Magnus, A. L. Boatwright, A. Flodin and R. C. Shiell
Optical Pumping and Electromagnetically Induced Transparency in a Lithium Vapour
Journal of Optics B: Quantum Semiclassical Optics, **7**, 109–118, (1999).

Real Time Laser Mode Structure Analysis

[49] P. W. Milonni and J. H. Eberly
Lasers, 1st *edition*
John Wiley & Sons, Inc.
ch. 3, page 109, (1988).

[50] M. Hercher
Tunable Single Mode Operation of Gas Lasers Using Intracavity Tilted Étalons
Applied Optics, **8** (6), 1103–1106, (1969).

[51] H. W. Schröder, H. Dux and H. Welling
Single–Mode Operation of CW Dye Lasers
Applied Physics, **7**, 21–28, (1975).

[52] C. E. Wieman and L. Hollberg
Using Diode Lasers for Atomic Physics
Review of Scientific Instruments, **62** (1), 1–20, (1991).

[53] T. Amthor, M. Sinther and T. Walther
An Injection–Locked, Single–Mode, Continuous Wave Ti:Sapphire Laser
Laser Physics Letters, **3** (2), 75–78, (2005).

[54] M. Born and E. Wolf
Principles of Optics, 7th *edition*
Cambridge University Press, (2002).

[55] Micron Technology, Inc.
Model MT9M001C12STM 1.3 Megapixel CMOS Digital Image Sensor
http://download.micron.com/pdf/datasheets/imaging/mt9m001_1300_mono.pdf
Retrieved July 15^{th}, 2007.

[56] E. R. Fossum and R. Nixon
CMOS Active Pixel Sensor Type Imaging System on a Chip
United States Patent 5841126, (1997).

[57] Microchip Technology, Inc.
Model PIC18F2320 28–pin High–Performance Enhanced Flash Microcontrollers
http://ww1.microchip.com/downloads/en/devicedoc/39599c.pdf
Retrieved July 15^{th}, 2007.

[58] R. Marbot
Phase–Locked Loop and Resulting Frequency Multiplier
United States Patent 5838178, (1998).

[59] M. Ugray, J. E. Atfield, T. G. McCarthy and R. C. Shiell
Microcontroller–Based Wavemeter Using Compression Locking of an Internal Mirror Reference Laser
Review of Scientific Instruments, **77** (11), 113109–113109-5, (2006).

Power Supplies

[60] P. Horowitz and W. Hill
The Art of Electronics, 2^{nd} *edition*
Dover Publications, Inc.
ch. 6, page 380, (1989).

The Adiabatic Theorem of Quantum Mechanics: Beyond the Landau–Zener Approximation

[61] A. Messiah
Quantum Mechanics
Dover Publications, Inc., (1999).

[62] J. R. Rubbmark, M. M. Kash, M. G. Littman and D. Kleppner
Dynamical Effects at Avoided Level Crossings: A Study of the Landau–Zener Effect Using Rydberg Atoms
Physical review A, **23** (6), 3107–3117, (1981).

[63] Y. Zeiri and G. G. Balint–Kurti
Theory of Alkali Halide Photofragmentation: Potential Energy Curves and Transition Dipole Moments
Journal of Molecular Spectroscopy, **99**, 1–24, (1983).

[64] S. Stenholm
Quantum Dynamics of Simple Systems, Stirling, August 1994
The 44th Scottish Universities Summer School in Physics, 267–313, (1994).

[65] T. Kato
On the Adiabatic Theorem of Quantum Mechanics
Journal of the Physical Society of Japan, **5** (6), 435–439, (1950).

[66] L. D. Landau
Zur Theorie der Energieubertragung. II
Physics of the Soviet Union, **2**, 46–51, (1932).

[67] C. Zener
Non–Adiabatic Crossing of Energy Levels
Proceedings of the Royal Society of London, Series A, **137** (6), 692–702, (1932).

[68] C. Wittig
The Landau–Zener Formula
Journal of Physical Chemistry B, **109** (17), 8428–8430, (2005).

Adiabatic Population Transfer

[69] L. Windholz
Coherent Population Trapping in Multi–Level Atomic Systems
Physica Scripta, **T95**, 81–91, (2001).

[70] K. Bergmann, H. Theuer and B. W. Shore
Coherent Population Transfer Among Quantum States of Atoms and Molecules
Reviews of Modern Physics, **70** (3), 1003–1025, (1998).

[71] E. A. Korsunsky, N. Leinfellner, A. Huss, S. Baluschev and L. Windholz
Phase–Dependent Electromagnetically Induced Transparency
Physical Review A, **59** (3), 2302–2305, (1999).

Appendix A

Assembly Code for PIC Microcontrollers

A.1 *SensorPIC* code

```
;;;;;;;;;;;;;;;;;;;;;;;;;;;;;;;;;;;;;;;;;;;;;;;;;;;;;;;;;;;;;;;;;;;
;;;;;;;;;;;;;;;;;;;;;;;;;;;;;;;;;;;;;;;;;;;;;;;;;;;;;;;;;;;;;;;;;;;
;;;;                                                           ;;;;
;;;;  Configure sensor, read sensor, send data to display PIC  ;;;;
;;;;                                                           ;;;;
;;;;;;;;;;;;;;;;;;;;;;;;;;;;;;;;;;;;;;;;;;;;;;;;;;;;;;;;;;;;;;;;;;;
;;;;;;;;;;;;;;;;;;;;;;;;;;;;;;;;;;;;;;;;;;;;;;;;;;;;;;;;;;;;;;;;;;;

;-------------------;
; PIC configuration ;
;-------------------;

    __CONFIG 0x300001, B’00001001’    ; Bit0:4(1001 => internal f=8MHz clock, f/4 signal on RA6)
    __CONFIG 0x300002, B’00001101’    ; Bit2,3(1,1 => Brownout reset voltage -> 2V)
                                      ; Bit1(0 => Brownout reset -> disabled)
                                      ; Bit0(1 => Power up timer -> disabled)
    __CONFIG 0x300003, B’00011110’    ; Bit1:4(Watchdog timer config [not needed])
                                      ; Bit0(Watchdog timer -> disabled [no interrupts needed])
    __CONFIG 0x300005, B’00000001’    ; Bit7(0 => RE3 input pin enabled)
                                      ; Bit1(PORTB<4:0>, 0 => digital I/O on reset, 1 => analog I/O on reset)
                                      ; Bit0(CCP2 I/O multiplex: 1 => RC1, 0 => RB3)
    __CONFIG 0x300006, B’10000000’    ; Bit7(1 => Background debugger disabled [can use RB6 & RB7])
                                      ; Bit2(0 => disable low voltage ICSP)
                                      ; Bit0(0 => Stack full/underflow => no reset)
    __CONFIG 0x300008, B’00001111’    ; Bit3:0(1 => code protection -> off)
    __CONFIG 0x300009, B’11000000’    ; Bit7:6(1 => EEPROM code protection -> off)
    __CONFIG 0x30000A, B’00001111’    ; Bit3:0(1 => Write protection -> off)
    __CONFIG 0x30000B, B’11100000’    ; Bit7:5(1 => EEPROM write protection -> off)
    __CONFIG 0x30000C, B’00001111’    ; Bit3:0(1 => Table read protection -> off)
    __CONFIG 0x30000D, B’01000000’    ; Bit6(1 => Boot block table read protection -> off)

;----------------------------;
; Special function registers ;
;----------------------------;

A           EQU     0
PORTA       EQU     0x80            ; PORTA register
PORTB       EQU     0x81            ; PORTB register
PORTC       EQU     0x82            ; PORTC register
```

```
LATA        EQU     0x89            ; PORTA data latch register
LATB        EQU     0x8A            ; PORTB data latch register
LATC        EQU     0x8B            ; PORTC data latch register
TRISA       EQU     0x92            ; PORTA tri-state (I/O) register
TRISB       EQU     0x93            ; PORTB tri-state (I/O) register
TRISC       EQU     0x94            ; PORTC tri-state (I/O) register
FSR0        EQU     0x00            ; File select register (indirect addressing)
POSTINC0    EQU     0xEE            ; Increment FSR0 after indirect access
OSCCON      EQU     0xD3            ; Allows selection of internal oscillator block
ADCON0      EQU     0xC2            ; A/D converter control
ADCON1      EQU     0xC1            ;


;---------------;
; I2C registers ;
;---------------;

DSHIFT      EQU     0x6E            ; Data shift register
REGADDR     EQU     0x6D            ; Address of current imaging chip register
HIBYTE      EQU     0x6C            ; High byte of sensor register value
LOWBYTE     EQU     0x6B            ; Low byte of sensor register value
BITCNT      EQU     0x6A            ; Bit count (count sets of 8 bits)
BYTECNT     EQU     0x69            ; Byte count (count sets of 4 bytes)

;----------;
; Counters ;
;----------;

LINE        EQU     0x77            ; Display-line counter

TIME1       EQU     0x5C            ; Delay-time counters
TIME2       EQU     0x5B            ;
TIME3       EQU     0x5A            ;

;---------------;
; Program start ;
;---------------;

        ORG     0h                  ; Startup address = '0000'

        BSF     OSCCON, 4, A        ; Internal oscillator freq selector -> 8 MHz
        BSF     OSCCON, 5, A        ;
        BSF     OSCCON, 6, A        ;

        BCF     ADCON0, 0, A        ; Disable analog -> digital converter
        BSF     ADCON1, 0, A        ; Set all ports as digital I/O
        BSF     ADCON1, 1, A        ;
        BSF     ADCON1, 2, A        ;
        BSF     ADCON1, 3, A        ;

        CALL    LONGDELAY           ; Startup delay, allows signals to stablise

;------------------;
; Initialise PORTs ;
;------------------;

        CLRF    PORTA, A            ;
        CLRF    PORTB, A            ; Clear ports -> nothing floating
        CLRF    PORTC, A            ;

        MOVLW   B'00011010'         ; PORTA pins RA1,RA4 -> inputs, all others outputs
        MOVWF   TRISA, A            ; RA1 = data request signal
                                    ; RA3 = FRAME_VALID (unused), RA4 = monitor LINE_VALID from sensor
                                    ; RA0 = SCLK, RA5 = SDATA, RA2 = DataValid line
                                    ; RA6 = CLKO (sensor clock output)

        MOVLW   B'00000000'         ; PORTB pins -> outputs
        MOVWF   TRISB, A            ; Output data to DisplayPIC, bytewise
```

```
        MOVLW   B'11111111'         ; PORTC pins -> inputs
        MOVWF   TRISC, A            ; Input data from sensor, bytewise

;-----------------------;
; Configure imaging chip ;
;-----------------------;

        CALL    SHORTDELAY

        MOVLW   0x09                ; 'Rows of integration' register address = 0x09
        MOVWF   REGADDR, A
        MOVLW   0x00                ; high byte of 2 byte 'rows of integration' value
        MOVWF   HIBYTE, A
        MOVLW   0x0A                ; low byte of 2 byte 'rows of integration' value
        MOVWF   LOWBYTE, A

        CALL    I2C                 ; Call serial communication subroutine

        MOVLW   0x05                ; 'Horizontal blanking' register address = 0x05
        MOVWF   REGADDR, A
        MOVLW   0x00                ; high byte of 2 byte 'horizontal blanking' value
        MOVWF   HIBYTE, A
        MOVLW   0x00                ; low byte of 2 byte 'horizontal blanking' value
        MOVWF   LOWBYTE, A

        CALL    I2C                 ; Call serial communication subroutine

        MOVLW   0x06                ; 'Vertical blanking' register address = 0x06
        MOVWF   REGADDR, A
        MOVLW   0x00                ; high byte of 2 byte 'vertical blanking' value
        MOVWF   HIBYTE, A
        MOVLW   0x00                ; low byte of 2 byte 'vertical blanking' value
        MOVWF   LOWBYTE, A

        CALL    I2C                 ; Call serial communication subroutine

        MOVLW   0x03                ; 'Window height' register address = 0x03
        MOVWF   REGADDR, A
        MOVLW   0x00                ; high byte of 2 byte 'window height' value
        MOVWF   HIBYTE, A
        MOVLW   0x02                ; low byte of 2 byte 'window height' value (0x02 => 3 line window)
        MOVWF   LOWBYTE, A

        CALL    I2C                 ; Call serial communication subroutine

        MOVLW   0x01                ; 'Row start' register address = 0x01
        MOVWF   REGADDR, A
        MOVLW   0x01                ; high byte of 2 byte 'row start' value
        MOVWF   HIBYTE, A
        MOVLW   0xF4                ; low byte of 2 byte 'row start' value (0x01F4 => start on row 500)
        MOVWF   LOWBYTE, A

        CALL    I2C                 ; Call serial communication subroutine

;-------------------------;
; Acquire data from sensor ;
;-------------------------;

GETDATA MOVLW   D'240'              ; Set line-counter, 240 lines
        MOVWF   LINE, A
        LFSR    FSR0, 0x100         ; Initiate File Select Register 0 to address 0x100
LWAIT   BTFSC   PORTA, 4, A         ; Wait for LINE_VALID -> 0
        GOTO    LWAIT
HWAIT   BTFSS   PORTA, 4, A         ; Wait for LINE_VALID -> 1
        GOTO    HWAIT

LOOP    MOVF    PORTC, 0, A         ; Read byte of data from sensor
```

```
        MOVWF   POSTINC0, A         ; Store in register assigned by FSR0 then increment FSR0
        DECFSZ  LINE, 1, A          ; Count down lines
        GOTO    LOOP                ; NOTE: loop = 5 instr-cycles = 20 PICclk cycles = 5 snsrclk cycles
                                    ; => only read 1/5 pixels

;-------------------------;
; Send data to display PIC ;
;-------------------------;

START   LFSR    FSR0, 0x100         ; Initiate File Select Register 0 to address 0x100
        MOVLW   D'240'              ; Set line-counter, 240 lines
        MOVWF   LINE, A

REQWAIT BTFSS   PORTA, 1, A         ; Wait for data request from DisplayPIC
        GOTO    REQWAIT
        MOVF    POSTINC0, 0, A      ; Read byte of data
        MOVWF   PORTB, A            ; Output data to DisplayPIC
        BSF     PORTA, 2, A         ; DataValid line -> 1
CFMWAIT BTFSC   PORTA, 1, A         ; Wait for confirmation from DisplayPIC
        GOTO    CFMWAIT
        BCF     PORTA, 2, A         ; DataValid line -> 0
        DECFSZ  LINE, 1, A          ; If not finished sending data
        GOTO    REQWAIT             ;  loop around to send next byte

        GOTO    GETDATA             ; else acquire next frame from sensor

;----------------------------;
; I2C serial write subroutine ;
;----------------------------;

I2C     MOVLW   0xBA                ; 0xBA => serial write commencing
        MOVWF   DSHIFT, A           ; 0xBA -> data shift register

        MOVLW   D'4'
        MOVWF   BYTECNT, A          ; Byte count -> 4
        MOVLW   D'8'
        MOVWF   BITCNT, A           ; Bit count -> 8

        BSF     LATA, 5, A          ; SDATA -> 1  prepare for start bit
        BSF     LATA, 0, A          ; SCLK -> 1

STRTBIT BCF     LATA, 5, A          ; SDATA -> 0 (start bit = falling edge of SDATA while SCLK is high)
        CALL    VSDELAY             ; Very short delay
        BCF     LATA, 0, A          ; SCLK -> 0

SERIAL  BTFSS   DSHIFT, 7, A        ; if bit7 of DSHIFT == 0
        BCF     LATA, 5, A          ;  SDATA -> 0
        BTFSC   DSHIFT, 7, A        ; if bit7 of DSHIFT == 1
        BSF     LATA, 5, A          ;   SDATA -> 1

        BSF     LATA, 0, A          ; SCLK -> 1
        CALL    VSDELAY             ; Very short delay
        BCF     LATA, 0, A          ; SCLK -> 0

        RLNCF   DSHIFT, 1,A         ; Rotate left => ready to send next bit
        DECFSZ  BITCNT, 1, A        ; Count down until entire byte sent
        GOTO    SERIAL

        MOVLW   B'00100000'         ; listen for acknowledgement bit from SDATA
        IORWF   TRISA, 1, A         ; => RA5 -> input

        CALL    VSDELAY             ; Very short delay
        BSF     LATA, 0, A          ; SCLK -> 1
        BTFSC   PORTA, 5, A         ; Test for acknowledgement bit
        BRA     $-2                 ; Keep listening if necessary

        CALL    VSDELAY             ; Very short delay
        BCF     LATA, 0, A          ; SCLK -> 0
```

```
        MOVLW   B'11011111'         ; Stop listening for acknowledgement bit from SDATA
        ANDWF   TRISA, 1, A         ; => RA5 -> output

        MOVLW   D'8'
        MOVWF   BITCNT, A           ; Reset bit count

        DCFSNZ  BYTECNT, 1, A       ; if BYTECNT == 0
        GOTO    STOPBIT             ;   GOTO STOPBIT

        MOVLW   D'3'                ; if BYTECNT > 2 (inc. BYTECNT = 3)
        CPFSLT  BYTECNT, A          ;   GOTO reg. address
        GOTO    SETREG              ; end

        MOVLW   D'1'                ; if BYTECNT < 2 (inc. BYTECNT = 1)
        CPFSGT  BYTECNT, A          ;   GOTO low byte
        GOTO    SETLOW              ; end

        GOTO    SETHI               ; else GOTO high byte

;-------------------------------------------------------
SETREG  MOVF    REGADDR, 0, A
        MOVWF   DSHIFT, A           ; DSHIFT = REGADDR
        GOTO    SERIAL

SETHI   MOVF    HIBYTE, 0, A
        MOVWF   DSHIFT, A           ; DSHIFT = HIBYTE
        GOTO    SERIAL

SETLOW  MOVF    LOWBYTE, 0, A
        MOVWF   DSHIFT, A           ; DSHIFT = LOWBYTE
        GOTO    SERIAL
;-------------------------------------------------------

STOPBIT BCF     LATA, 5, A          ; Ensure SDATA is low prior to stop bit

        BSF     LATA, 0, A          ; SCLK -> 1 ready for stop bit
        CALL    VSDELAY
        BSF     LATA, 5, A          ; SDATA -> 1 (stop bit = rising edge of SDATA while SCLK is high)

        RETURN                      ; End subroutine

;-------------------------;
; Very short delay 10.5 us ;
;-------------------------;

VSDELAY     MOVLW   D'5'
            MOVWF   TIME1, A
VSDLOOP     DECFSZ  TIME1, 1, A
            GOTO    VSDLOOP
            RETURN

;-------------------------------;
; Short delay subroutine (~5 ms) ;
;-------------------------------;

SHORTDELAY  MOVLW   D'13'
            MOVWF   TIME1, A
SDLOOP1     MOVLW   D'255'
            MOVWF   TIME2, A
SDLOOP2     DECFSZ  TIME2, 1, A
            GOTO    SDLOOP2
            DECFSZ  TIME1, 1, A
            GOTO    SDLOOP1
            RETURN

;--------------------------------;
; Long delay subroutine (~0.978 s) ;
```

```
;---------------------------------;

LONGDELAY   MOVLW   D'10'
            MOVWF   TIME1, A
LDLOOP1     MOVLW   D'255'
            MOVWF   TIME2, A
LDLOOP2     MOVLW   D'255'
            MOVWF   TIME3, A
LDLOOP3     DECFSZ  TIME3, 1, A
            GOTO    LDLOOP3
            DECFSZ  TIME2, 1, A
            GOTO    LDLOOP2
            DECFSZ  TIME1, 1, A
            GOTO    LDLOOP1
            RETURN

        END                           ; End program
```

A.2 *DisplayPIC* code

```
;;;;;;;;;;;;;;;;;;;;;;;;;;;;;;;;;;;;;;;;;;;;;;;;;;;;;;;;
;;;;;;;;;;;;;;;;;;;;;;;;;;;;;;;;;;;;;;;;;;;;;;;;;;;;;;;;
;;;;                                                ;;;;
;;;;  Receive data from sensor PIC, display on LCD  ;;;;
;;;;                                                ;;;;
;;;;;;;;;;;;;;;;;;;;;;;;;;;;;;;;;;;;;;;;;;;;;;;;;;;;;;;;
;;;;;;;;;;;;;;;;;;;;;;;;;;;;;;;;;;;;;;;;;;;;;;;;;;;;;;;;

;-------------------;
; PIC configuration ;
;-------------------;

    __CONFIG 0x300001, B'00000110'  ; Bit0:4(0110 => high speed crystal osc. with phase locked loop)
    __CONFIG 0x300002, B'00001101'  ; Bit2,3(1,1 => Brownout reset voltage -> 2V)
                                    ; Bit1(0 => Brownout reset -> disabled)
                                    ; Bit0(1 => Power up timer -> disabled)
    __CONFIG 0x300003, B'00011110'  ; Bit1:4(Watchdog timer config [not needed])
                                    ; Bit0(Watchdog timer -> disabled [no interrupts needed])
    __CONFIG 0x300005, B'00000001'  ; Bit7(0 => RE3 input pin enabled)
                                    ; Bit1(PORTB<4:0>, 0 => digital I/O on reset, 1 => analog I/O on reset)
                                    ; Bit0(CCP2 I/O multiplex: 1 => RC1, 0 => RB3)
    __CONFIG 0x300006, B'10000000'  ; Bit7(1 => Background debugger disabled [can use RB6 & RB7])
                                    ; Bit2(0 => disable low voltage ICSP)
                                    ; Bit0(0 => Stack full/underflow => no reset)
    __CONFIG 0x300008, B'00001111'  ; Bit3:0(1 => code protection -> off)
    __CONFIG 0x300009, B'11000000'  ; Bit7:6(1 => EEPROM code protection -> off)
    __CONFIG 0x30000A, B'00001111'  ; Bit3:0(1 => Write protection -> off)
    __CONFIG 0x30000B, B'11100000'  ; Bit7:5(1 => EEPROM write protection -> off)
    __CONFIG 0x30000C, B'00001111'  ; Bit3:0(1 => Table read protection -> off)
    __CONFIG 0x30000D, B'01000000'  ; Bit6(1 => Boot block table read protection -> off)

;----------------------------;
; Special function registers ;
;----------------------------;

A           EQU     0
PORTA       EQU     0x80            ; PORTA register
PORTB       EQU     0x81            ; PORTB register
PORTC       EQU     0x82            ; PORTC register
LATA        EQU     0x89            ; PORTA data latch register
LATB        EQU     0x8A            ; PORTB data latch register
LATC        EQU     0x8B            ; PORTC data latch register
TRISA       EQU     0x92            ; PORTA tri-state (I/O) register
TRISB       EQU     0x93            ; PORTB tri-state (I/O) register
TRISC       EQU     0x94            ; PORTC tri-state (I/O) register
FSR0        EQU     0x00            ; File select register (indirect addressing)
POSTINC0    EQU     0xEE            ; Increment FSR0 after indirect access
POSTDEC0    EQU     0xED            ; Decrement FSR0 after indirect access
ADCON0      EQU     0xC2            ; A/D converter control
ADCON1      EQU     0xC1            ;
T1CON       EQU     0xCD            ; Timer 1 control
BLK         EQU     0x7A            ; Block counter 1 (block = 4 display pixels)
BLK2        EQU     0x79            ; Block counter 2 (block = 4 display pixels)
BLK3        EQU     0x78            ; Block counter 3 (block = 4 display pixels)
LINE        EQU     0x77            ; Line number on display

CYCDL       EQU     0x76            ; Cyclic delay counter
SLOW        EQU     0x74            ; Counters used to slow down cycling delay
SLOW2       EQU     0x73            ;
MIN         EQU     0x70            ; Stores current minimum intensity value
MAX         EQU     0x6F            ; Stores current maximum intensity value
FCOUNT      EQU     0x6E            ; Frame counter

TIME1       EQU     0x5C            ; Counters for delay subroutines
TIME2       EQU     0x5B            ;
TIME3       EQU     0x5A            ;
```

```
;---------------;
; Program start ;
;---------------;

        ORG     0h                  ; Startup address = '0000'

        CLRF    CYCDL, A            ; Initialize cyclic delay counter = 0
        CLRF    SLOW, A
        CLRF    SLOW2, A

BCF     ADCON0, 0, A        ; Disable analog -> digital converter
        BSF     ADCON1, 0, A        ; Set all ports as digital I/O
        BSF     ADCON1, 1, A        ;
        BSF     ADCON1, 2, A        ;
        BSF     ADCON1, 3, A        ;

        BCF     T1CON, 0, A         ; Disable TIMER1 secondary clock source

;-------------------------------------------;
; Startup delay, allows signals to stablise ;
;-------------------------------------------;

CALL    LONGDELAY

;------------------;
; Initialise PORTs ;
;------------------;

        CLRF    PORTA, A            ;
        CLRF    PORTB, A            ; Clear ports -> nothing floating
        CLRF    PORTC, A            ;

        MOVLW   B'00001100'         ; PORTA pins 2,3 -> inputs, all others outputs
        MOVWF   TRISA, A            ; RA2 = DataValid signal from sensor PIC, RA3 = cyclic delay enable
                                    ; RA0 = LCD Drive, RA1 = Data request line, RA<6:7> = Crystal osc.
        MOVLW   B'00000000'         ; PORTB pins -> outputs
        MOVWF   TRISB, A            ; Output data to display, RB<0:3> = data bus, RB4 = /DISPOFF...
                                    ; ... RB5 = CP, RB6 = LP, RB7 = FLM
        MOVLW   B'11111111'         ; PORTC pins -> inputs
        MOVWF   TRISC, A            ; Input data from SensorPIC, bytewise

;------------------------------;
; Receive data from sensor PIC ;
;------------------------------;

GETDATA MOVLW   D'10'           ; Set frame counter = 10
        MOVWF   FCOUNT, A       ;
        LFSR    FSR0, 0x100     ; Initiate File Select Register 0 to address 0x100
        BSF     PORTA, 1, A     ; Request data
FVLWAIT BTFSS   PORTA, 2, A     ; Wait for data to be valid (First VaLid WAIT)
        GOTO    FVLWAIT
        MOVF    PORTC, 0, A     ; Read data from sensor PIC into WREG
        MOVWF   POSTINC0, A     ; Shift data from WREG into first indirect addressing register...
                                ; and increment FSR0
                                ; Point off left side of screen, value written to avoid long...
                                ; marker on first line
        MOVWF   POSTINC0, A     ; Shift data from WREG into second indirect addressing register...
                                ; and increment FSR0
        BCF     PORTA, 1, A     ; Indicate data received
FNVWAIT BTFSC   PORTA, 2, A     ; Wait for data valid line to go low (First Not Valid WAIT)
        GOTO    FNVWAIT

        MOVLW   D'239'          ; Set line-counter, 239 lines (last line is blank and separate...
                                ; to merge with FLM)
        MOVWF   LINE, A

DATLOOP BSF     PORTA, 1, A     ; Request data
```

```
VALWAIT BTFSS   PORTA, 2, A     ; Wait for data to be valid (VALid WAIT)
        GOTO    VALWAIT
        MOVF    PORTC, 0, A     ; Read data from sensor PIC into WREG
        MOVWF   POSTINC0, A     ; Shift data from WREG into next indirect addressing register...
                                ; and increment FSR0
        BCF     PORTA, 1, A     ; Indicate data received
NVLWAIT BTFSC   PORTA, 2, A     ; Wait for data valid line to go low (Not VaLid WAIT)
        GOTO    NVLWAIT
        DECFSZ  LINE, 1, A      ; Decrement line counter, if last line reached begin display
        GOTO    DATLOOP         ; else acquire more data

        MOVWF   INDF0, A        ; Point off right side of screen, value written to avoid...
                                ; long marker on last line

;--------------;
; Display data ;
;--------------;

;------------------;
; Blank first line ;
;------------------;

        BSF     LATA, 0, A          ; LCD Drive voltage on (1.7V)

START   LFSR    FSR0, 0x100         ; Initiate File Select Register 0 to address 0x100
        MOVLW   D'239'              ; Set line-counter, 239 lines (last line is blank and separate...
                                    ; to merge with FLM)
        MOVWF   LINE, A

        MOVLW   D'79'               ; 80 blocks (1 outside loop) * 4 segments
        MOVWF   BLK, A              ; => 320 segments in line

        BCF     LATB, 7, A          ; /DISPOFF -> 0
        BSF     LATB, 5, A          ; LP -> 1
        BCF     LATB, 6, A          ; CP -> 0
        BSF     LATB, 7, A          ; /DISPOFF -> 1
        BSF     LATB, 6, A          ; CP -> 1

        BCF     LATB, 0, A          ; Ensure D<0:3> = 0
        BCF     LATB, 1, A          ;
        BCF     LATB, 2, A          ;
        BCF     LATB, 3, A          ;

        BSF     LATB, 4, A          ; FLM -> 1
        BCF     LATB, 5, A          ; LP -> 0

LINE1   BCF     LATB, 6, A          ; First line is blank
        BSF     LATB, 6, A          ;
        DECFSZ  BLK, 1, A           ;
        GOTO    LINE1               ;

        BSF     LATB, 5, A          ; LP -> 1
        BCF     LATB, 6, A          ; CP -> 0
        BSF     LATB, 6, A          ; CP -> 1
        BCF     LATB, 4, A          ; FLM -> 0
        BCF     LATB, 5, A          ; LP -> 0

        DECF    LINE, 1, A          ; Decrement line-counter

;-----------------------------------;
; Calculate marker size and position ;
;-----------------------------------;

CRVCALC MOVF    POSTINC0, 0, A      ; Read data from location(X-1) into WREG and increment FSR0
        MOVWF   MIN, A              ; Shift data from WREG into MIN
        MOVF    POSTINC0, 0, A      ; Read data from location(X) into WREG and increment FSR0
        CPFSLT  MIN, A              ; if MIN < value(X), then value(X-1) remains MIN
        MOVWF   MIN, A              ; else shift value(X) into MIN
```

```
        MOVWF   MAX, A              ; Shift value(X) into MAX
        MOVF    POSTDEC0, 0, A      ; Read data from location X+1 into WREG and decrement FSR0
        CPFSLT  MIN, A              ; if MIN < value(X+1), then MIN is unchanged
        MOVWF   MIN, A              ; else shift value(X+1) into MIN

        MOVF    MIN, 0, A           ; Shift value(MIN) into WREG
        CPFSGT  MAX, A              ; if MAX > WREG, then increment value(MIN) by 1
        GOTO    NODIAG              ; else GOTO NODIAG
        INCF    MIN, 1, A           ;

NODIAG  MOVF    MIN, 0, A           ; Shift value(MIN)...
        MOVWF   BLK, A              ; ...into BLK
        RRNCF   BLK, 1, A           ; Divide by four (round down), writing in blocks of 4 pixels
        RRNCF   BLK, 1, A           ;
        BCF     BLK, 7, A           ;
        BCF     BLK, 6, A           ; => BLK = number of blocks to minimum of current and adjacent rows

        MOVF    MAX, 0, A           ; Shift value(MAX)...
        MOVWF   BLK2, A             ; ...into BLK2
        RRNCF   BLK2, 1, A          ; Divide by four (round down), writing in blocks of 4 pixels
        RRNCF   BLK2, 1, A          ;
        BCF     BLK2, 7, A          ;
        BCF     BLK2, 6, A          ; => BLK2 = number of blocks to max of current and adjacent rows

        MOVLW   D'78'               ; Preload BLK3 with 78 (80 blocks total, 78 either light or dark,...
        MOVWF   BLK3, A             ; ...2 possible partially lit blocks at top and bottom of marker)
        MOVF    BLK2, 0, A          ; Subtract value(MAX)/4 from BLK3
        SUBWF   BLK3, 1, A          ; => BLK3 = num of blocks between current intensity, and end of row

        MOVF    BLK, 0, A           ; Subtract BLK from BLK2
        SUBWF   BLK2, 1, A          ; => BLK2 = number of blocks between current intensity value...
        INCF    BLK2, 1, A          ; ...and min of current and adjacent values

        MOVF    BLK, 0, A

;-------------------------------;
; Test for delay increase signal ;
;-------------------------------;

        BTFSS   PORTA 3, A
        CALL    KEEPDEL
        BTFSC   PORTA, 3, A
        CALL    CYCLICDELAY

;---------------------------;
; Address pixels under curve ;
;---------------------------;

NORM    BSF     LATB, 0, A          ; Ensure D<0:3> = 1
        BSF     LATB, 1, A          ;
        BSF     LATB, 2, A          ;
        BSF     LATB, 3, A          ;

        TSTFSZ  BLK, A              ; Avoid decrement to 255 on zero value
        GOTO    BLANK1B
        GOTO    SKIP1B
BLANK1B BCF     LATB, 6, A          ; value(BLK) number of display clock cycles
        BSF     LATB, 6, A          ;
        DECFSZ  BLK, 1, A           ;
        GOTO    BLANK1B             ;

SKIP1B  BCF     MIN, 7, A           ; MIN -> (MIN mod 4)
        BCF     MIN, 6, A           ; Determine number of bright pixels in first block of marker
        BCF     MIN, 5, A           ;
        BCF     MIN, 4, A           ;
        BCF     MIN, 3, A           ;
        BCF     MIN, 2, A           ;
        DECF    MIN, 1, A           ; Decrement MIN four times
```

```
        DECF    MIN, 1, A           ; => can count *up* to zero
        DECF    MIN, 1, A           ;
        DECF    MIN, 1, A           ;
        BCF     MAX, 7, A           ; MAX -> (MAX mod 4)
        BCF     MAX, 6, A           ; Determine number of dark pixels in last block of marker
        BCF     MAX, 5, A           ;
        BCF     MAX, 4, A           ;
        BCF     MAX, 3, A           ;
        BCF     MAX, 2, A           ;
        DECF    MAX, 1, A           ; Decrement MAX four times
        DECF    MAX, 1, A           ; => can count *up* to zero
        DECF    MAX, 1, A           ;
        DECF    MAX, 1, A           ;

;--------------------------------------;
; Find where in a block the mark begins ;
;--------------------------------------;

        BCF     LATB, 0, A          ; D0 -> 0
        INFSNZ  MIN, 1, A           ; Increment MIN, if MIN cycles to zero...
        GOTO    MARK                ; ...then goto MARK
        BCF     LATB, 1, A          ; D1 -> 0
        INFSNZ  MIN, 1, A           ; Increment MIN, if MIN cycles to zero...
        GOTO    MARK                ; ...then goto MARK
        BCF     LATB, 2, A          ; D2 -> 0
        INFSNZ  MIN, 1, A           ; Increment MIN, if MIN cycles to zero...
        GOTO    MARK                ; ...then goto MARK
        BCF     LATB, 3, A          ; D3 -> 0

;---------------------;
; Place marker on line ;
;---------------------;

MARK    MOVLW D'1'
        CPFSEQ  BLK2, A
        GOTO    MID
        INFSNZ  MAX, 1, A
        GOTO    MID
        BSF     LATB, 0, A
        INFSNZ  MAX, 1, A
        GOTO    MID
        BSF     LATB, 1, A
        INFSNZ  MAX, 1, A
        GOTO    MID
        BSF     LATB, 2, A

MID     BCF     LATB, 6, A          ; CP -> 0
        BSF     LATB, 6, A          ; CP -> 1
        BCF     LATB, 3, A          ; D<0:3> -> 1
        BCF     LATB, 2, A          ;
        BCF     LATB, 1, A          ;
        BCF     LATB, 0, A          ;
        DECFSZ  BLK2, 1, A
        GOTO    MARK

        BSF     LATB, 0, A          ; Ensure D<0:3> = 1
        BSF     LATB, 1, A          ;
        BSF     LATB, 2, A          ;
        BSF     LATB, 3, A          ;


        TSTFSZ  BLK3, A             ; Avoid decrement to 255 on zero value
        GOTO    BLANK1C
        GOTO    SKIP1C
BLANK1C BCF     LATB, 6, A          ; Following BLK2 blocks are blue (D=0)
        BSF     LATB, 6, A          ;
        DECFSZ  BLK3, 1, A          ;
        GOTO    BLANK1C             ;
```

```
SKIP1C  BSF     LATB, 5, A          ; LP -> 1
        BCF     LATB, 6, A          ; CP -> 0
        BSF     LATB, 6, A          ; CP -> 1
        BCF     LATB, 5, A          ; LP -> 0

        DECFSZ  LINE, 1, A          ; Move on to next line
        GOTO    CRVCALC

        MOVLW   D'79'               ; 80 blocks (1 outside loop) * 4 segments
        MOVWF   BLK, A              ; => 320 segments in line
        BCF     LATB, 0, A          ; Ensure D<0:3> = 0
        BCF     LATB, 1, A          ;
        BCF     LATB, 2, A          ;
        BCF     LATB, 3, A          ;


BLANK1D BCF     LATB, 6, A          ; Last line is blank
        BSF     LATB, 6, A          ;
        DECFSZ  BLK, 1, A           ;
        GOTO    BLANK1D             ;

        DECFSZ  FCOUNT, 1, A        ; Decrement FrameCount, if FrameCount /= 0
        GOTO    START               ;   then repeat frame
        GOTO    GETDATA             ; else acquire new frame of data from SensorPIC

;------------------------;
; Cyclic delay subroutine ;
;------------------------;

CYCLICDELAY INCFSZ  SLOW, 1, A       ; Increment SLOW, if cycle from 0xFF to 0x00 skip an instruction
            GOTO    POSTINC
            INCF    SLOW2, 1, A      ; Increment SLOW2
            BTFSS   SLOW2, 1, A      ; if SLOW2 == 2, skip next instruction
            GOTO    POSTINC
            CLRF    SLOW2, A         ; Set SLOW2 = 0
            CLRF    SLOW, A          ; Set SLOW = 0
            INCF    CYCDL, 1, A     ; Increment CYCDL
            MOVLW   D'255'
            CPFSGT  CYCDL, A
            GOTO    POSTINC
            MOVLW   D'1'
            MOVWF   CYCDL, A
POSTINC     INCF    CYCDL, 1, A     ; if CYCDL == 0
            DCFSNZ  CYCDL, 1, A     ;
            INCF    CYCDL, 1, A     ;   then increment CYCDL
            MOVF    CYCDL, 0, A     ; Shift CYCDL...
            MOVWF   TIME1, A        ; ...into TIME1
MDLOOP1     NOP                     ; Delay-loop, count down from CYCDL to zero
            NOP
            NOP
            DECFSZ  TIME1, 1, A
            GOTO    MDLOOP1
            RETURN


KEEPDEL     INCF    CYCDL, 1, A     ; if CYCDL == 0
            DCFSNZ  CYCDL, 1, A     ;
            INCF    CYCDL, 1, A     ;   then increment CYCDL
            MOVF    CYCDL, 0, A     ; Shift CYCDL...
            MOVWF   TIME1, A        ; ...into TIME1
MDLOOP2     NOP                     ; Delay-loop, count down from CYCDL to zero
            NOP
            NOP
            DECFSZ  TIME1, 1, A
            GOTO    MDLOOP2
            RETURN
```

```
;----------------------------------;
; Long delay subroutine (~0.978 s) ;
;----------------------------------;

LONGDELAY   MOVLW   D'10'
            MOVWF   TIME1, A
LDLOOP1     MOVLW   D'255'
            MOVWF   TIME2, A
LDLOOP2     MOVLW   D'255'
            MOVWF   TIME3, A
LDLOOP3     DECFSZ  TIME3, 1, A
            GOTO    LDLOOP3
            DECFSZ  TIME2, 1, A
            GOTO    LDLOOP2
            DECFSZ  TIME1, 1, A
            GOTO    LDLOOP1
            RETURN

END
```

Appendix B

Deriving the Hamiltonian for the Time-Dependent Adiabatic State

We start with the time-dependent Schrödinger equation for the diabatic state

$$i\hbar\frac{d}{dt}|\psi\rangle = \underline{\underline{H}}|\psi\rangle \tag{B.1}$$

The adiabatic state is given by the unitary transformation

$$|\phi\rangle = \underline{\underline{U}}|\psi\rangle \tag{B.2}$$

Which allows us to make the substitution for the diabatic state

$$|\psi\rangle = \underline{\underline{U}}^{-1}|\phi\rangle \tag{B.3}$$

$$\Rightarrow i\hbar\frac{d}{dt}\left(\underline{\underline{U}}|\phi\rangle\right) = \underline{\underline{H}}\underline{\underline{U}}|\phi\rangle \tag{B.4}$$

$$\Rightarrow i\hbar\left\{\left(\frac{d}{dt}\underline{\underline{U}}\right)|\phi\rangle + \underline{\underline{U}}\frac{d|\phi\rangle}{dt}\right\} = \underline{\underline{H}}\underline{\underline{U}}|\phi\rangle \tag{B.5}$$

The time-dependent Schrödinger equation for the adiabatic state is given by

$$i\hbar\frac{d}{dt}|\phi\rangle = \underline{\underline{H}}_A|\phi\rangle \tag{B.6}$$

$$\Rightarrow \frac{d}{dt}|\phi\rangle = \frac{1}{i\hbar}\underline{\underline{H}}_A|\phi\rangle \tag{B.7}$$

Substituting this into equation B.5 gives

$$i\hbar\left(\frac{d}{dt}\underline{\underline{U}}\right)|\phi\rangle + \underline{\underline{U}}\,\underline{\underline{H}}_A|\phi\rangle = \underline{\underline{H}}\,\underline{\underline{U}}|\phi\rangle \tag{B.8}$$

Multiplying both sides by $\underline{\underline{U}}^{-1}$ and rearranging in terms of $\underline{\underline{H}}_A$ gives

$$\underline{\underline{H}}_A|\phi\rangle = \left(\underline{\underline{U}}^{-1}\underline{\underline{H}}\,\underline{\underline{U}} - i\hbar\underline{\underline{U}}^{-1}\frac{d}{dt}\underline{\underline{U}}\right)|\phi\rangle \tag{B.9}$$

which is the Hamiltonian for the time–dependent adiabatic state

$$\underline{\underline{H}}_A = \underline{\underline{U}}^{-1}\underline{\underline{H}}\,\underline{\underline{U}} - i\hbar\underline{\underline{U}}^{-1}\frac{d}{dt}\underline{\underline{U}} \tag{B.10}$$

Appendix C

Adiabatic Theorem MATLAB Code

C.1 Analyzing the effect of differing field profiles

```
clear; clc; clf;
%%%%%%%%%%%%%%%%%%%%%%%%%%%%%%%%%%%%%%%%%%%%%%%%%%%%%%%%%%%%%%%%%%%%%%%%
% Solving the amplitude equations quantum system near a curve crossing %
%                      for different field profiles                    %
%%%%%%%%%%%%%%%%%%%%%%%%%%%%%%%%%%%%%%%%%%%%%%%%%%%%%%%%%%%%%%%%%%%%%%%%

nosteps = 4001;      % Number of time-steps
N = (nosteps - 1)/2; % Time runs from -tmax -> tmax
tmax = 4;
dt = tmax/N;         % Stepsize

a = 1;               % Coupling between diabatic states
hbar = 1;

t(1) = -tmax;        % Initial time
cA1(1) = sqrt(1);    % Initial amplitude of adiabatic state 1
cA2(1) = sqrt(0);    % Initial amplitude of adiabatic state 2
E0(1) = 0;           % Initial value of ea0.dF/dt
E0max = 30;          % Maximum value of ea0.dF/dt
Fmax = E0max/2*(2*tmax + dt); % Maximum electric field
F(1) = -Fmax/2;               % Initial electric field
epsilon(1) = sqrt(E0max/2^2*t(1)^2 + a^2); % Initial adiabatic state energy
w0 = 2*epsilon(1)/hbar;       % Initial frequency splitting

figure(1)            % Create figure
for q = 1:3

    for n = 2:nosteps

        t(n) = t(n-1) + dt; % Time

        if q == 1 % Linear field ramp

            F(n) = F(n-1) + E0max/2*dt;

        elseif q == 2 % sin^2 field ramp

            F(n) = Fmax*sin(pi/(4*tmax)*(t(n) + tmax))^2 - Fmax/2;
```

```
        elseif q == 3

            if t(n) < 0 % First sin^2 field ramp
                F(n) = Fmax/2*sin(pi/(2*tmax)*(t(n) + tmax))^2 - Fmax/2;
            else        % Second sin^2 field ramp
                F(n) = Fmax/2*sin(pi/(2*tmax)*t(n))^2 + Fmax/2 - Fmax/2;
            end

        end

        E0(n) = (F(n) - F(n-1))/dt;             % Field gradiant

        epsilon(n) = sqrt(F(n)^2 + a^2);        % Adiabatic state energy

        gamma(n) = a*E0max/2/(2*epsilon(n)^2); % Coupling between adiabatic states

        % 4th order Runge-Kutta solution algorithm
        p1 = i*epsilon(n-1)*cA1(n-1) - gamma(n-1)*cA2(n-1);
        q1 = gamma(n-1)*cA1(n-1) - i*epsilon(n-1)*cA2(n-1);

        p2 = i*epsilon(n-1)*(cA1(n-1) + dt/2*p1) - gamma(n-1)*(cA2(n-1) + dt/2*q1);
        q2 = gamma(n-1)*(cA1(n-1) + dt/2*p1) - i*epsilon(n-1)*(cA2(n-1) + dt/2*q1);

        p3 = i*epsilon(n-1)*(cA1(n-1) + dt/2*p2) - gamma(n-1)*(cA2(n-1) + dt/2*q2);
        q3 = gamma(n-1)*(cA1(n-1) + dt/2*p2) - i*epsilon(n-1)*(cA2(n-1) + dt/2*q2);

        p4 = i*epsilon(n-1)*(cA1(n-1) + dt*p3) - gamma(n-1)*(cA2(n-1) + dt*q3);
        q4 = gamma(n-1)*(cA1(n-1) + dt*p3) - i*epsilon(n-1)*(cA2(n-1) + dt*q3);

        cA1(n) = cA1(n-1) + dt/6*(p1 + 2*p2 + 2*p3 + p4);
        cA2(n) = cA2(n-1) + dt/6*(q1 + 2*q2 + 2*q3 + q4);

    end
    subplot(3,3,q);plot(t,F,'k-','linewidth',2)
    axis([-tmax tmax -Fmax/2 Fmax/2])
    if q == 1
        ylabel('Field strength','fontsize',16)
        title('(a)','fontsize',16)
    elseif q == 2
        title('(b)','fontsize',16)
    else
        title('(c)','fontsize',16)
    end
    subplot(3,3,q+3);plot(t(2:n),-epsilon(2:n),'r-',t(2:n),epsilon(2:n),'b-','linewidth',2)
    axis([-tmax tmax -70 70])
    if q == 1
        ylabel('Energy','fontsize',16)
    end
    subplot(3,3,q+6);plot(t,cA1.*conj(cA1),'r-',t,cA2.*conj(cA2),'b-','linewidth',2)
    text(-3.6,0.45,sprintf('P_{diabatic} = %1.2f',cA2(n)*conj(cA2(n))))
    if q == 1
        xlabel('Time','fontsize',16)
        ylabel('Populations','fontsize',16)
    else
        xlabel('Time','fontsize',16)
    end
end
```

C.2 Comparing numerical results with calculations using the Landau–Zener formula

```
clear; clc; clf;
%%%%%%%%%%%%%%%%%%%%%%%%%%%%%%%%%%%%%%%%%%%%%%%%%%%%%%%%%%%%%%%%%%%%%%%%%
% Solving the amplitude equations quantum system near a curve crossing %
%       comparison of numerical results with Landau-Zener              %
%%%%%%%%%%%%%%%%%%%%%%%%%%%%%%%%%%%%%%%%%%%%%%%%%%%%%%%%%%%%%%%%%%%%%%%%%

nosteps = 4001;      % Number of time-steps
N = (nosteps - 1)/2; % Time runs from -tmax -> tmax
tmax = 4;
dt = tmax/N;         % Stepsize

num = 20;            % Number of values of ea0.dF/dt
E0min = 1;           % Minimum value of ea0.dF/dt
E0max = 30;          % Maximum value of ea0.dF/dt

a = 1;               % Coupling between diabatic states
hbar = 1;

t(1) = -tmax;        % Initial time
cA1(1) = sqrt(1);    % Initial amplitude of adiabatic state 1
cA2(1) = sqrt(0);    % Initial amplitude of adiabatic state 1

for q = 1:num

    E0(q) = E0min + (q-1)*(E0max - E0min)/num;   % Electric field gradient
    epsilon(1) = sqrt(E0(q)^2*t(1)^2 + a^2); % Initial adiabatic energy

    for n = 2:nosteps

        t(n) = t(n-1) + dt;                      % Time
        F(q,n) = E0(q)*(t(n) + tmax + dt);       % Electric field strength
        epsilon(n) = sqrt(E0(q)^2*t(n)^2 + a^2); % Adiabatic state energy
        gamma(n) = a*E0(q)/2/epsilon(n)^2;       % Coupling between adiabatic states

        % 4th order Runge-Kutta solution algorithm
        p1 = i*epsilon(n-1)*cA1(n-1) - gamma(n-1)*cA2(n-1);
        q1 = gamma(n-1)*cA1(n-1) - i*epsilon(n-1)*cA2(n-1);

        p2 = i*epsilon(n-1)*(cA1(n-1) + dt/2*p1) - gamma(n-1)*(cA2(n-1) + dt/2*q1);
        q2 = gamma(n-1)*(cA1(n-1) + dt/2*p1) - i*epsilon(n-1)*(cA2(n-1) + dt/2*q1);

        p3 = i*epsilon(n-1)*(cA1(n-1) + dt/2*p2) - gamma(n-1)*(cA2(n-1) + dt/2*q2);
        q3 = gamma(n-1)*(cA1(n-1) + dt/2*p2) - i*epsilon(n-1)*(cA2(n-1) + dt/2*q2);

        p4 = i*epsilon(n-1)*(cA1(n-1) + dt*p3) - gamma(n-1)*(cA2(n-1) + dt*q3);
        q4 = gamma(n-1)*(cA1(n-1) + dt*p3) - i*epsilon(n-1)*(cA2(n-1) + dt*q3);

        cA1(n) = cA1(n-1) + dt/6*(p1 + 2*p2 + 2*p3 + p4);
        cA2(n) = cA2(n-1) + dt/6*(q1 + 2*q2 + 2*q3 + q4);

    end

    if q == 5
        figure(1) % Plot adiabatic state populations
        axes('fontsize',20)
        plot(t,cA1.*conj(cA1),'r-',t,cA2.*conj(cA2),'b-','linewidth',2)
        legend('\rho^A_{11}(t)','\rho^A_{22}(t)')
        xlabel('Time')

        figure(2) % Plot adiabatic state energies
        axes('fontsize',20)
        plot(t,-epsilon,'r-',t,epsilon,'b-','linewidth',2)
        legend('{\it\epsilon_1}','{\it\epsilon_2}')
```

```
        xlabel('Time')
        ylabel('Energy')
    end
    % Numerical solution for probability of a diabatic transition
    nonadiabaticpop(q) = cA2(n)*conj(cA2(n));
    % Landau-Zener value for probability of a diabatic transition (shifted)
    PLZ(q) = exp(-2*pi*a^2/(hbar*2*(E0(q) - 0.005))) - 0.005;

end

figure(3) % Compare numerical results with Landau-Zener
axes('fontsize',16)
plot(E0,nonadiabaticpop,'b-',E0,PLZ,'r-','linewidth',2)
legend('Numerical calculation','Landau-Zener (shifted by 0.005 {\itx} and {\it-y})')
xlabel('Field gradient','fontsize',20)
ylabel('Diabatic transition probability','fontsize',20)
```

Appendix D

MATLAB Simulation of Population Dynamics in a 4–Level System

```
clear; clc; clf;
%%%%%%%%%%%%%%%%%%%%%%%%%%%%%%%%%%%%%%%%%%%%%%%%%%%%%%%%%%%%%%%%%%%
%%    Population dynamics of a 4-level 'double lambda' system    %%
%%  4 light fields with variable frequency, intensity and phase  %%
%%%%%%%%%%%%%%%%%%%%%%%%%%%%%%%%%%%%%%%%%%%%%%%%%%%%%%%%%%%%%%%%%%%

e = 1.6e-19; hbar = 1.05e-34; c = 3e8; % Fundamental constants
a0 = 0.5292e-10; ep0 = 8.85e-12;

h0 = 2e-10;                   % Stepsize
notimesteps = 25000;          % Number of timesteps
tmax = 2e-6;                  % Simulation running time
tcoll = 0.5e-6;               % Interval between collisions
dephase = 0;                  % 1 = collisions on
numden = 1e19;                % Atomic number density

% Level frequencies
% (define |1> as zero)
lev(1) = 0;
lev(2) = 2*pi*806e6;
lev(3) = 2*pi*446810e9;
lev(4) = 2*pi*446810.094e9;

% Frequency splittings
w = zeros(4,4);
for k = 1:4
    for l = 1:4
        w(k,l) = lev(k) - lev(l);
    end
end

% 4 Laser frequencies
wL = zeros(4,4);
wL(1,3) = w(3,1);
wL(2,3) = w(3,2);
wL(1,4) = w(4,1);
wL(2,4) = w(4,2);

% Detunings
Delta = zeros(4,4);
for k = 1:4
    for l = 1:4
```

```
        for m = 1:4
            for n = 1:4
                Delta(k,l,m,n) = wL(k,l) - w(m,n);
            end
        end
    end
end

% Initial phases of light fields
phi13 = 0;
phi14 = 0;
phi23 = 0;
phi24 = 0;

% Relaxation rates of states |3> and |4>
Gamma3 = 1e7;
Gamma4 = 1e8;

% Electric field amplitude of light fields
E = zeros(4,4);
E(1,3) = 1000;
E(2,3) = 1000;
E(1,4) = 0;
E(2,4) = 0;

% Initial transition dipole moments
D = zeros(4,4);
r = 0;
for k = 2:4
    r = r + 1;
    for l = 1:r
        D(k,l) = -e*a0;
        D(l,k) = conj(D(k,l));
    end
end

d(:,:) = D(:,:);

% Initial Rabi frequencies
for k = 1:4
    for l = 1:4
        for m = 1:4
            for n = 1:4
                Chi(k,l,m,n) = -D(k,l)*E(m,n)/hbar;
            end
        end
    end
end

Chi(4,2,2,3) = -Chi(3,2,2,3);

% Define solution matrix
v = zeros(notimesteps,6);

% Initial amplitudes
v(1,2) = 1;
v(1,3) = 0;
%v(1,4) = 1/sqrt(2);
%v(1,5) = 1/sqrt(2);
v(1,6) = 1;

% Initial absorption coefficient
Kappa(1) = (wL(1,3)/c)*2*numden/(ep0*E(1,3))*imag(v(1,2)*conj(v(1,4))*D(3,1));

% Baseline for measuring collision interval
T = 0;
for n = 2:notimesteps
```

```
    % Time
    v(n,1) = v(n-1,1) + h0;

    % t = tmax -> end simulation
    if v(n,1) > tmax
        fprintf(1,'t > tmax')
        break
    end

    % Collisional dephasing
    if dephase == 1
        if v(n,1) > T + tcoll

            fprintf(1,'Collision, t = %1.2f us\n',1e6*v(n,1))
            T = T + tcoll;

            % Dephase transition dipole moments, d(i,j) = d(j,i)^*
            R = rand(4,1);
            r = 0;
            for k = 2:4
                r = r + 1;
                for l = 1:r
                    d(k,l) = D(k,l)*exp(i*2*pi*(R(l) - R(k)));
                    d(l,k) = conj(d(k,l));
                end
            end

            % Re-define Rabi frequencies
            for k = 1:4
             for l = 1:4
         for m = 1:2
              for p = 3:4
                 Chi(k,l,m,p) = -d(k,l)*E(m,p)/hbar;
                        end
                    end
                end
            end

        end
    end

    % 4th order Runge-Kutta solution algorithm
    p1 = -i/2*((conj(Chi(3,1,1,3))*exp(i*(Delta(1,3,3,1)*v(n-1,1) + phi13)) +...
      conj(Chi(3,1,1,4))*exp(i*(Delta(1,4,3,1)*v(n-1,1) + phi14)))*v(n-1,4) +...
               (conj(Chi(4,1,1,3))*exp(i*(Delta(1,3,4,1)*v(n-1,1) + phi13)) +...
      conj(Chi(4,1,1,4))*exp(i*(Delta(1,4,4,1)*v(n-1,1) + phi14)))*v(n-1,5));

    q1 = -i/2*((conj(Chi(3,2,2,3))*exp(i*(Delta(2,3,3,2)*v(n-1,1) + phi23)) +...
      conj(Chi(3,2,2,4))*exp(i*(Delta(2,4,3,2)*v(n-1,1) + phi24)))*v(n-1,4) +...
               (conj(Chi(4,2,2,3))*exp(i*(Delta(2,3,4,2)*v(n-1,1) + phi23)) +...
      conj(Chi(4,2,2,4))*exp(i*(Delta(2,4,4,2)*v(n-1,1) + phi24)))*v(n-1,5));

    r1 = -i/2*((Chi(3,1,1,3)*exp(-i*(Delta(1,3,3,1)*v(n-1,1) + phi13)) +...
      Chi(3,1,1,4)*exp(-i*(Delta(1,4,3,1)*v(n-1,1) + phi14)))*v(n-1,2) +...
               (Chi(3,2,2,3)*exp(-i*(Delta(2,3,3,2)*v(n-1,1) + phi23)) +...
Chi(3,2,2,4)*exp(-i*(Delta(2,4,3,2)*v(n-1,1) + phi24)))*v(n-1,3)) - Gamma3/2*v(n-1,4);

    s1 = -i/2*((Chi(4,1,1,3)*exp(-i*(Delta(1,3,4,1)*v(n-1,1) + phi13)) +...
      Chi(4,1,1,4)*exp(-i*(Delta(1,4,4,1)*v(n-1,1) + phi14)))*v(n-1,2) +...
               (Chi(4,2,2,3)*exp(-i*(Delta(2,3,4,2)*v(n-1,1) + phi23)) +...
Chi(4,2,2,4)*exp(-i*(Delta(2,4,4,2)*v(n-1,1) + phi24)))*v(n-1,3)) - Gamma4/2*v(n-1,5);

    p2 = -i/2*((conj(Chi(3,1,1,3))*exp(i*(Delta(1,3,3,1)*(v(n-1,1) + h0/2) + phi13)) +...
conj(Chi(3,1,1,4))*exp(i*(Delta(1,4,3,1)*(v(n-1,1) + h0/2) + phi14)))*(v(n-1,4) + h0/2*r1) +...
                     (conj(Chi(4,1,1,3))*exp(i*(Delta(1,3,4,1)*(v(n-1,1) + h0/2) + phi13)) +...
conj(Chi(4,1,1,4))*exp(i*(Delta(1,4,4,1)*(v(n-1,1) + h0/2) + phi14)))*(v(n-1,5) + h0/2*s1));

    q2 = -i/2*((conj(Chi(3,2,2,3))*exp(i*(Delta(2,3,3,2)*(v(n-1,1) + h0/2) + phi23)) +...
```

```
conj(Chi(3,2,2,4))*exp(i*(Delta(2,4,3,2)*(v(n-1,1) + h0/2) + phi24)))*(v(n-1,4) + h0/2*r1) +...
                     (conj(Chi(4,2,2,3))*exp(i*(Delta(2,3,4,2)*(v(n-1,1) + h0/2) + phi23)) +...
conj(Chi(4,2,2,4))*exp(i*(Delta(2,4,4,2)*(v(n-1,1) + h0/2) + phi24)))*(v(n-1,5) + h0/2*s1));

    r2 = -i/2*((Chi(3,1,1,3)*exp(-i*(Delta(1,3,3,1)*(v(n-1,1) + h0/2) + phi13)) +...
     Chi(3,1,1,4)*exp(-i*(Delta(1,4,3,1)*(v(n-1,1) + h0/2) + phi14)))*(v(n-1,2) + h0/2*p1) +...
                          (Chi(3,2,2,3)*exp(-i*(Delta(2,3,3,2)*(v(n-1,1) + h0/2) + phi23)) +...
    Chi(3,2,2,4)*exp(-i*(Delta(2,4,3,2)*(v(n-1,1) + h0/2) + phi24)))*(v(n-1,3) + h0/2*q1)) -...
                                                          Gamma3/2*(v(n-1,4) + h0/2*r1);

    s2 = -i/2*((Chi(4,1,1,3)*exp(-i*(Delta(1,3,4,1)*(v(n-1,1) + h0/2) + phi13)) +...
     Chi(4,1,1,4)*exp(-i*(Delta(1,4,4,1)*(v(n-1,1) + h0/2) + phi14)))*(v(n-1,2) + h0/2*p1) +...
                          (Chi(4,2,2,3)*exp(-i*(Delta(2,3,4,2)*(v(n-1,1) + h0/2) + phi23)) +...
    Chi(4,2,2,4)*exp(-i*(Delta(2,4,4,2)*(v(n-1,1) + h0/2) + phi24)))*(v(n-1,3) + h0/2*q1)) -...
                                                          Gamma4/2*(v(n-1,5) + h0/2*s1);

    p3 = -i/2*((conj(Chi(3,1,1,3))*exp(i*(Delta(1,3,3,1)*(v(n-1,1) + h0/2) + phi13)) +...
conj(Chi(3,1,1,4))*exp(i*(Delta(1,4,3,1)*(v(n-1,1) + h0/2) + phi14)))*(v(n-1,4) + h0/2*r2) +...
                     (conj(Chi(4,1,1,3))*exp(i*(Delta(1,3,4,1)*(v(n-1,1) + h0/2) + phi13)) +...
conj(Chi(4,1,1,4))*exp(i*(Delta(1,4,4,1)*(v(n-1,1) + h0/2) + phi14)))*(v(n-1,5) + h0/2*s2));

    q3 = -i/2*((conj(Chi(3,2,2,3))*exp(i*(Delta(2,3,3,2)*(v(n-1,1) + h0/2) + phi23)) +...
conj(Chi(3,2,2,4))*exp(i*(Delta(2,4,3,2)*(v(n-1,1) + h0/2) + phi24)))*(v(n-1,4) + h0/2*r2) +...
                     (conj(Chi(4,2,2,3))*exp(i*(Delta(2,3,4,2)*(v(n-1,1) + h0/2) + phi23)) +...
conj(Chi(4,2,2,4))*exp(i*(Delta(2,4,4,2)*(v(n-1,1) + h0/2) + phi24)))*(v(n-1,5) + h0/2*s2));

    r3 = -i/2*((Chi(3,1,1,3)*exp(-i*(Delta(1,3,3,1)*(v(n-1,1) + h0/2) + phi13)) +...
     Chi(3,1,1,4)*exp(-i*(Delta(1,4,3,1)*(v(n-1,1) + h0/2) + phi14)))*(v(n-1,2) + h0/2*p2) +...
                          (Chi(3,2,2,3)*exp(-i*(Delta(2,3,3,2)*(v(n-1,1) + h0/2) + phi23)) +...
    Chi(3,2,2,4)*exp(-i*(Delta(2,4,3,2)*(v(n-1,1) + h0/2) + phi24)))*(v(n-1,3) + h0/2*q2)) -...
                                                          Gamma3/2*(v(n-1,4) + h0/2*r2);

    s3 = -i/2*((Chi(4,1,1,3)*exp(-i*(Delta(1,3,4,1)*(v(n-1,1) + h0/2) + phi13)) +...
     Chi(4,1,1,4)*exp(-i*(Delta(1,4,4,1)*(v(n-1,1) + h0/2) + phi14)))*(v(n-1,2) + h0/2*p2) +...
                          (Chi(4,2,2,3)*exp(-i*(Delta(2,3,4,2)*(v(n-1,1) + h0/2) + phi23)) +...
    Chi(4,2,2,4)*exp(-i*(Delta(2,4,4,2)*(v(n-1,1) + h0/2) + phi24)))*(v(n-1,3) + h0/2*q2)) -...
                                                          Gamma4/2*(v(n-1,5) + h0/2*s2);

    p4 = -i/2*((conj(Chi(3,1,1,3))*exp(i*(Delta(1,3,3,1)*(v(n-1,1) + h0) + phi13)) +...
    conj(Chi(3,1,1,4))*exp(i*(Delta(1,4,3,1)*(v(n-1,1) + h0) + phi14)))*(v(n-1,4) + h0*r3) +...
                       (conj(Chi(4,1,1,3))*exp(i*(Delta(1,3,4,1)*(v(n-1,1) + h0) + phi13)) +...
    conj(Chi(4,1,1,4))*exp(i*(Delta(1,4,4,1)*(v(n-1,1) + h0) + phi14)))*(v(n-1,5) + h0*s3));

    q4 = -i/2*((conj(Chi(3,2,2,3))*exp(i*(Delta(2,3,3,2)*(v(n-1,1) + h0) + phi23)) +...
    conj(Chi(3,2,2,4))*exp(i*(Delta(2,4,3,2)*(v(n-1,1) + h0) + phi24)))*(v(n-1,4) + h0*r3) +...
                       (conj(Chi(4,2,2,3))*exp(i*(Delta(2,3,4,2)*(v(n-1,1) + h0) + phi23)) +...
    conj(Chi(4,2,2,4))*exp(i*(Delta(2,4,4,2)*(v(n-1,1) + h0) + phi24)))*(v(n-1,5) + h0*s3));

    r4 = -i/2*((Chi(3,1,1,3)*exp(-i*(Delta(1,3,3,1)*(v(n-1,1) + h0) + phi13)) +...
         Chi(3,1,1,4)*exp(-i*(Delta(1,4,3,1)*(v(n-1,1) + h0) + phi14)))*(v(n-1,2) + h0*p3) +...
                            (Chi(3,2,2,3)*exp(-i*(Delta(2,3,3,2)*(v(n-1,1) + h0) + phi23)) +...
        Chi(3,2,2,4)*exp(-i*(Delta(2,4,3,2)*(v(n-1,1) + h0) + phi24)))*(v(n-1,3) + h0*q3)) -...
                                                            Gamma3/2*(v(n-1,4) + h0*r3);

    s4 = -i/2*((Chi(4,1,1,3)*exp(-i*(Delta(1,3,4,1)*(v(n-1,1) + h0) + phi13)) +...
         Chi(4,1,1,4)*exp(-i*(Delta(1,4,4,1)*(v(n-1,1) + h0) + phi14)))*(v(n-1,2) + h0*p3) +...
                            (Chi(4,2,2,3)*exp(-i*(Delta(2,3,4,2)*(v(n-1,1) + h0) + phi23)) +...
        Chi(4,2,2,4)*exp(-i*(Delta(2,4,4,2)*(v(n-1,1) + h0) + phi24)))*(v(n-1,3) + h0*q3)) -...
                                                            Gamma4/2*(v(n-1,5) + h0*s3);

    %%%   |psi> = c1|1> + c2|2> + c3|3> + c4|4>   %%%
    % c1
    v(n,2) = v(n-1,2) + h0/6*(p1 + 2*p2 + 2*p3 + p4);
    % c2
    v(n,3) = v(n-1,3) + h0/6*(q1 + 2*q2 + 2*q3 + q4);
    % c3
    v(n,4) = v(n-1,4) + h0/6*(r1 + 2*r2 + 2*r3 + r4);
    % c4
```

```
    v(n,5) = v(n-1,5) + h0/6*(s1 + 2*s2 + 2*s3 + s4);

    % Total system population
    v(n,6) = abs(v(n,2))^2 + abs(v(n,3))^2 + abs(v(n,4))^2 + abs(v(n,5))^2;

    % Absorption coefficient
    Kappa(n) = (wL(1,3)/c)*2*numden/(ep0*E(1,3))*imag(conj(v(n,2))*v(n,4)*d(3,1));

end
% Define output variables from solution matrix
t = v(1:n-1,1);
c1 = v(1:n-1,2);
c2 = v(1:n-1,3);
c3 = v(1:n-1,4);
c4 = v(1:n-1,5);
c1234 = v(1:n-1,6);

% Plot level populations
figure(1)
axes('fontsize',30)
plot(t*1e6,abs(c1).^2,'k-',t*1e6,abs(c2).^2,'r-',t*1e6,abs(c3).^2,'b-',t*1e6,abs(c4).^2,'g-','linewidth',2)
legend('\rho_{11}','\rho_{22}','\rho_{33}','\rho_{44}')
axis([0 tmax*1e6 0 1])
title('4-level system, antisymmetric phase')%,'fontsize',18)
xlabel('Time [\mus]')%,'fontsize',18)

% Plot total system population
figure(2)
axes('fontsize',16)
plot(t*1e6,c1234,'k-');
title('Tr[\rho]');
xlabel('Time [\mus]')

% Plot absorption coefficient
figure(3)
axes('fontsize',16)
plot(t*1e6,Kappa(1:n-1),'k-')
title('Absorption coefficient')
xlabel('Time [\mus]')
ylabel('\kappa [m^{-1}]')
```